



UNIVERSITAT POLITÈCNICA
DE CATALUNYA
BARCELONATECH

Programa de Doctorat en Enginyeria de la Construcció

Seismic design of steel beam-to-column joints with Reduced Beam Section using European hot-rolled profiles

Tesi doctoral realitzada per:

Adrià Jiménez Torres

Dirigida per:

Enrique Mirambell Arrizabalaga

Esther Real Saladrigas

Escola Tècnica Superior d'Enginyers de Camins, Canals i Ports de Barcelona
Departament d'Enginyeria Civil i Ambiental

Barcelona, Juliol 2021

Acknowledgements

I would like to thank my PhD directors Enrique Mirambell and Esther Real, for all the guidance and counselling received during all these years. Thank you to Itsaso Arrayago for her readiness to get involved in my thesis when I needed help. Thank you to all the Equaljoints Plus project partners, especially to Elide Nastri for her willingness to collaborate and share her knowledge with others. Also thank you to my family, Laia and Alex for the support you have given to me, engineering-related or otherwise.

This PhD thesis would not have been possible out of the framework of the Industrial Doctorate program of the Generalitat de Catalunya, whose collaboration is hereby acknowledged.

Abstract

The design rules on Reduced Beam Sections (RBS) are covered in the Eurocodes in EN1998-3 as a possible solution to improve rotation capacity of beams for the retrofit of existing structures. The design rules are very similar to those in AISC358 provisions, although European cross-sections and steel grades are different. Research pieces on RBS in a European environment are few and do not study this matter with an extensive parametric study to assess their behaviour. Moreover, the design rules in EN1998-3 only show how to design the weakened section of the beam, but they do not provide any additional information on whether further action is needed on the structure for the design of other members such as braces or if special considerations need to be made for connection detailing. The current state of the Eurocodes does not consider the design of a new structure with RBS, while AISC358 provisions do allow for new RBS designs.

The aim of this PhD thesis is to study the behaviour of the RBS and find the most relevant design parameters affecting its response in a beam-to-column assembly level and to study the benefits of incorporating RBS as a solution for the design of new structures in seismic areas. In order to fulfill the first goal, a numerical model has been developed in Abaqus in order to assess the behaviour of RBS and to discuss the results obtained from them. Hot-rolled European sections have been studied from the HEA and IPE cross-section families, as well as a built-up slender girder and an American Jumbo section. Several different cutouts (or trimmed flange widths) are investigated, as well as S235 and S355 steel grades with their cyclic hardening properties. The influence on the column web panel strength is also considered in the parametric study. The results obtained are then examined to compare degradation ratios, overstrength ratios, lateral-torsional buckling development, dissipated plastic work and plastic damage by means of equivalent plastic strains (PEEQ). In order to fulfill the second goal, two different studies have been performed to assess the influence of the RBS in a structure subjected to seismic load. The behaviour of a structure provided with RBS is compared to that of a control structure without RBS. The results have been obtained and the differences found have been quantified in order to objectively report the benefits found when adopting RBS.

After having studied the behaviour of the RBS both locally (at a beam-to-column level) and globally, the main conclusions have been derived. Also, design recommendations to take into consideration for the design of new RBS are provided in order to ensure a proper behaviour of the RBS when subjected to seismic loads and to guarantee overall good structural behaviour.

Contents

Acknowledgements	2
Abstract	3
1 Introduction	6
2 State of the art	9
2.1 Philosophy of seismic design	9
2.1.1 Connections for seismic applications	14
2.2 Reduced Beam Sections in Standards	24
2.2.1 RBS in Eurocodes	24
2.2.2 RBS in AISC	27
3 Study on the local behaviour of the RBS	31
3.1 General	31
3.2 Definition of the numerical model	32
3.2.1 Geometries	32
3.2.2 Loading of the specimens	34
3.2.3 Mesh and boundary conditions	35
3.2.4 Constitutive law of the material	37
3.2.5 Validation of the numerical model	38
3.3 Parametric study	46
3.3.1 Studied cross-sections	46
3.3.2 Steel grades	49
3.3.3 Radius cut geometry	50
3.3.4 Column web panel strength	51
3.4 Results	54
3.4.1 Detailed results for HEA600 beam, $r = 0.833$, $g = 0.2b_f$, S355	54
3.4.2 Detailed results for IPE750 beam, $r = 1.6$, $g = 0.3b_f$, S235	58
3.4.3 Detailed results for built-up girder, $r = 1.312$, $g = 0.25b_f$, S355	61
3.4.4 Detailed results for Jumbo section, $r = 1.6$, $g = 0.25b_f$, S355	65
3.4.5 Summary of the results for all the assemblies	68
3.5 Analysis of the results	88
3.5.1 Influence of the yield stress f_y	88
3.5.2 Influence of the trimmed flange width g	92
3.5.3 Influence of the web panel strength ratio r	100
3.5.4 Influence of the slenderness of the member plates	104
3.6 Statistical analysis of the results obtained for γ_{sh}	108

3.6.1	γ_{sh} values using prEN1998-1-2:2020 values for γ_{ov}	109
3.6.2	Summary of the values obtained for the γ_{sh} distributions . .	110
4	Structural behaviour under seismic actions. Benefits of the dog-bone	112
4.1	General	112
4.2	First study, pushover analysis	113
4.2.1	Moment-rotation curves and numerical modelling	113
4.2.2	Moment Resisting Frames	118
4.2.3	Dual Eccentrically-braced Frames	121
4.2.4	Analysis of the results	124
4.3	Second study, nonlinear time-history analysis	126
4.3.1	Definition of the seismic action	126
4.3.2	Numerical model	128
4.3.3	Results	131
5	Summary, conclusions and design recommendations	137
5.1	Summary	137
5.2	Conclusions	138
5.3	Design recommendations	140
6	Future research	142
	References	143

1 Introduction

Findings after the earthquakes of Northridge and Kobe (in 1994 and 1995, respectively) have come to show that steel structures are very much sensitive to cyclic actions. A large amount of detailings of steel joints have been found to develop cracks, which leads to a brittle failure of the joint. A lot of research has been undertaken since in order to find better solutions for these connections. One of the main research projects was the SAC project in 1994 with the objective of investigating the damage to welded MRFs during the Northridge earthquake and developing repair techniques and new design approaches to minimise damage to steel MRF in future seismic events. The project was funded by the Federal Emergency Management Agency (FEMA).

Since then, many different solutions have been developed to prevent such failures, which generally entail reinforcing the connection and limiting its plastic demand or weakening the beam member of the connection to concentrate plastic strains away from the connection and into the beam.

The Reduced Beam Section (RBS, also called dog-bone) is a good alternative to the reinforcement of the connection due to its ease of execution and its reduced cost (reinforcements usually entail large welds and more manpower). Owing to their convenience, RBS connections are becoming increasingly popular in seismic areas since they were first proposed by Plumier [47] in 1990. Indeed, the RBS are being object of study by many researchers like Montuori [41], [40] in Italy; Pachoumis [45], [46], Sophianopoulos [55], Sofias [54] and Deri [14] in Greece; Engelhardt [20] in the USA; Deylami [15], Morshedi [42], Tahamouli [52] and Saleh [53] in Iran; Han [27], [26] in Korea, and many others around the world [9], [34], [59], [25], [44], [51].

The RBS entails performing a circular cut on the beam flanges at a certain distance of the beam-to-column connection. This radius cut weakens the beam at that section so that failure is localised in that specific location, sparing the connection from any plastic engagement and completely avoiding the possibility of brittle fracture of the welds. Figure 1 shows a schematic of a beam-to-column connection provided with RBS.

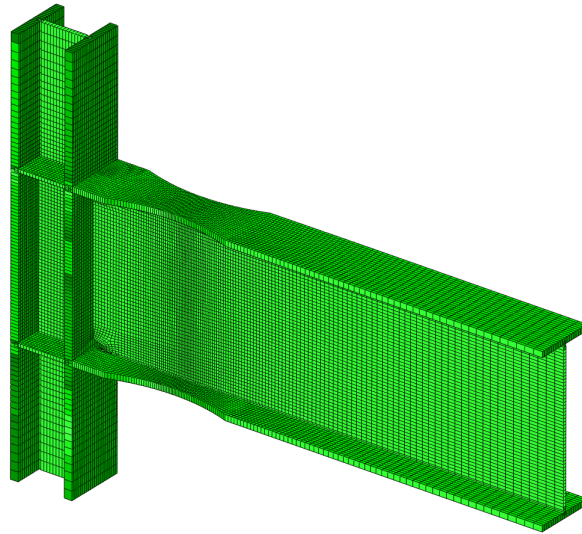


Figure 1: Schematic of a beam-to-column connection provided with RBS

The methodology used in the research presented in this PhD thesis is widely used by many researchers. The usual procedure is to gather data by means of experimental results and/or numerical simulations. The experimental results are used to validate the finite element model. Once the model is validated it can be used to obtain a larger amount of data by means of parametric studies where the influence of the most relevant parameters can be observed and more general conclusions can be drawn. In this investigation, a study on the behaviour of Reduced Beam Sections is undertaken by using numerical simulations. The aims of this research are:

- To provide an overview on the general principles of structural seismic design and specifically on seismic connection design for steel structures.
- To gather information on the behaviour of Reduced Beam Sections and its state of the art (articles, reports, design manuals, standards, etc.)
- To evaluate the structural behaviour of planar Moment-resisting frames (MRFs) when adopting Reduced Beam Sections to improve their response when subjected to severe seismic actions and show the benefits of using dog-bones.
- To research in current norms and codes to evaluate and compare the existing rules to be considered for the design of a Reduced Beam Section.
- To develop a numerical model to reproduce experimental tests of beam-to-column assemblies subjected to a cyclic loading protocol in order to validate the numerical model with experimental results.

- To undertake a parametric study to determine which parameters are the most impactful in the behaviour of a Reduced Beam Section when subjected to cyclic actions and to quantify such impact.
- To analyse the obtained results in the numerical simulations and obtain the ultimate loads in every studied case in accordance with a set of established criteria.
- To provide a proposal of design recommendations and draw conclusions with the information obtained from the simulations and the analysis of their results.

In order to fulfil these goals, this document is divided in the following sections:

- State of the art: seismic design philosophy and different possible approaches. Steel connections for seismic applications. Discussion on different types of connections according to their strength related to the beam. Reduced Beam Sections. Overview of the experimental and numerical studies undertaken on dog-bone joints. Discussion on the current norms AISC 358 [2] and EN 1998-3 [19].
- Numerical model: detailed description of the developed model. Description and justification of the geometries considered, boundary conditions applied and meshing. Constitutive law of the material used. Failure criteria. Validation of the numerical model with experimental results found in the literature.
- Parametric study: determination of the impact of each of the parameters involved in the problem. Cross-section families, steel grades, geometry of the cut for the reduced section. Slenderness of the members plates.
- Results: display of all the results obtained.
- Analysis of the results: interpretation and discussion on the results obtained in the simulations.
- Structural behaviour under the effects of a seismic action. Benefits of the dog-bone: examples of planar frames subjected to seismic loads, with special attention to the influence of the dog-bone to the global structural behaviour. Studies on the improved behaviour of structures subjected to severe seismic loads when adopting Reduced Beam Sections.
- Summary, conclusions and design recommendations.
- References.

2 State of the art

2.1 Philosophy of seismic design

Experience shows that steel structures have a good behaviour under seismic action. There are two different possible approaches for the design of a steel structure in a seismic area. The structure can be designed with members and cross-sections large enough to be able to resist the seismic forces in their elastic range (low-dissipative behaviour), or the structure can be designed with slightly smaller members allowing for yielding to occur in certain areas of the structure to form plastic dissipative zones (dissipative behaviour).

The difference between dissipative and low-dissipative behaviours is dictated by both the ductility and energy dissipation capacity of the structure. The ductility of a structure represents the capacity of a structure to deform in the plastic domain without substantially reducing its bearing capacity (Landolfo et al. [35]). In figure 2.2, two load-displacement curves are plotted for two different structures subjected to increasing lateral loads. As it can be observed, both structures have the same lateral strength F_y . The displacement δ_u corresponds to the displacement capacity of the structure, achieved when the structure undergoes a sudden loss of lateral strength (failure).

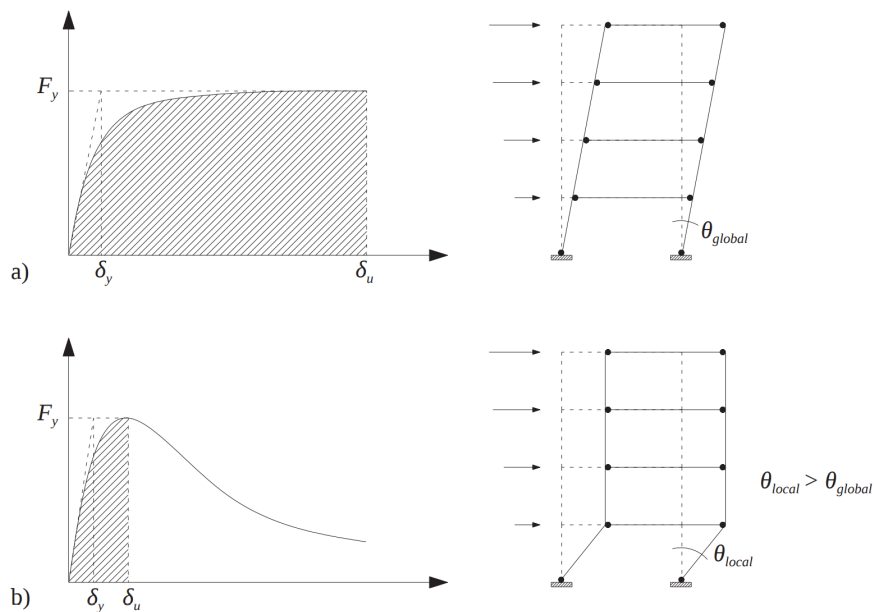


Figure 2.2: Ductility of frames: a) high and b) poor displacement capacity. Source: Landolfo et al. [35]

Despite both structures having the same lateral strength, structure a) exhibits much more ductile behaviour, very different from structure b). The displacement capacity δ_u is much larger than that of structure b), the ductility exhibited $\mu = \delta_u/\delta_y$ is also much larger, and structure a) also absorbed a much larger amount of energy, represented as the shaded area under the curve.

However, a good seismic structural behaviour also depends on the shape of the cyclic response of the dissipative zones. Concerning this idea, figure 2.3 shows two different hysteresis loops of frames under cyclic loading having the same monotonic response and displacement capacity δ_u . In this case, the shape of the hysteresis loops depends on the number of loading cycles, since fatigue phenomena can develop and have an influence on the response. The frame in figure 2.3 a) dissipates a greater amount of energy before failure than b), providing a better seismic performance. The energy dissipated is represented as the area under the hysteresis loops.

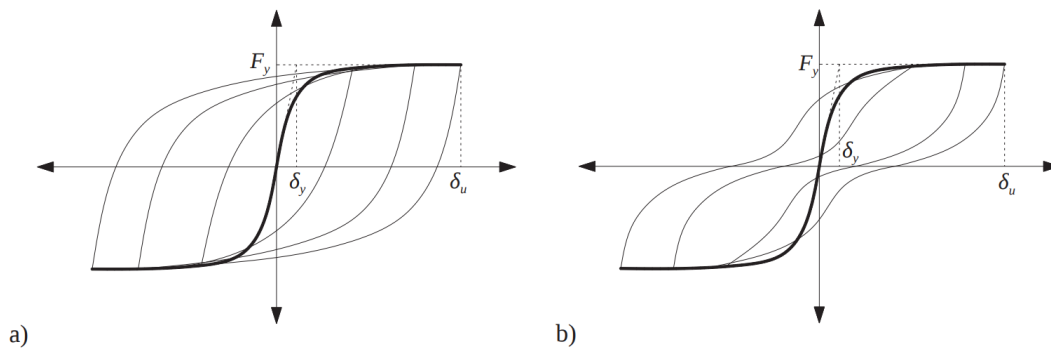


Figure 2.3: Dissipative capacity of frames: a) high and b) poor energy dissipation. Source: Landolfo et al. [35]

The elastic design of structures in seismic areas generally leads to uneconomical and potentially unsafe solutions. Elastic design of each of the components of the structure according to the external forces does not ensure a good global behaviour. Also, larger accelerations than those expected in the design phase may occur due to the randomness of the seismic action. On the other hand, ductile and dissipative structures are convenient because they can avoid brittle phenomena and lead to less expensive constructions. In order to exploit the ductility, ductile structures are usually designed to resist forces smaller than those needed to obtain an elastic response under seismic action corresponding to the Ultimate Limit State (ULS). However, plastic deformation imposed by the seismic action must not exceed the deformation capacity of the structure in the plastic domain to prevent excessive

damage that may compromise the stability of the structure. Therefore, the minimum strength of the structure F_y against lateral forces is directly related to the plastic deformation capacity.

Figure 2.4 shows the relationship between the lateral strength of the structure F_y and the displacement demand δ_{Ed} for a given seismic action.

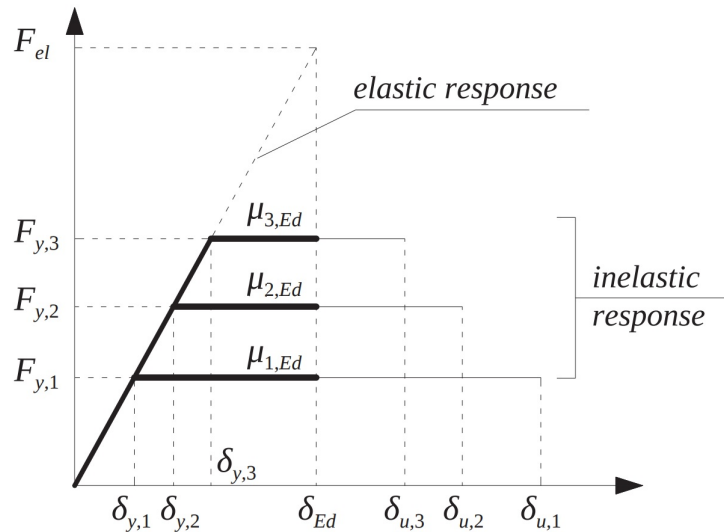


Figure 2.4: Strength vs displacement demand relationship. Source: Landolfo et al. [35]

When keeping the displacement demand δ_{Ed} constant (as indicated with thick black lines in figure 2.4), the lower the lateral strength of the structure, the higher the ductility demand ($\mu_{Ed} = \delta_{Ed}/\delta_y$) on the structure is. Therefore, very ductile structures can be designed to resist smaller seismic forces, which can be determined by scaling the elastic forces by the so-called behaviour factor q , which depends on the structural typology. By adopting a behaviour factor q the design spectrum is reduced, and the accelerations and forces introduced in the structure will be lower. The difference can be observed in figure 2.5.

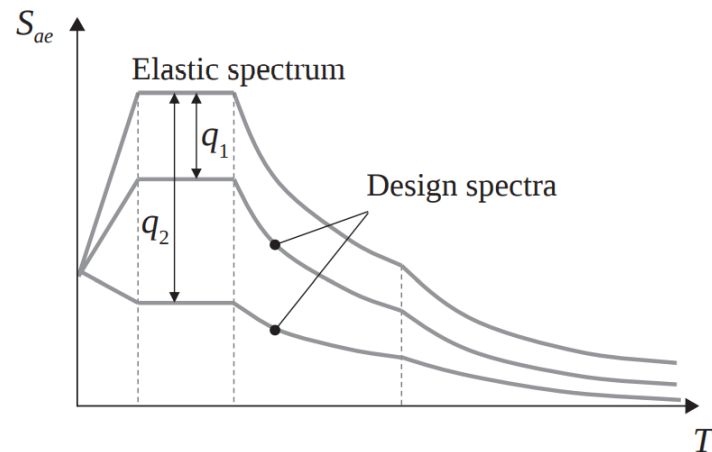


Figure 2.5: Elastic vs design spectra according to EC8. Source: Landolfo et al. [35]

EN1998-1 [18] defines three ductility classes (Ductility Class Low, Medium and High - DCL, DCM and DCH) for structures in seismic areas. The highest ductility classes (DCH and DCM) have the benefit of a large q factor, with a very reduced design seismic spectrum. However, it is vital to provide the necessary ductility to the structure. The current state of EN1998-1 [18] allows for two different design approaches for the design of a new structure:

- Low-dissipative behaviour: the design is done according to an elastic analysis providing enough strength to the members and all components of the structure to remain in their elastic domain. This type of behaviour can only be used for structures with Ductility Class Low (DCL). It is recommended to use a behaviour factor q of up to 1.5, which allows for very limited plastic engagement of the structural members.
- Dissipative behaviour: the design allows for the formation of dissipative zones in the structure, carefully designed to that effect. Ductility Class High (DCH) and Ductility Class Medium (DCM) are found in this approach. DCM structures behaviour factor q varies according to the structural type, being smaller than or equal to 4. DCH structures are the most dissipative, and their behaviour factor q can be as high as 6.5, provided they are moment resisting frames (with or without buckling-restrained braces) constituted by class 1 cross-sections.

When designing a structure in a low seismicity area where the Peak Ground Acceleration (PGA) is smaller than 0.1g, it is possible to ignore all the rules given

in EN1998-1 - section 6 (specific rules for steel buildings), but the rules given in sections 2 through 4 still apply, which are material-independent seismic rules (in particular, sections 4.4.2 and 4.4.3). These rules establish that structures in seismic areas must have regularity in plan and elevation in order to exhibit good seismic behaviour, and also provide the safety requirements for Ultimate Limit State (ULS) and Damage Limitation State (DLS). These safety requirements are several:

- Resistance checks against seismic action: The members need to be designed in order to resist a certain design seismic load (clause 4.4.2.2).
- $P - \Delta$ effects: Second-order effects need to be accounted for in the design unless it is proven that the structure is not sensitive to second-order effects (clause 4.4.2.2).
- $\sum M_{Rc} \geq 1.3 \sum M_{Rb}$ for MRFs: Moment-Resisting Frames need to be designed with the strong column-weak beam principle. It is required to provide at least a flexural overstrength of 30% to the columns of the lateral-resistant system to ensure that the members undergoing plastic engagement are beams and not columns (clause 4.4.2.3).
- Diaphragms overstrength: the diaphragms need to be able to transmit the loads to the lateral-resisting system with sufficient overstrength (clause 4.4.2.5).
- Seismic joints conditions for buildings: Buildings need to be protected from earthquake-induced pounding from adjacent structures or between structurally independent units of the same building. Sufficient room needs to be provided so that the structural displacements do not cause impacts (clause 4.4.2.7).
- Interstorey drift limitations: The Damage Limitation requirement is considered to be fulfilled if the interstorey drifts are limited under certain prescribed values for a seismic action having larger probability of occurrence than the design seismic action corresponding to the "no-collapse requirement" (clause 4.4.3.2).

For cases of very low seismicity where the Peak Ground Acceleration is smaller than 0.04g, no seismic design is required and the seismic action can be ignored. Due to the reasons mentioned above regarding the uncertainty of the severity of the seismic action as well as the global behaviour of the structure, Eurocode 8 recommends using the DCL concept with caution and only for low seismicity cases. However, for all the other cases where the seismic action plays a substantial role in the design, a dissipative design approach is advised.

The design criteria for DCM and DCH structures are:

- Structures with dissipative zones shall be designed so that yielding or local buckling or other phenomena due to hysteretic behaviour do not affect the overall stability of the structure.
- Dissipative zones shall have adequate ductility and resistance. The resistance must be verified according to EN1993.
- Dissipative zones may be located in the structural members or the connections.
- If dissipative zones are located in the structural members, the non-dissipative parts and the connections of the dissipative parts to the rest of the structure must have sufficient overstrength to allow for the development of cyclic yielding in the dissipative parts.
- When dissipative zones are located in the connections, the connected members must have sufficient overstrength to allow for the development of cyclic yielding in the connections.

The abovementioned design criteria are the criteria included in the current version of EN1998-1 [18] and are soon to be changed by those in the forthcoming revision of the Eurocodes. prEN1998-1-2:2020 provides a slightly different definition of the ductility classes (DC1, DC2 and DC3) with slightly different design rules with minor changes to the q values for each ductility class depending on the cross-section class and structural type. However, the underlying concepts for the design remain the same and will be based on the same seismic design philosophy.

2.1.1 Connections for seismic applications

Connections play a crucial role in the behaviour of a steel structure. The design of the connections is of vital importance for an adequate structural behaviour under seismic action. According to Eurocode 8 - part 1 [18] the seismic design of steel structures should be done based on the concept of dissipative structures, in which certain parts of the structure need to be capable of developing plastic strains to dissipate energy due to the earthquake. On the other hand, non-dissipative components should remain in their elastic domain in order to avoid any damage. Thus, it is important to establish a hierarchy of resistances for the structural elements, which is the fundamental principle that allows for this behaviour. Therefore it is necessary to design the elastic components in such a way that they can withstand the plastic resistance of the dissipative components.

According to the design approach developed in the Equaljoints project [48], the connection is composed by three macrocomponents (namely the column web panel, the connection and the beam - see figure 2.6).

Three different strength-based criteria can be adopted for the connection design:

- Full strength connection: the connection is designed to be stronger than the other macrocomponents so that yielding occurs in the column web panel and beam.
- Equal strength connection: the connection is designed to have a strength similar to that of the other macrocomponents. Theoretically yielding should be simultaneous in all three macrocomponents.
- Partial strength connection: the connection is designed to be weaker than the other macrocomponents, so the connection components are designed to develop plastic strains.

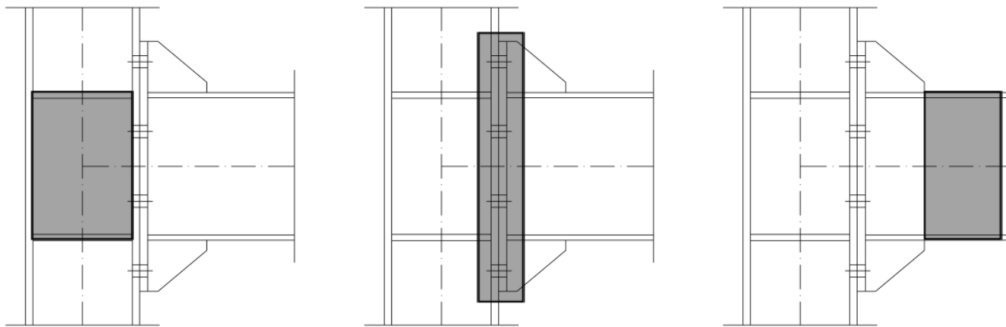


Figure 2.6: Macrocomponents of the connection. Left to right: web panel, connection and beam. Source: Equaljoints Plus [48]

And according to the design objectives of the connection, the following inequality needs to be fulfilled.

$$M_{con,Rd} \geq M_{con,Ed} \quad (2.1)$$

In the current state of both Eurocode 3 - part 1-8 [17] and Eurocode 8 - part 1 [18], the case of equal strength connections proposed in the Equaljoints project [48] as the intermediate performance level is not considered. According to the current classification in the Eurocodes, equal strength performance should be treated as partial strength.

The main source of plastic strains in a seismic event is the beam end. Depending on the plastic hinge location, amount of strain hardening and expected yield strength at the plastic hinge, the design moment at the column face may be obtained according to equation 2.2:

$$M_{con,Ed} = \alpha(M_{b,Rd} + V_{b,Ed} \cdot s) \quad (2.2)$$

where $M_{con,Ed}$ is the design bending moment at the connection with the column face. In the case of a simple MRF, $M_{b,Rd}$ is just the plastic flexural resistance of the beam M_{pl} .

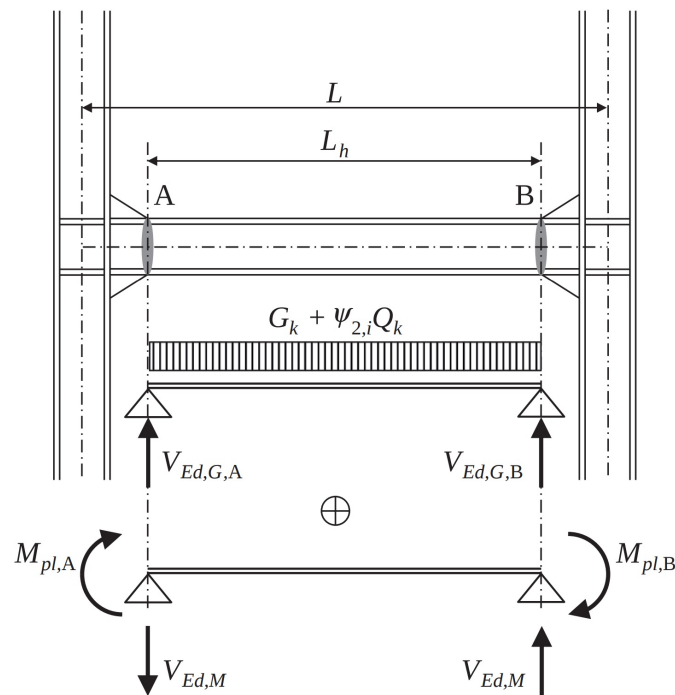


Figure 2.7: Position of the plastic hinges in a MRF span. Source: Landolfo et al. [35]

α depends on the design performance level. It is equal to $\gamma_{sh} \cdot \gamma_{ov}$ for full strength joints (being γ_{sh} the strain hardening factor and γ_{ov} the overstrength factor due to material randomness), equal to 1 for equal strength joints and lower than 1 for partial strength connections. In order to avoid excessive damage in the connections, in the Equaljoints project the recommended value of α for partial strength joints is 0.6 or 0.8. $M_{b,Rd}$ is the plastic bending resistance of the connected beam, s is the distance between the column face and the plastic hinge location in the

beam and $V_{b,Ed}$ is the shear force acting in the beam, given by equation 2.3:

$$V_{b,Ed} = V_{b,Ed,M} + V_{b,Ed,G} \quad (2.3)$$

where $V_{b,Ed,M}$ is the shear force associated to the formation of plastic hinges at both ends of the beam, spaced by the length L_h , and calculated as:

$$V_{b,Ed,M} = \frac{2 \cdot M_{b,Rd}}{L_h} \quad (2.4)$$

and $V_{b,Ed,G}$ is the shear force due to gravity loads.

Concerning both γ factors, further considerations are necessary: γ_{ov} is assumed equal to 1.25, as recommended by EN1998-1 [17]. The strain hardening factor γ_{sh} is assumed differently by EN1993-1-8 [17] and EN1998-1 [18]. In particular, EN1993-1-8 recommends to consider a γ_{sh} ratio equal to 1.2 for full strength joints, while EN1998-1 on the contrary assumes a value equal to 1.1. Several empirical equations are available in literature to estimate the flexural strain hardening γ_{sh} developed by steel beams. Based on the main findings obtained by Mazzolani and Piluso [39], D'Aniello et al [12], Güneyisi et al [23],[24] it can be argued that γ_{sh} factor ranges within 1.1-1.2 for European profiles commonly used for beams (e.g. IPE), thus larger than the value recommended by Eurocode 8, but in line with AISC358-10 that assumes the following overstrength factor:

$$\gamma_{sh,AISC} = \frac{f_y + f_u}{2 \cdot f_y} \leq 1.2 \quad (2.5)$$

And it is therefore recommended in the Equaljoints project to adopt the more conservative value $\gamma_{sh} = 1.2$.

Similarly, another design objective can be defined for the column web panel:

- Full strength panel: the column web panel is designed to be stronger than the other macrocomponents so that yielding occurs in the connection and beam.
- Equal strength panel: the column web panel is designed to have a strength similar to that of the other macrocomponents. Theoretically yielding should be simultaneous in all three macrocomponents.
- Partial strength panel: the column web panel is designed to be weaker than the other macrocomponents, so the column web panel is designed to develop plastic strains.

Figure 2.8 shows the forces acting on the column web panel in a simple beam-to-column connection (only one beam connects to the column) when the beam develops a plastic hinge under positive bending:

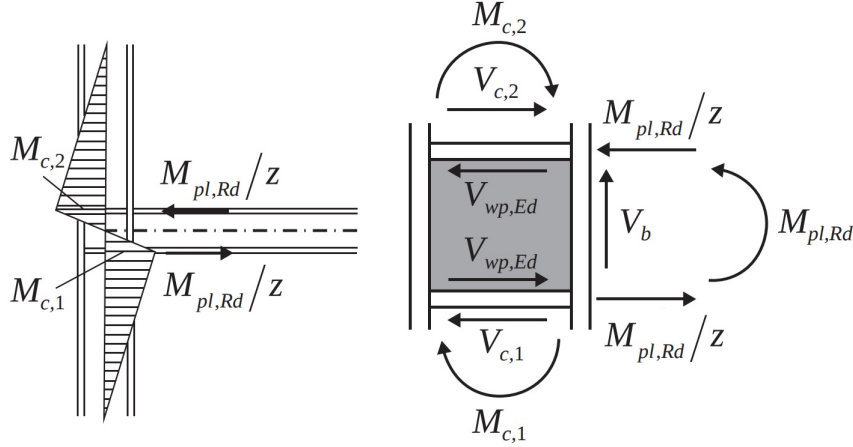


Figure 2.8: Forces acting on the column web panel. Source: Landolfo et al. [35]

For the general case of a double-sided beam-to-column joint with both beams developing plastic hinges under opposite sign bending, the shear force in the column web panel may be determined as:

$$V_{wp,Ed} = \frac{\sum M_{pl,Rd,i}}{z} - \left(\frac{V_{c1,Ed} + V_{c2,Ed}}{2} \right) \quad (2.6)$$

where $V_{wp,Ed}$ is the design shear force in the column web panel, $V_{c1,Ed}$ and $V_{c2,Ed}$ are the shear forces in the column, z is the internal lever arm. In order to account for the design performance level (which may be different from the value adopted for the design of the connection) and for the possibility of shifting the plastic hinge position to a specific area the design shear on the web column is calculated as:

$$V_{wp,Ed} = \alpha \cdot \left(\frac{\sum M_{pl,Rd,i}}{z} + V_b \cdot s \right) - \left(\frac{V_{c1,Ed} + V_{c2,Ed}}{2} \right) \quad (2.7)$$

And according to the design objectives of the connection, the following inequality shall be checked:

$$V_{wp,Rd} \geq V_{wp,Ed} \quad (2.8)$$

where $V_{wp,Rd}$ is the shear resistance of the column web panel.

The joints can also be classified and designed according to a ductility criterion. The joint ductility depends on the type of failure mode and the corresponding plastic deformation capacity of the activated component. The basic joint components can be found in table 2.1.

Table 2.1: Basic joint components. Source: EN1998-3, Table 6.1 [19]

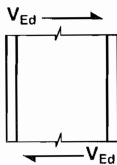
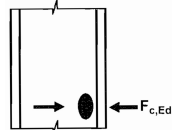
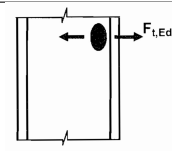
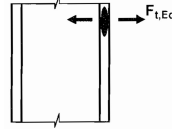
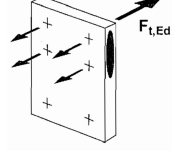
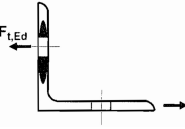
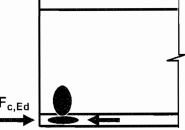
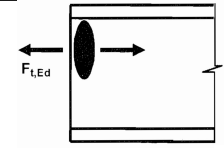
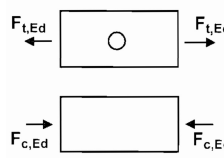
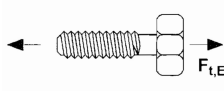
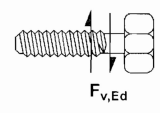
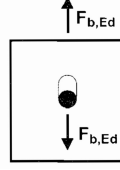
Component	Resisting mechanism
Column web panel in shear	 A rectangular diagram representing a column web panel. Two horizontal arrows labeled V_{Ed} point in opposite directions (one to the right, one to the left) at the top and bottom edges, indicating shear force.
Column web in transverse compression	 A vertical rectangular diagram representing a column web. A horizontal arrow labeled $F_{c,Ed}$ points to the right from the left side, and another horizontal arrow labeled $F_{c,Ed}$ points to the left from the right side, indicating transverse compression.
Column web in transverse tension	 A vertical rectangular diagram representing a column web. A horizontal arrow labeled $F_{t,Ed}$ points to the right from the left side, and another horizontal arrow labeled $F_{t,Ed}$ points to the left from the right side, indicating transverse tension.
Column flange in bending	 A vertical rectangular diagram representing a column flange. A horizontal arrow labeled $F_{t,Ed}$ points to the right from the left side, and another horizontal arrow labeled $F_{t,Ed}$ points to the left from the right side, indicating bending.
Endplate in bending	 A 3D perspective diagram of an endplate. Several arrows labeled $F_{t,Ed}$ point outwards from the top and bottom surfaces, indicating bending.
Flange cleat in bending	 A diagram of an L-shaped flange cleat. A horizontal arrow labeled $F_{t,Ed}$ points to the right from the top flange, and another horizontal arrow labeled $F_{t,Ed}$ points to the left from the bottom flange, indicating bending.
Beam or column flange and web in compression	 A rectangular diagram representing a beam or column flange and web. A horizontal arrow labeled $F_{c,Ed}$ points to the right from the left side, and another horizontal arrow labeled $F_{c,Ed}$ points to the left from the right side, indicating compression.

Table 2.1: Basic joint components. Source: EN1998-3, Table 6.1 [19]. Continued from previous page

Beam web in tension	
Plate in tension or compression	
Bolts in tension	
Bolts in shear	
Bolts in bearing (on beam flange, column flange, endplate or cleat)	

The strength and stiffness of each component can be calculated with the component method, found in EN1993-1-8. For all the components involving failure of plates and member panels, the component method uses a T-stub model to calculate their strength.

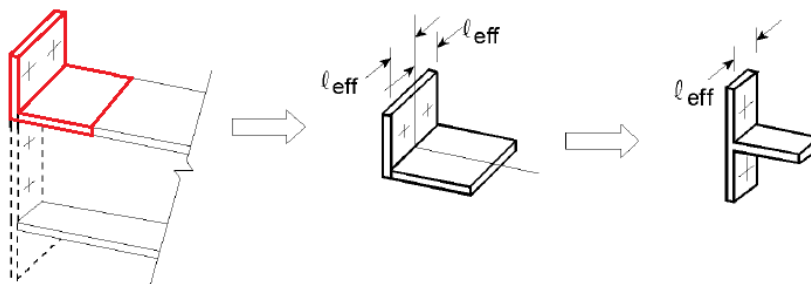


Figure 2.9: Equivalent T-stub model in an endplate for the application of the component method. Source: EN1993-1-8 [17]

As it has been previously stated, the failure mode of each of the components of the

joint determines whether the connection will behave in a ductile or brittle manner when under extreme loads. Figure 2.10 depicts the dependency of failure mode on geometric properties and endplate to bolt strength ratio (Jaspart, 1997 [30]).

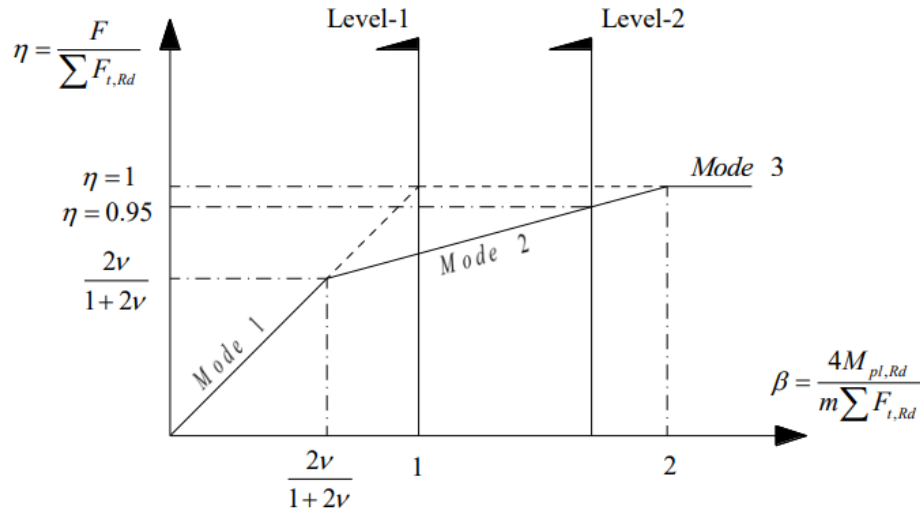


Figure 2.10: Ductility criterion: T-Stub resistance and corresponding failure mechanism. Source: Equaljoints Plus [48]

In abscissa it is reported the ratio β between the flexural strength ($M_{pl,Rd}$) of the plates or column flanges, and the axial strength of the bolts ($F_{t,Rd}$), while the vertical axis reports the ratio η between the T-stub strength (F) over $F_{t,Rd}$. The strength for mode 1 in case of non-circular pattern depends on the ratio $\nu = n/m$, where m is the distance between the bolt axis and the flange-to-web expected location of the plastic hinge, and n is the minimum of the distance between the edge of the flange and the bolts axis or $1.25m$. In line with figure 2.10, two possible ductility criteria can be adopted to avoid mode 3, namely:

- Level 1: $\beta \leq 1$, this condition imposes either a failure mode I or failure mode II (but very close to mode I), which provides very high ductility.
- Level 2: $\beta < 2$ and $\eta \leq 0.95$, this condition imposes a failure mode II with limited ductility, but avoiding brittle failure.

The level of ductility to be guaranteed depends on the design performance objectives. It is crucial to provide larger ductility to equal and partial strength joints where plastic strains will appear. On the contrary, for full strength joints no additional requirements are necessary if sufficient overstrength is provided.

According to the EN1993-1-8 [17], the joint rotation capacity should be checked if $M_{j,Rd}$ is less than $1.2M_{b,pl,Rd}$. This rule establishes that when sufficient overstrength is provided to the connection no special rotation requirements apply, since the main source of plastic dissipation will be a plastic hinge in the beam thus very much limiting plastic engagement of the connection. When the overstrength is not provided the check can be accomplished in two alternative ways: 1) performing experimental tests; 2) controlling the thickness t of either endplate or column flange, provided that the joint design moment resistance is governed by those components (and avoiding any failure mechanism governed by other components), which should satisfy the following inequality:

$$t \leq 0.36d\sqrt{f_{ub}/f_y} \quad (2.9)$$

where d is the nominal bolt diameter, f_y is the yield strength of the relevant basic component and f_{ub} is the bolt ultimate strength. Equation 2.9 would theoretically comply with the ductility Level 1 depicted in figure 2.10, assuming that the resistance of each individual bolt $F_{t,Rd}$ is greater than the resistance $F_{p,Rd}$ of the connected plates (endplate or column flange) associated to a circular pattern failure mechanism. In particular, the design resistance of a bolt in tension $F_{t,Rd}$ is given as follows:

$$F_{t,Rd} = \frac{0.9A_s f_{ub}}{\gamma_{M2}} \quad (2.10)$$

where A_s is the tensile stress area of the bolt and γ_{M2} is the relevant partial safety factor (i.e. Eurocode recommended value is equal to 1.25). In addition, equation 2.9 uses the design resistance $F_{p,Rd}$ corresponding to a circular mechanism, which can be assumed as follows:

$$F_{p,Rd} = \frac{\pi t^2 f_y}{\gamma_{M0}} \quad (2.11)$$

where t is the plate thickness and γ_{M0} is the relevant partial safety factor recommended equal to 1. It should be noted that equations 2.10 and 2.11 assume perfectly plastic behaviour of steel plates. However, in light of the considerations previously discussed, the ductility level 1 for seismic resistant partial strength joints should be expressed accounting for both the random variability of plate material and its relevant strain hardening, so that the following inequality can be used:

$$F_{t,Rd} \geq \alpha \cdot F_{p,Rd} = \gamma_{sh} \cdot \gamma_{ov} \cdot F_{p,Rd} \quad (2.12)$$

The overstrength factor $\alpha = \gamma_{sh} \cdot \gamma_{ov}$ in equation 2.12 can be taken equal to 1.5, since the Eurocode recommended value for γ_{ov} is equal to 1.25, the value for γ_{sh} is equal to 1.2 for European mild carbon steel, and the recommended partial safety factor γ_{M0} is equal to 1.0. Thus, rearranging the inequality 2.12 with expression 2.9, the ductility condition accounting for capacity design criteria can be expressed as follows:

$$t \leq \frac{0.42d}{\sqrt{\gamma_{sh} \cdot \gamma_{ov}}} \cdot \sqrt{\frac{\gamma_{M0} \cdot f_{ub}}{\gamma_{M2} \cdot f_y}} \cong 0.30d \cdot \sqrt{\frac{f_{ub}}{f_y}} \quad (2.13)$$

Regarding full and equal strength joints, even though either no or little ductility should be exploited respectively, a local hierarchy criterion is advisable in order to avoid undesirable failure mode in the brittle components due to material variability. Hence, in line with ductility Level 2, the strength of bolts should satisfy the following inequality:

$$F_{t,Rd} \geq \gamma_{ov} \cdot F_{p,Rd} \quad (2.14)$$

It is important to highlight that all criteria previously described require that failure of welds has to be unquestionably avoided, because of their brittle collapse mechanism.

EN1998-1 [18] establishes in clause 6.6.4 (3) a minimum rotation to be achieved by the connections according to the design objectives:

- Ductility Class High (DCH) structures: the minimum plastic rotation θ_p to be achieved is 35mrad.
- Ductility Class Medium (DCM) structures with $q \geq 2$: the minimum plastic rotation θ_p to be achieved is 25mrad.

In the American standard, the AISC341-16 Seismic Provisions [1] have requirements for connections different from those found in Eurocode 8:

- Special Moment Frames (SMF) structures: the minimum plastic rotation θ_p to be achieved is 40mrad and the flexural resistance must be at least equal to $0.8M_{pl}$ of the connected beam at a rotation of 40mrad.
- Intermediate Moment Frames (IMF) structures: the minimum plastic rotation θ_p to be achieved is 20mrad and the flexural resistance must be at least equal to $0.8M_{pl}$ of the connected beam at a rotation of 20mrad.

2.2 Reduced Beam Sections in Standards

2.2.1 RBS in Eurocodes

The information on RBS in the Eurocodes is quite limited. In fact, the concept of RBS does not appear in EN1993-1 or EN1998-1. Instead, it appears in EN1998-3, clause B.5.3.4 - Weakening of beams in Annex B [19] for steel and composite structures as a possible solution to improve rotational capacity of members for the retrofitting of damaged buildings due to earthquake. In other words, the European standard does not account for the possibility of the design of a new structure provided with dog-bones but only sees the dog-bone as a retrofitting option. The only specific rule that EN1998-3 gives for the dog-bones adequate behaviour is a required total rotation capacity associated to each limit state defined in EN1998-1 [18]:

Table 2.2: Required rotation capacity of RBS, in mrad. Source: EN1998-3, Annex B [19]

Damage Limitation	Significant Damage	Near Collapse
10	25	40

However, the indications in table 2.2 can be assumed to be achieved if the following procedure is adopted for the design:

- Determine the distance from the beginning of the RBS trim to the column flange a and the reduced flange length b as follows:

$$a = 0.6b_f \quad (2.15)$$

$$b = 0.75d_b \quad (2.16)$$

where b_f is the beam flange width and d_b is the beam depth.

- Determine the distance of the theoretical plastic hinge location at the centre of the RBS from the column face, s , as:

$$s = a + b/2 \quad (2.17)$$

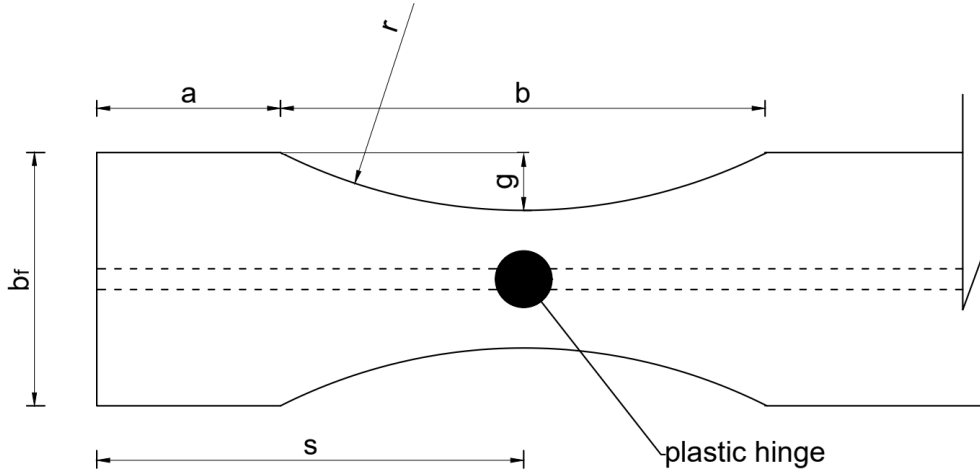


Figure 2.11: Geometry of flange reduction for RBS

- Determine the depth of the flange cut g on each side. According to EN1998-3, this depth should not exceed $0.25b_f$. As first trial, it may be taken as:

$$g = 0.2b_f \quad (2.18)$$

- Compute the plastic modulus Z_{RBS} and the plastic bending moment $M_{pl,Rd,RBS}$ of the plastic hinge section at the centre of the RBS:

$$Z_{RBS} = Z_b - 2gt_f(d_b - t_f) \quad (2.19)$$

$$M_{pl,Rd,RBS} = Z_{RBS} \cdot f_{yb} \quad (2.20)$$

where Z_b is the plastic modulus of the intact beam and f_{yb} is the yield stress of the beam, accounting for its overstrength in the case of new steel or obtained from *in-situ* tests in the case of already existing steel.

- Compute the shear force $V_{Ed,RBS}$ in the section of the plastic hinge formation from equilibrium of the beam part (L_h) between the two intended plastic hinges. For a uniform gravity load $G_k + \psi_{2,i}Q_k$ acting on the beam in the seismic design situation:

$$V_{Ed,RBS} = \frac{2M_{pl,Rd,RBS}}{L_h} + \frac{(G_k + \psi_{2,i}Q_k) \cdot L_h}{2} \quad (2.21)$$

In case of a different gravity load distribution, it should be taken into consideration in equation 2.21.

- Compute the plastic moment away from the RBS, $M_{pl,Rd,b}$ as follows:

$$M_{pl,Rd,b} = Z_b \cdot f_{yb} \quad (2.22)$$

- Verify that $M_{b,pl,Rd}$ is greater than the bending moment that develops at the column face when a plastic hinge forms at the centre of the RBS: $M_{cf,Ed} = M_{pl,Rd,RBS} + V_{pl,RBS} \cdot s$. If it is not, the cut-depth g should be increased and repeat the previous steps. The length b should be chosen so that $M_{cf,Ed}$ is about 85% to 100% of $M_{pl,Rd,b}$

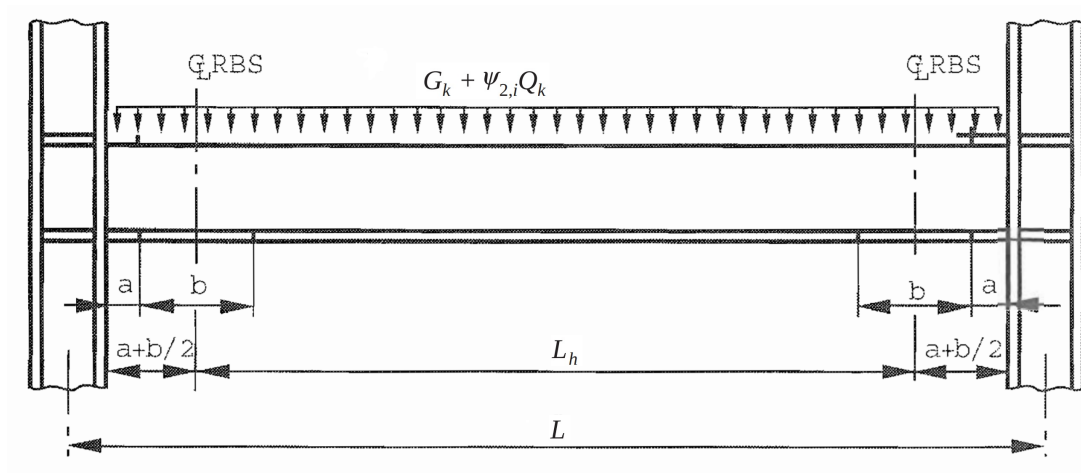


Figure 2.12: Typical sub-frame assembly with reduced beam sections (RBS). Source: EN1998-3. [19]

- Check the width-to-thickness ratios at the RBS to prevent local buckling. The flange width should be measured at the ends of the central two-thirds of the reduced section of the beam.
- compute the radius (r) of the cuts in both top and bottom flanges over the length b of the RBS of the beam:

$$r = \frac{b^2 + 4g^2}{8g} \quad (2.23)$$

- Check that the fabrication process ensures the adequate surface roughness (i.e. between 10 and 15 μm) for the finished cuts and that grind marks are not present.

Other supplementary rules are provided for the use of RBS in composite structures. It must be noted that there is no prequalification in the European framework

for RBS in the Eurocodes, so all steps must be checked carefully in the design. However, in the recent Equaljoints project, a prequalification task was undertaken to apply for European steels and European cross-sections. The result of such task can be found in [48].

2.2.2 RBS in AISC

Much information can be found on RBS in the American standard. Indeed, chapter 5 in AISC358 [2] "Reduced Beam Section (RBS) moment connection" covers all the aspects of RBS design as a prequalified moment-resisting connection. It provides general information on the behaviour of RBS and its intended use in new structures, about the experimental tests for the prequalification task and the prequalification limits for its application in moment-resisting frames with many references to experimental studies.

The prequalification limits are established for the use of RBS in Special (SMF) and Intermediate Moment Frames (IMF). These two categories are similar to the Ductility Class High (DCH) and Ductility Class Medium (DCM) found in the Eurocodes in order to provide a certain level ductility to the structure. Their requirements are divided according to the elements to be applied on:

- Beam limitations. A wide range of sizes were tested for the prequalification. From the relatively small Canadian W530x82 ($d_b=528\text{mm}$, $b_f=209\text{mm}$) up to the largest beam W36x300 ($d_b=948\text{mm}$, $b_f=423\text{mm}$). Although the AISC Seismic Provisions [1] allows for the use of even larger profiles, the prequalification limit is established for the W36x300 cross-section, which was considered to be appropriately conservative.

Beam depth and beam span-to-depth ratio are significant in inelastic behaviour of beam-to-column connections. For the same curvature, deeper beams will experience larger strains. Also, beams with smaller span-to-depth ratio will have a greater moment gradient across the beam span, resulting in reduced length of the beam participating in plastic hinging and increased strains under inelastic rotation demands. Minimum span-to-depth ratios were set to 7 for SMF and to 5 for IMF.

Local buckling requirements are covered in the AISC Seismic Provisions [1]. For the purposes of calculating the width-to-thickness ratio, it is permitted to take the flange width at the two-thirds point of the RBS cut.

Studies indicated that although supplemental bracing is not required at the RBS to achieve the 0.04 rad interstorey drift angles, the addition of supplemental brace can result in improved performance if designed according to Section D1.2b of the AISC Seismic Provisions [1]. In cases where a supplemental brace is provided, it shall be located at or just beyond the end of the RBS that is furthest from the column face.

- Column limitations. The prequalification applies on strong-axis connections only. Most of the prequalification tests were constructed with W14 columns ($d_b=360\text{mm}$). However, more tests were conducted using W18, W27 and W36 columns (with depths 460mm, 690mm and 920mm, respectively). Testing of deep-column specimens under the FEMA/SAC program [21] indicated that stability problems may occur when using RBS connections with deep columns and showed a considerable amount of column twisting, which showed to produce fracture of the column web near the k -area in a few specimens. The k -area is located in the web of the W-shape beam where the flange-to-web root radius becomes tangent with the web. The k -area may have reduced ductility due to cold working at the mill during the fabrication of the steel shape. Also, the k -area is the slowest to cool down after the shape is hot rolled, so it will contain a more coarse microstructure, which can lead to a brittle crack propagation in the k -area [43]. The k -area is shown in figure 2.13 for a hot-rolled HEA240 section:

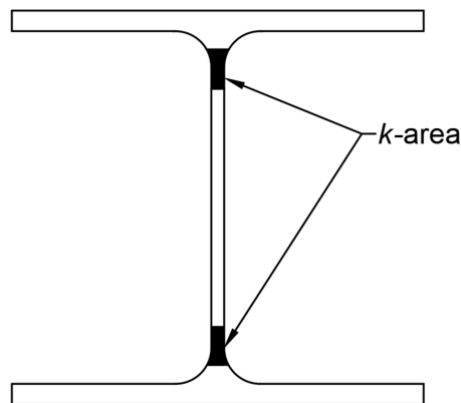


Figure 2.13: k -area of the HEA240 section

After the FEMA/SAC tests, other studies showed that boundary conditions used for the tests may not be representative of what would be found in real buildings, and that the large-column twisting (and presumably, the resultant k -area column fracture) would not be present. It was concluded

that deep columns should not perform differently from the smaller W14 ($d_b=360\text{mm}$) profiles and that no special bracing is required when a slab is present. The prequalification limit was therefore extended to include W36 columns ($d_b=920\text{mm}$).

Also, several tests have been conducted using built-up box columns. The largest box column used was 24in by 24in. (600mm by 600mm). RBS connections have been prequalified for built-up box columns up to 600mm. The limits on the width-to-thickness ratios for the walls of the box columns are specified in Section 2.3.2b(3) in AISC358 [2] and were chosen to match the columns tested.

- Column-beam relationship limitations. The strength of the panel zone on RBS specimen has varied on a wide range. Good performance has been achieved for all levels of panel zone strength, including panel zones weaker than permitted in the AISC Seismic Provisions [1]. There are concerns that very weak panel zones may promote fracture near the beam-flange groove welds due to "kinking" of the column flanges at the boundaries of the panel zone. The minimum strength for the panel zone is specified in Section E3.6e of the AISC Seismic Provisions [1].
- Beam flange-to-column flange weld limitations. It is indicated that RBS connections are not particularly sensitive to weld access hole geometry, and therefore the regular requirements found in Section 6.11 of AWS D1.8/D1.8M [7] should be satisfied.
- Beam web-to-column connection limitations. Two types of web connection details have been used for RBS specimens. One with a welded web using a complete-joint-penetration (CJP) groove weld, the other being a bolted detail with pretensioned high-strength bolts. Many tests have been conducted on both joint typologies and while the welded detail has consistently provided satisfactory results in terms of interstorey drift angles, contradictory and inconclusive results have been obtained with the bolted detail. Until further data are available, a welded web connection is required for RBS connections prequalified for SMF. For IMF applications, bolted web connections can be used.
- Fabrication of flange cuts. Due to the experimental evidence of its superior performance, only the radius cut geometry is prequalified. Finish and smoothness requirements for RBS connections are consistent with those in FEMA 350 [22].

- Design procedure. The design procedure in Section 5.8 of AISC 358 [2] is very similar to that found in EN1998-3 [19]. It is also indicated that a slight slope in the beams does not negatively impact RBS performance. However, a limiting angle for that assumption has not been determined.

3 Study on the local behaviour of the RBS

3.1 General

In this section, a study on the local behaviour of the RBS is performed. A numerical model is developed in order to assess the behaviour of the dog-bone and a parametric study is used to find the influence of several relevant design parameters on its response. 158 beam-to-column assemblies are generated with varying parameters. The investigated parameters are the beam cross-section, the steel grade, the trimmed flange width (or the cutout portion of the flanges) and the column web panel strength.

The geometries adopted in this study are a series of beam-to-column assemblies with a radius cut in the beam flanges. The column is fixed on both ends and the beam is fixed to the column flange as a cantilever. The column cross-sections have been selected to provide sufficient flexural overstrength over the beam, following the widely known weak beam - strong column design approach. At the beam free end the load is applied in the form of a variable imposed rotation with increasing steps, following the Equaljoints cyclic loading protocol [48].

The choice of the Equaljoints cyclic protocol over the widely used ANSI/AISC341-16 protocol [1] stems from the fact that it is capable of reproducing the European seismic available data in a more reliable manner. It was developed within the Equaljoints project specifically for the prequalification of European connections, using European steel profiles and steel grades.

After the results of the 158 simulations are exposed, a detailed analysis is performed. The influence of each of the investigated parameters on the response of the RBS is evaluated. The main results to focus on in this study are the moment-rotation diagram (with special attention to the maximum bending moment $M_{max,RBS}$, the bending moment at 40mrad rotation $M_{40,RBS}$ and their comparison with respect to the design bending resistance $M_{Rd,RBS}$). The dissipated plastic work and the longitudinal stress at the welded flange-to-flange connection are also compared among the different cases of study.

The software *Abaqus* was used in the simulations. It is a general-purpose finite-element analyser that employs implicit integration scheme. A general static analysis approach was used in all the simulations. The solution at each load increment was obtained by means of a direct full-Newton equation solver.

3.2 Definition of the numerical model

3.2.1 Geometries

The length of the members has been defined in such a way so that any potential local effects that may occur take place far away from the connection area and the RBS area while trying to keep them as short as possible in order to avoid a very high computational cost. For that reason, the distance from the end of the RBS to the beam end has been adopted as $2d_b$ (double of the beam depth) and the distance from the beam flange to each of the column ends has been adopted as $2d_c$ (double of the column depth).

The analysed specimens are beam-to-column assemblies using European steels and European cross-section geometries, with the beam members being hot-rolled profiles from the families IPE and HEA, a built-up slender section and an American Jumbo section. The column sections have been chosen in such a way that a sufficient flexure overstrength is guaranteed according to usual seismic design practice, and belonging to the HEB and HEM families and another Jumbo section in the case of the Jumbo beam section. In figure 3.1 a schematic of the assemblies can be seen:

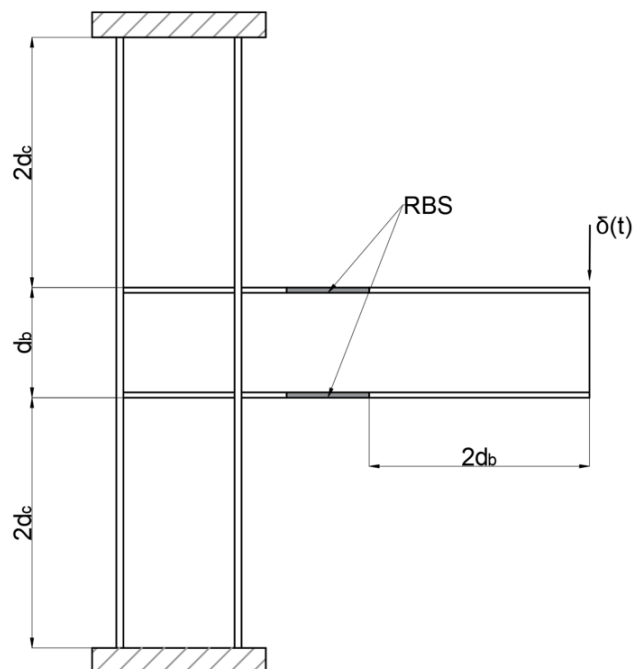


Figure 3.1: Schematic of the assemblies.

In the next figure the main parameters of the RBS can be observed.

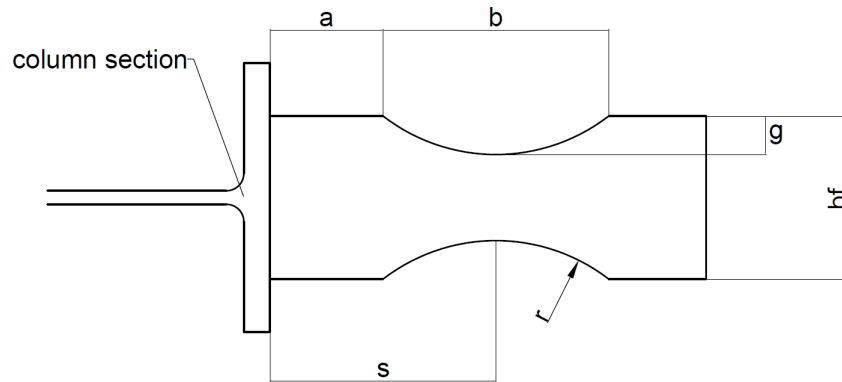


Figure 3.2: Scheme of the geometry of a Reduced Beam Section

In figure 3.2 b_f stands for the beams flange width, d_b the beams depth, a is the distance between the column flange and the start of the trimmed part of the beam flange, b is the length of the RBS, g is the maximum trimmed flange width, s is the distance between the column flange and the center of the RBS and r is the radius of the circular cut.

The doubler plates in the panel zone were modelled with a single shell with its thickness equal to the sum of the thicknesses of the column web and the doubler plates according to the panel strength ratio for each case (see section 3.3.4). The welds are not accounted for in the model. Instead, the beam-to-column joint is achieved by merging the geometry and making both beam and column share a group of nodes as if they were a single member. Weld access holes were modelled and designed according to AISC 358 [2], AWS D1.1 [6] and AWS D1.8 [7] specifications.

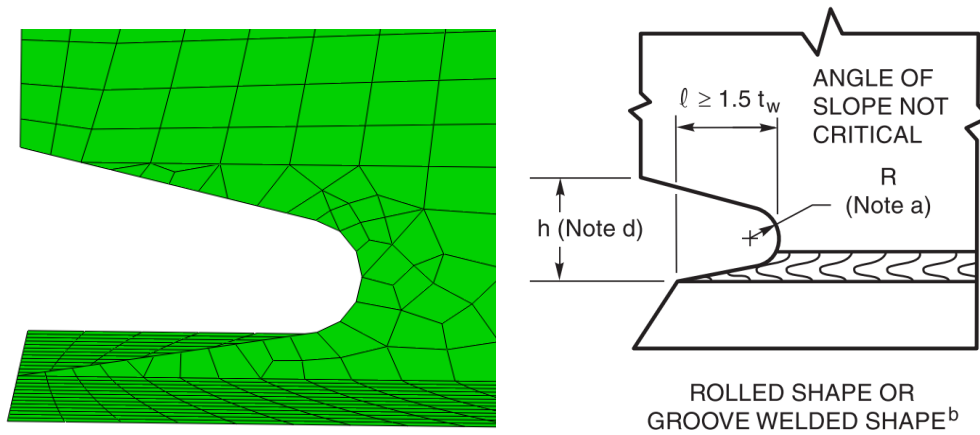


Figure 3.3: Modelling of the web access holes (left) and design guidelines for the weld access holes (right) [6]

3.2.2 Loading of the specimens

The simulations were performed applying a variable displacement at the tip of the beam so that total interstorey drift rotations in the beam were achieved according to table 3.1, following the Equaljoints protocol. This loading protocol originated in the Equaljoints research project for the prequalification of European bolted steel joints. Although the ANSI/AISC341-16 is more widely known and used, the Equaljoints is used in this study since it better represents the available European seismic data and the steel grades and cross-sections used are all European. It has been found that the results obtained with both protocols are in fact quite similar [48]. It can be observed that the number of cycles at each imposed rotation is different from the AISC 341-16 protocol [1].

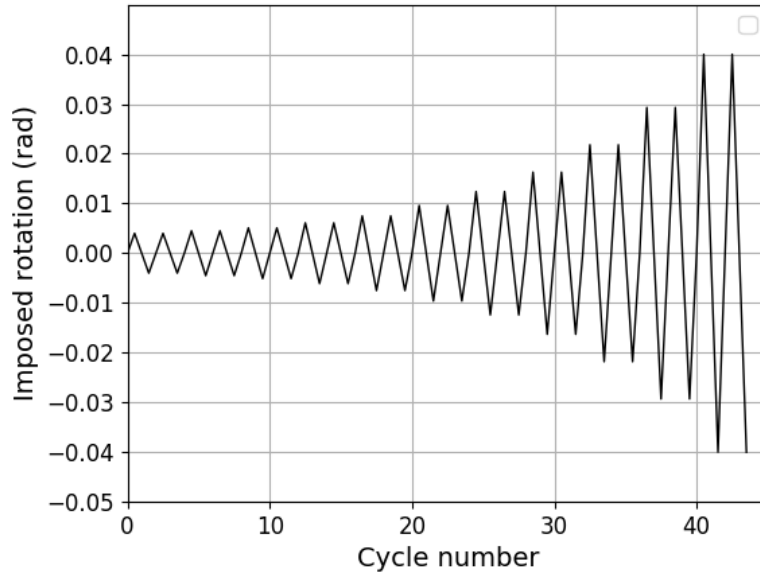


Figure 3.4: Equaljoints cyclic loading protocol

Table 3.1: Equaljoints cyclic loading protocol

Load step	Number of cycles	Interstorey drift rotation θ (rad)
1	2	0.004
2	2	0.0045
3	2	0.0051
4	2	0.0061
5	2	0.0075
6	2	0.0096
7	2	0.0124
8	2	0.0163
9	2	0.0218
10	2	0.0293
11	2	0.040

3.2.3 Mesh and boundary conditions

The beam-to-column assemblies were modelled using S4R shell elements in Abaqus and 5 integration points across their thickness. The shells were located in the mid-

dle plane of the plates. The root between flanges and web was modelled as a small area with a thickness larger than the web so that the total cross-sectional area in the model is in accordance with that of the real profile. The column was modelled as fixed at both ends by means of two reference points located at the end sections in the middle of the web. All the nodes in the section at the supports of the column are then forced to behave in the same way as the reference point. The beam is free with the only exception of a lateral restraint at the tip to avoid any lateral-torsional buckling of the whole span of the beam.

The specimens were meshed with the smallest elements located at the RBS and the weld access holes, while the column and beam ends were meshed using larger elements to reduce computational cost. Figures 3.5 and 3.6 show the mesh configuration for the model.

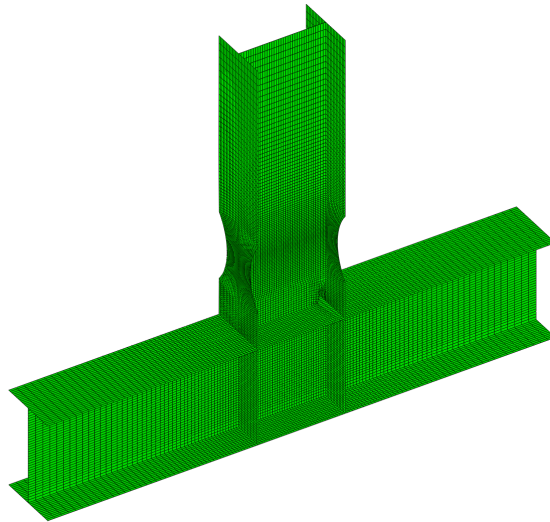


Figure 3.5: General view of the mesh of the model

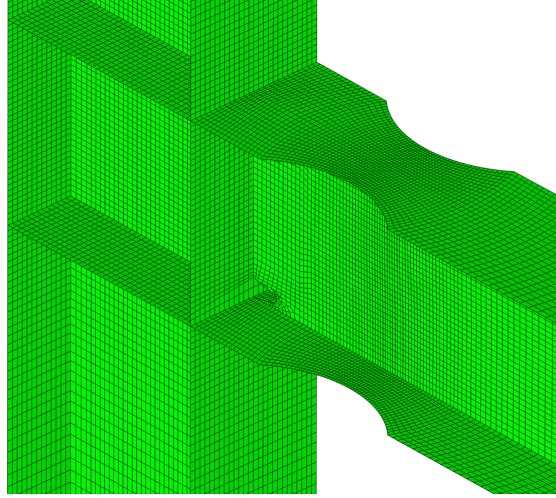


Figure 3.6: Close up view of the mesh of RBS area

3.2.4 Constitutive law of the material

Due to the variable nature of the load protocol to introduce and in order to assess the cyclic behaviour of the RBS, the material model to be used must account for the cyclic hardening of the steel material in order to reproduce accurately the phenomena that take place during the simulated tests. The material used in the numerical model is a nonlinear isotropic/kinematic hardening model, based on the work of Lemaitre and Chaboche [37]. Using the Von Mises yield criterion, the yield surface is defined as:

$$f = J_2(\boldsymbol{\sigma} - \boldsymbol{\alpha}) - \sigma^0 = 0 \quad (3.1)$$

where σ^0 is the size of the yield surface and $J_2(\boldsymbol{\sigma} - \boldsymbol{\alpha})$ is the equivalent Von Mises stress with respect to the backstress $\boldsymbol{\alpha}$.

$$J_2(\boldsymbol{\sigma} - \boldsymbol{\alpha}) = \sqrt{\frac{3}{2}(\boldsymbol{\sigma}^{dev} - \boldsymbol{\alpha}^{dev}) : (\boldsymbol{\sigma}^{dev} - \boldsymbol{\alpha}^{dev})} \quad (3.2)$$

where $\boldsymbol{\sigma}$ is the stress tensor and $\boldsymbol{\sigma}^{dev}$ and $\boldsymbol{\alpha}^{dev}$ are the deviatoric parts of the stress and backstress tensors, respectively. The operator ":" stands for the double dot product of two tensors.

The isotropic behaviour controls the size of the yield surface σ^0 as a function of the equivalent plastic strain $\bar{\varepsilon}^{pl}$, which can be modelled as an exponential law:

$$\sigma^0 = \sigma|_0 + Q_\infty(1 - e^{-b\bar{\varepsilon}^{pl}}) \quad (3.3)$$

where Q_∞ and b are material parameters to be calibrated from cyclic tests data. Q_∞ determines the maximum possible expansion of the yield surface, b determines the rate at which the yield surface expands as plastic strains develop and $\sigma|_0$ is the size of the yield surface at zero plastic strain.

The kinematic hardening behaviour is defined as the sum of a linear kinematic term (known as the Ziegler hardening law) and a second term introducing the nonlinearity, also known as the "relaxation term". The overall backstress is composed of multiple components, and their evolution is defined as:

$$\dot{\alpha}_k = C_k \dot{\varepsilon}^{pl} \frac{1}{\sigma_0} (\sigma - \alpha) - \gamma_k \alpha_k \dot{\varepsilon}^{pl} \quad (3.4)$$

and the overall backstress is computed as follows:

$$\alpha = \sum_{k=1}^n \alpha_k \quad (3.5)$$

where n is the number of backstresses and C_k and γ_k are material parameters. C_k is the k -th kinematic hardening module, while γ_k determines the rate at which the kinematic hardening module C_k decreases as plastic strains increase.

3.2.5 Validation of the numerical model

After the initial check with a perfect elastic behaviour, the non-linear material properties were tested. The numerical model was then validated by reproducing an experimental test performed in the Equaljoints project. The experimental test consists of a beam-to-column assembly consisting of a W44x230 beam ($d_b=1090\text{mm}$, $b_f=401\text{mm}$, $t_f=31\text{mm}$) and a W14x342 column ($d_b=445\text{mm}$, $b_f=417\text{mm}$, $t_f=63\text{mm}$) in Grade 50 steel ($f_y = 345\text{MPa}$). Doubler plates were adopted in the test with a thickness of 5/8 inches and continuity plates were 3/4 inches. All the details of the test can be found in [48]. The specimen can be seen in figure 3.7:

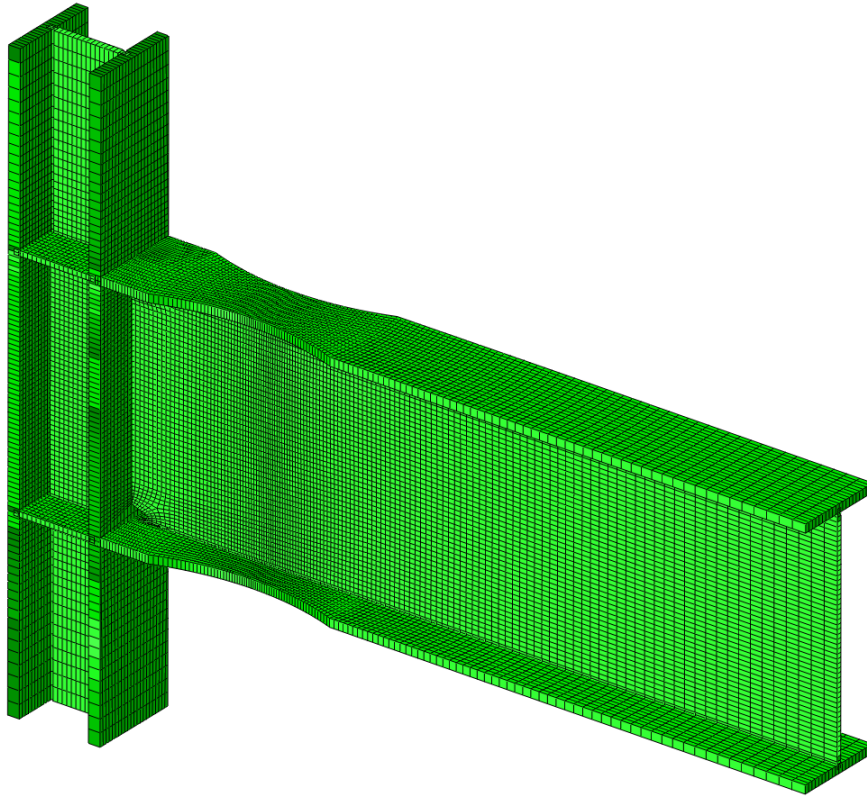


Figure 3.7: Modelling of the specimen in the test in the Equaljoints project [48]

The material used in the simulation was obtained from the literature [33], corresponding to a S355 steel with nonlinear isotropic-kinematic hardening. The values used are in table 3.2.

Table 3.2: Parameters for the definition of the properties of steel S355. Source: Krolo et al. [33]

Material	E	ν	$\sigma _0$	C_1	γ_1	C_2	γ_2	C_3	γ_3	Q_∞	b
	(MPa)		(MPa)	(MPa)		(MPa)		(MPa)		(MPa)	
S355	210000	0.3	386	5327	75	1725	16	1120	10	20.8	3.2

The loading protocol adopted for the test was the displacement loading protocol in AISC341-16 [1]. The cyclic loading protocol rotations (in rad) are represented in figure 3.8, and the corresponding displacements were introduced at the beam end.

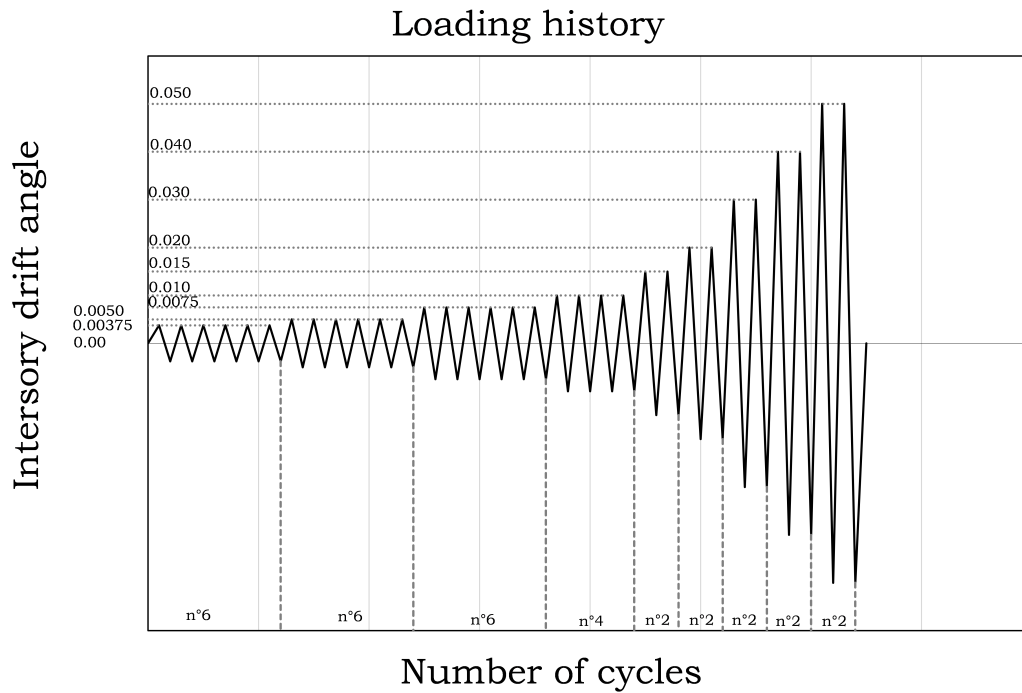


Figure 3.8: Cyclic loading protocol in AISC341-16 [1]. Source: FreeDam Plus project [49]

For this particular test, the protocol was followed until the 0.050rad cycles were reached. At that stage of the test a total of 5 cycles at 0.050rad were performed and the test was then stopped. Figures 3.9 and 3.10 show the moment-rotation diagrams obtained in the test from the Equaljoints project [48] and the curve obtained numerically in the present study, respectively.

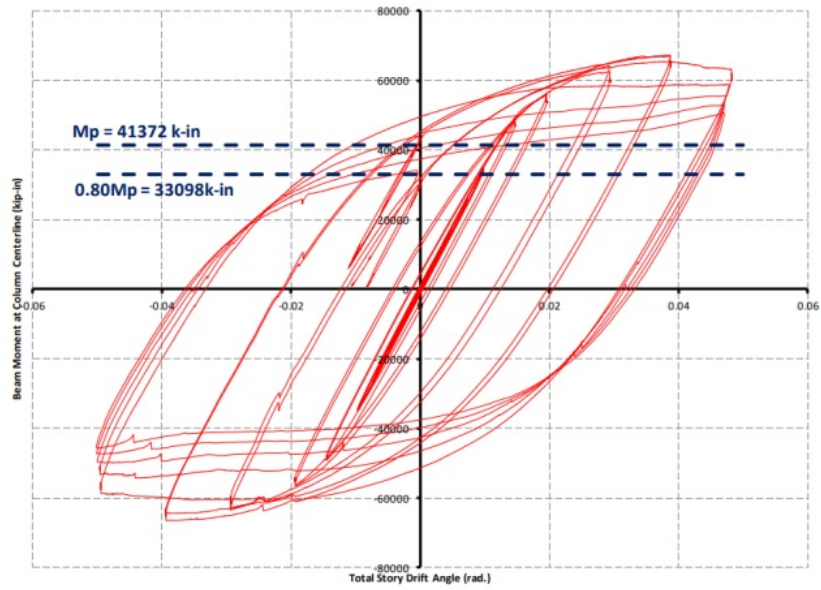


Figure 3.9: Moment-rotation curve obtained in the test in the Equaljoints project [48]

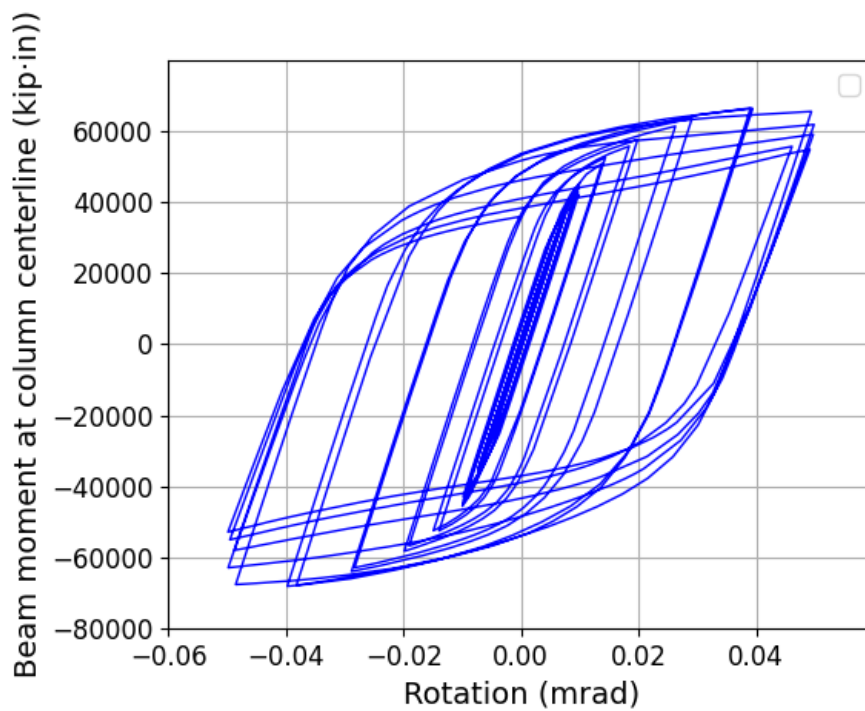


Figure 3.10: Moment-rotation curve obtained in the present study using Abaqus

The results of the validation show that the numerical model developed for this study is in very good agreement with the experimental test, even after several cycles at very high rotations, clearly greater than those achieved in the simulations performed in this study.

The experimental tests performed in [15] are also used to validate the numerical model in Abaqus. Specifically, specimen a) was reproduced. These tests consist of a beam-to-column assembly (see figure 3.11) with a radius cut RBS connection with the tip of the beam subjected to a variable imposed displacement according to the AISC/SAC loading protocol. The profiles involved are HEB300 section as the column and IPE450 section as the beam. The connection has doubler plates in the column web and continuity plates. The parameters defining the radius cut are shown in table 3.3.

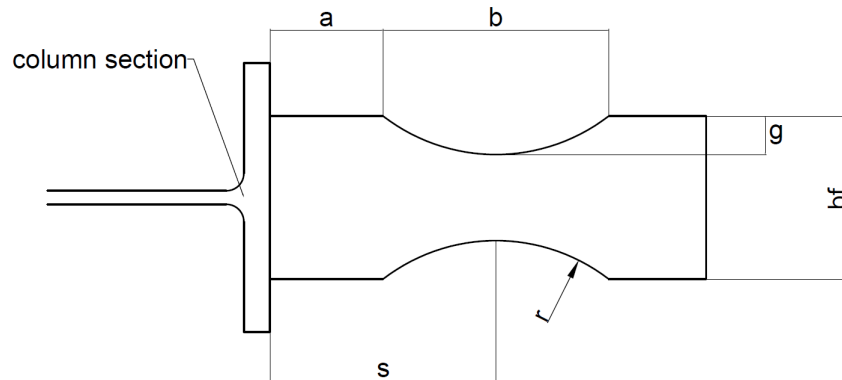


Figure 3.11: Scheme of the geometry of a Reduced Beam Section

Table 3.3: Parameters of the dog-bone joint for the validation of the numerical model [5] (RBS1-S). Dimensions in mm

b_f	d_b	a	b	g	s	r
190	450	100	350	45	275	362.8

The values in table 3.3 are based upon the design guidelines in EN1998-3 [19] and are dependent on the flange width b_f and beam depth d_b . The beam had a span of 2750 mm with the displacement imposed with adequate stiffening of the loading area. The steel used in the tests had a yield stress $f_y = 314 N/mm^2$. The material introduced in the software was based upon the data available in [15] and

the hardening law applied was combined nonlinear kinematic. Table 3.4 shows the material parameters used for this validation.

Table 3.4: Parameters for the definition of the properties the steel for the test in [15]

E	ν	$\sigma _0$	C_1	γ_1	C_2	γ_2	C_3	γ_3	Q_∞	b
(MPa)		(MPa)	(MPa)		(MPa)		(MPa)		(MPa)	
210000	0.3	314	13921	765	4240	52	1573	14	25.6	4.4

The tests were performed applying a variable displacement at the tip of the beam so that total rotations in the beam were achieved (see table 3.5). The following table shows the loading protocol used in the tests.

Table 3.5: SAC cyclic loading protocol [1]

Load step	Peak rotation (mrad)	Number of cycles, n
1	3.75	6
2	5	6
3	7.5	6
4	10	4
5	15	2
6	20	2
7	30	2
Increase rotation by 10mrad with two cycles per step		

The beam-to-column assemblies were modelled using S4R shell elements in Abaqus, located in the middle plane of the plates. The column was modelled as pinned at both ends. The beam is free with the only exception of a lateral restraint to avoid any lateral-torsional bucking of the whole span of the beam. The doubler plates in the panel zone were modelled with a single shell with its thickness equal to the sum of the thicknesses of the column web and the doubler plates. The welds are not accounted for in the model. Further details can be found in [31].

The mesh (see figure 3.12) was more refined at the areas in which stress and strain concentrations and large gradients were expected.

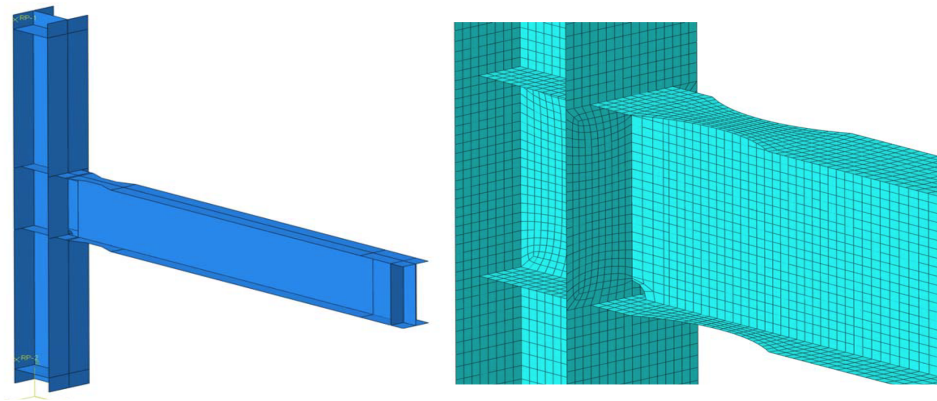


Figure 3.12: Visualisation of the model of the beam-to-column assembly with RBS (left). Detail of the mesh of the model (right)

The load protocol was introduced as a quasi-statically imposed displacement (see table 3.5). Buckling shapes were accounted for in the analysis. A small imperfection was given to the beam to reproduce the local buckling of the web and flanges. In figure 3.13, a comparison is made between the failed specimen in the laboratory and the numerical model developed.

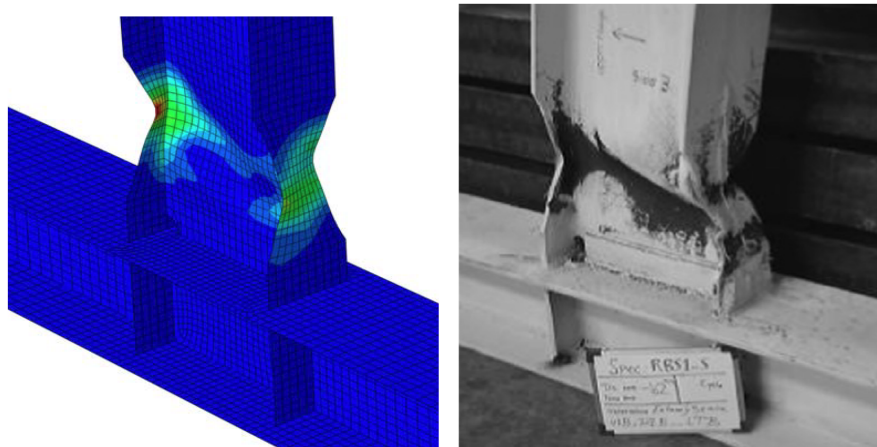


Figure 3.13: Comparison between the numerical model (left, equivalent plastic strains (PEEQ) displayed, present study) and the specimen in the laboratory (right, source: Deylami et al [15]).

Figure 3.14 shows the comparison of the moment-rotation curves in [15] and the ones obtained in the numerical model presented in this study [31].

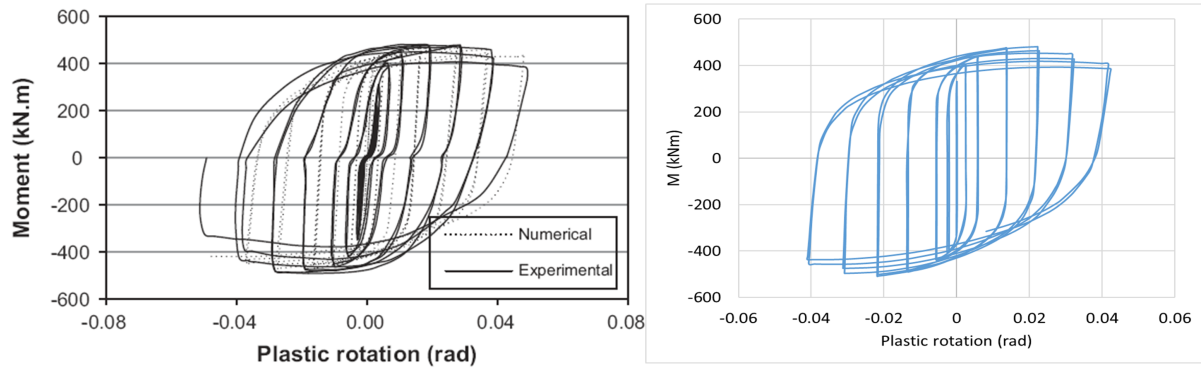


Figure 3.14: Comparison between moment-rotation diagrams (left, source: Deylami et al [15]) and present study

As it can be observed in figure 3.14, very good agreement was achieved between the numerical model developed in this study and both the laboratory test and the numerical analysis in [15].

3.3 Parametric study

The behaviour of a RBS under a cyclic load is dependant on a wide variety of factors: geometrical parameters, material parameters, component strength hierarchy, component stiffness, among others. In this study it will be considered that the welded connection is full-strength and fully rigid. This consideration allows the dog-bone to shine by concentrating plastic strains in the RBS away from the connection. In this study, the welded joint is assumed to work perfectly, with sufficiently small residual stresses (which tend to dissipate as the loading cycles invert the load [36]) and with no defects that may lead to brittle fracture. Fatigue phenomena are also not taken into account. In order to investigate the response of a RBS under cyclic loading with a wide range of different parameters, a total number of 158 simulations have been performed.

3.3.1 Studied cross-sections

Due to the different width-to-thickness ratios of different cross-sections it is expected that a RBS will have a different behaviour when applied to a certain profile or another. With that in mind, several different cross-sections have been included. The selection of profiles studied here will provide a range of web and flange slendernesses for the study of RBS on hot-rolled profiles, as well as a built-up slender girder.

The profiles of study consist of hot-rolled profiles from the IPE and HEA families, as well as a built-up plate girder with depth $d = 1200mm$ and an American Jumbo section W44x408 ($d_b=1138mm$, $b_f=410mm$, $t_f=55mm$). In all cases the beams are paired with column members strong enough to provide enough flexural overstrength, following common practice for structural seismic design. 9 different assemblies (beam and column pairs) have been studied in this study. All the details can be found below:

- European hot-rolled sections:

- IPE450 - HEB340

Table 3.6: Assembly 1 details.

Beam: IPE450		Column: HEB340	
$h_b = 450mm$	$t_{f,b} = 14.6mm$	$h_c = 340mm$	$t_{f,c} = 21.5mm$
$b_b = 190mm$	$t_{w,b} = 9.4mm$	$b_c = 300mm$	$t_{w,c} = 12.0mm$
$r_b = 21mm$	$W_{pl,b} = 1701.9cm^3$	$r_c = 27mm$	$W_{pl,c} = 2408.3cm^3$

- HEA450 - HEB500

Table 3.7: Assembly 2 details.

Beam: HEA450		Column: HEB500	
$h_b = 440mm$	$t_{f,b} = 21.0mm$	$h_c = 500mm$	$t_{f,c} = 28.0mm$
$b_b = 300mm$	$t_{w,b} = 11.5mm$	$b_c = 300mm$	$t_{w,c} = 14.5mm$
$r_b = 27mm$	$W_{pl,b} = 3216.1cm^3$	$r_c = 27mm$	$W_{pl,c} = 4814.8cm^3$

- IPE600 - HEB500

Table 3.8: Assembly 3 details.

Beam: IPE600		Column: HEB500	
$h_b = 600mm$	$t_{f,b} = 19.0mm$	$h_c = 500mm$	$t_{f,c} = 28.0mm$
$b_b = 220mm$	$t_{w,b} = 12.0mm$	$b_c = 300mm$	$t_{w,c} = 14.5mm$
$r_b = 24mm$	$W_{pl,b} = 3512.7cm^3$	$r_c = 27mm$	$W_{pl,c} = 4814.8cm^3$

- HEA600 - HEM550

Table 3.9: Assembly 4 details.

Beam: HEA600		Column: HEM550	
$h_b = 590mm$	$t_{f,b} = 25.0mm$	$h_c = 572mm$	$t_{f,c} = 40.0mm$
$b_b = 300mm$	$t_{w,b} = 13.0mm$	$b_c = 306mm$	$t_{w,c} = 21.0mm$
$r_b = 27mm$	$W_{pl,b} = 5350.7cm^3$	$r_c = 27mm$	$W_{pl,c} = 7933.0cm^3$

- IPE750x196 - HEM700

Table 3.10: Assembly 5 details.

Beam: IPE750x196		Column: HEM700	
$h_b = 770mm$	$t_{f,b} = 25.4mm$	$h_c = 716mm$	$t_{f,c} = 40.0mm$
$b_b = 268mm$	$t_{w,b} = 15.6mm$	$b_c = 304mm$	$t_{w,c} = 21.0mm$
$r_b = 17mm$	$W_{pl,b} = 7174cm^3$	$r_c = 27mm$	$W_{pl,c} = 10540cm^3$

- HEA800 - HEB900

Table 3.11: Assembly 6 details.

Beam: HEA800		Column: HEM900	
$h_b = 790mm$	$t_{f,b} = 28.0mm$	$h_c = 910mm$	$t_{f,c} = 40.0mm$
$b_b = 300mm$	$t_{w,b} = 15.0mm$	$b_c = 302mm$	$t_{w,c} = 21.0mm$
$r_b = 30mm$	$W_{pl,b} = 8699cm^3$	$r_c = 30mm$	$W_{pl,c} = 14440cm^3$

- HEA1000 - HE1000x393

Table 3.12: Assembly 7 details.

Beam: HEA1000		Column: HE1000x393	
$h_b = 990mm$	$t_{f,b} = 31.0mm$	$h_c = 1016mm$	$t_{f,c} = 43.9mm$
$b_b = 300mm$	$t_{w,b} = 16.5mm$	$b_c = 303mm$	$t_{w,c} = 24.4mm$
$r_b = 30mm$	$W_{pl,b} = 12820cm^3$	$r_c = 30mm$	$W_{pl,c} = 18540cm^3$

- Slender built-up members:

- Built-up girder - W44x262

Table 3.13: Assembly 8 details.

Beam: Built-up girder		Column: W44x262	
$h_b = 1200mm$	$t_{f,b} = 20.0mm$	$h_c = 1100mm$	$t_{f,c} = 36.0mm$
$b_b = 400mm$	$t_{w,b} = 10.0mm$	$b_c = 400mm$	$t_{w,c} = 20.0mm$
$a = 6mm$	$W_{el,b} = 11451.5cm^3$ $W_{eff,b} = 11015.3cm^3$	$r_c = 20mm$	$W_{pl,c} = 20780cm^3$

- American Jumbo sections:

- W44x408 - W44x593

Table 3.14: Assembly 9 details.

Beam: W44x408		Column: W44x593	
$h_b = 1138mm$	$t_{f,b} = 55.0mm$	$h_c = 1092mm$	$t_{f,c} = 82.0mm$
$b_b = 410mm$	$t_{w,b} = 31.0mm$	$b_c = 424mm$	$t_{w,c} = 45.5mm$
$r_b = 30mm$	$W_{pl,b} = 33000cm^3$	$r_c = 20mm$	$W_{pl,c} = 45260cm^3$

The choice of these cross-sections for their study is based on the limited available data on large sections with RBS. Not only are studies with European cross-sections few, but they only study cross-sections with small depths ($d_b \leq 400mm$), which are the most commonly used. In this study, hot-rolled cross-sections are considered ranging from $450mm \leq d_b \leq 1000mm$, with an intended use for beams with spans ranging from 9m up to 20m. These larger sections are not so commonly used, and even profiles with depths above 500mm are often not readily available in stock and are only available on special order. Also, two larger sections are considered for more extreme applications: a built-up slender girder with $d_b = 1200mm$ and a hot-rolled American Jumbo section with $d_b = 1138mm$.

Another consideration when opting to study the largest profiles stems from the fact that for a given curvature, the members with greater depths will experience larger strains. This effect may aggravate any instability phenomena in the beam and it makes studying these cross-sections even more necessary.

It is expected that the most compact specimens will behave the best, exhibiting stable hysteresis loops and avoiding or delaying the onset of any instabilities. Therefore, among the hot-rolled European profiles it is expected that the largest ones, especially those in the IPE family, have a poor performance relative to their HEA counterparts. For that same reason, the slender built-up girder is expected to have a poor response due to the slenderness of its panels and the robust Jumbo section is expected to perform very well since the width-to-thickness ratios of its panels are very small.

3.3.2 Steel grades

Another factor than can influence the response under bending and shear is the steel grade. The yield stress f_y and the hardening modulus $E(\varepsilon^{pl})$ are two parameters

to be taken into account. Also, the cyclic behaviour of each material is known to be unique, which also plays an important role in the cyclic behaviour of the RBS. In this study, two different materials widely used in European constructional steelwork are studied, with grades S235 and S355. In the elastic regime, all the steels have a Poisson ratio $\nu = 0.3$. The rest of the values completing the full isotropic/kinematic hardening law for each material have been obtained from the literature. The values used are indicated in the tables below.

Table 3.15: Parameters for the definition of the properties of steel S355. Source: Krolo et al. [33]

Material	E (MPa)	ν	$\sigma _0$ (MPa)	C_1 (MPa)	γ_1	C_2 (MPa)	γ_2	C_3 (MPa)	γ_3	Q_∞ (MPa)	b
S355	210000	0.3	386	5327	75	1725	16	1120	10	20.8	3.2

Table 3.16: Parameters for the definition of the properties of steel S235. Source: Hos et al. [28]

Material	E (MPa)	ν	$\sigma _0$ (MPa)	C_1 (MPa)	γ_1	C_2 (MPa)	γ_2	C_3 (MPa)	γ_3
S235	214000	0.3	310	13442	46	39134	400	72245	1904
	C_4 (MPa)	γ_4	C_5 (MPa)	γ_5	Q_∞ (MPa)	b			
	603494	7404	800707	704861	58.2	1.12			

3.3.3 Radius cut geometry

Another crucial parameter in the response of the RBS is the geometry of the trimmed portion of the beam flanges, as well as its exact location relative to the column flange. Following the rules in EN1998-3 [19] the distance of the start of the flange reduction from the column flange a and the length over which the beam flange will be trimmed b are considered as follows, for all studied cases:

$$a = 0.60b_f \quad (3.6)$$

$$b = 0.75d_b \quad (3.7)$$

Instead, the parameter to study will be the trimmed flange width g . Three different cases are analyzed:

- $g = 0.2b_f$. The remaining net flange width in this case is $b_{f,RBS} = 0.6b_f$.
- $g = 0.25b_f$. The remaining net flange width in this case is $b_{f,RBS} = 0.5b_f$.
- $g = 0.3b_f$. The remaining net flange width in this case is $b_{f,RBS} = 0.4b_f$.

This choice of trimmed flange widths offers the chance to study a given beam-to-column assembly when only the RBS net plastic modulus $W_{pl,RBS}$ is varied, with three different possible values for each assembly. Annex B of EN1998-3 [19] recommends against adopting values for $g > 0.25b_f$. The value $g = 0.3b_f$ has been purposefully included in order to gather data for those "non-compliant" cases and evaluate if the results obtained support or oppose to the stance in EN1998-3 [19].

3.3.4 Column web panel strength

As mentioned in section 2.1.1, connection component hierarchy is crucial to ensure the desired structural behaviour. In the case of study, the connection will always be full strength, and no damage will be accepted in the connection. However, for the column web panel different design objectives will be investigated. In order to do so, a column web panel strength ratio r is defined as

$$r = \frac{V_{wp,Rd} \cdot z_b}{M_{con,Ed}} \quad (3.8)$$

where $V_{wp,Rd}$ is the column web panel strength, z_b is the distance between the centers of gravity of the beam flanges and $M_{con,Ed}$ is the maximum expected bending moment in the beam located at the connected section. $M_{con,Ed}$ is to be obtained by using expression 2.2 with $\gamma_{sh} = 1.1$ (following the recommendations in EN1998-1 [18]) and $\gamma_{ov} = 1.25$. $V_{wp,Rd}$ may be calculated as (EN1993-1-8 clause 6.2.6.1 [17])

$$V_{wp,Rd} = \frac{0.9f_{y,wc}A_{v,c}}{\sqrt{3}\gamma_{M0}} \quad (3.9)$$

where $f_{y,wc}$ is the yield stress of the column web panel steel and $A_{v,c}$ is the shear area of the column. This resistance may be increased by the use of stiffeners or supplementary web plates. Ideally, when transverse web stiffeners are used in both the tension and compression zones, it is possible to achieve a failure mechanism with shear failure of the panel zone and four local plastic hinges located at the column flanges due to the large distortion of the web panel. Thus, provided the stiffeners have sufficient strength the web panel shear strength may be increased by $V_{wp,add,Rd}$:

$$V_{wp,add,Rd} = \frac{4M_{pl,fc,Rd}}{d_s} \leq \frac{2M_{pl,fc,Rd} + 2M_{pl,st,Rd}}{d_s} \quad (3.10)$$

where d_s is the lever arm between the stiffeners, $M_{pl,f_c,Rd}$ is the design plastic flexural resistance of a single column flange and $M_{pl,st,Rd}$ is the design plastic flexural resistance of a single stiffener. Figure 3.15 shows a schematic of the failure mechanism.

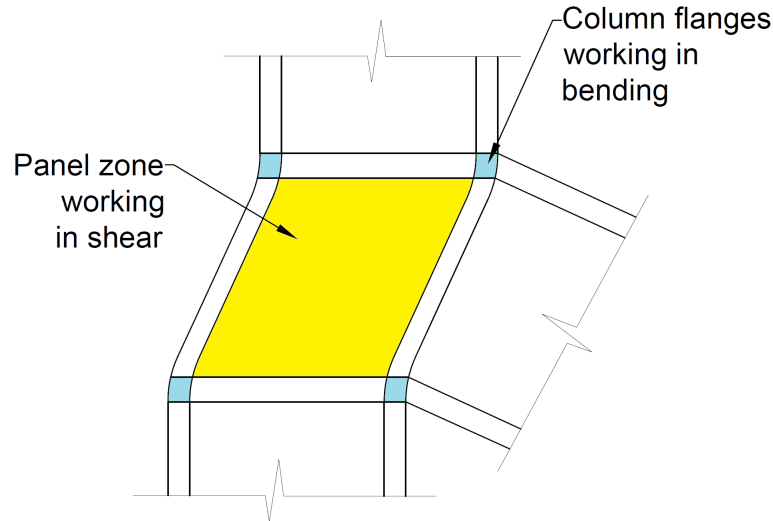


Figure 3.15: Schematic of the failure mechanism of the web panel zone. The web panel of the column (yellow) is carrying mostly shear, while the flanges (blue) are carrying bending

The design of the assemblies is undertaken with common seismic design practice in mind, which implies pairing columns with substantial flexural overstrength on the attached beams. However, in most cases, the column web panel strength ratio r happens to be smaller than 1, which implies that the column web panel is weak and prone to developing plastic strains. In order to ensure that a wide variety of strength ratios r are studied for each assembly, the following cases are studied:

- Assemblies with no column web panel doubler plates. This usually provides weak column web panels ($r \lesssim 1$).
- Assemblies with column web panel doubler plates. Their thickness will be such that the following r values are obtained:
 - $r = 1$. Equal strength panel zone is imposed.
 - $r = 1.3$. Strong panel zone is imposed with substantial overstrength.
 - $r = 1.6$. Very strong panel zone is imposed with high overstrength.

Following these lines, for each particular assembly, steel grade and RBS radius cut geometry, there will be 4 different column web panel strength ratios r . For some assemblies fewer web panel ratios have been generated, since some cases provide no additional information. For instance, for an assembly where the unreinforced web panel as is provides a ratio $r = 0.97$, the value $r = 1$ has been skipped since it would provide no additional information to the result of the unreinforced case.

Also, other cases have not been generated for the larger profiles. When the column web is of great thickness, it makes no practical sense to add two supplementary doubler plates of very small thicknesses each just to comply to a given r ratio. In those cases, only the largest values 1.3 and/or 1.6 have been generated.

3.4 Results

In this section, the results obtained from the 158 simulations are displayed. Moment-rotation curves, maximum bending moments, degraded bending moments (at 40mrad rotation), longitudinal weld stresses and dissipated plastic work have been obtained for each analysed case. For the sake of brevity, only a few cases will be fully displayed in this section. However, charts and tables are provided with the summary of the results of all the simulations.

All bending moments displayed hereinafter are all referred to the RBS central section. For a more simple notation the "RBS" subindex will be omitted. Therefore quantities like $M_{max,RBS}$ will simply be expressed as M_{max} .

3.4.1 Detailed results for HEA600 beam, $r = 0.833$, $g = 0.2b_f$, S355

In this subsection, the full results of a HEA600 - HEM550 beam-to-column assembly are presented. This particular case corresponds to an unreinforced column web panel with $r = 0.833$, a trimmed width of the flanges at each side $g = 0.2b_f$ and S355 steel grade. After the analysis, the moment-rotation diagram provides with a lot of information on the behaviour of this assembly with this specific RBS and panel strength configuration, which can be seen in figure 3.16.

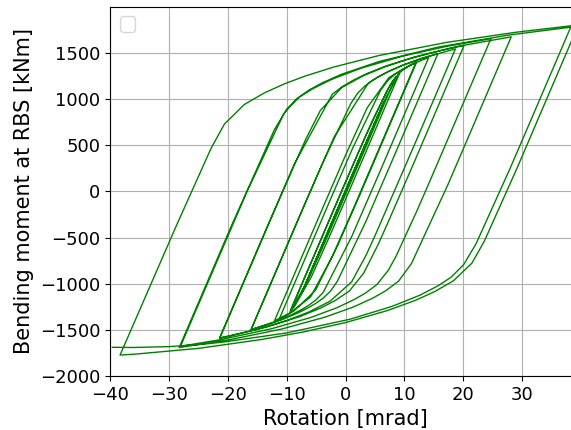


Figure 3.16: Moment-rotation diagram for HEA600 - HEM550 beam-to-column assembly. $r = 0.833$, $g = 0.2b_f$, S355 steel grade

As it can be observed from the diagram, the assembly performed very well. It developed wide and stable hysteresis loops, kept hardening as subsequent load steps were imposed with increasing rotation and reached its maximum strength at the

40mrad cycles, with the value $M_{40} = M_{max} = 1792.89kNm$. In this case, the nominal bending resistance is $M_{pl,Rd} = 1297.77kNm$, which indicates substantial overstrength with a factor of 1.38. Moreover, the fact that the maximum bending moment M_{max} and the bending moment at 40mrad rotation M_{40} are exactly the same implies that there is no strength degradation after the cyclic protocol is applied on the beam, exhibiting great reliability and resilience.

Figure 3.17 shows the Von Mises stresses and the equivalent plastic strain in the RBS at the end of the test. Equivalent plastic strains (PEEQ) are a useful way to visualise the results. From a complex stress-strain state, PEEQ gives a scalar to assess the plastic engagement of the assembly and to quantify such plastic engagement. The equivalent plastic strain is defined as:

$$\bar{\epsilon}^{pl} = \int_0^t \dot{\bar{\epsilon}}^{pl} dt \quad (3.11)$$

and the definition of $\dot{\bar{\epsilon}}^{pl}$ depends on the material model. For our case of Von Mises plasticity it is calculated as:

$$\dot{\bar{\epsilon}}^{pl} = \sqrt{\frac{2}{3} \dot{\epsilon}^{pl} : \dot{\epsilon}^{pl}} \quad (3.12)$$

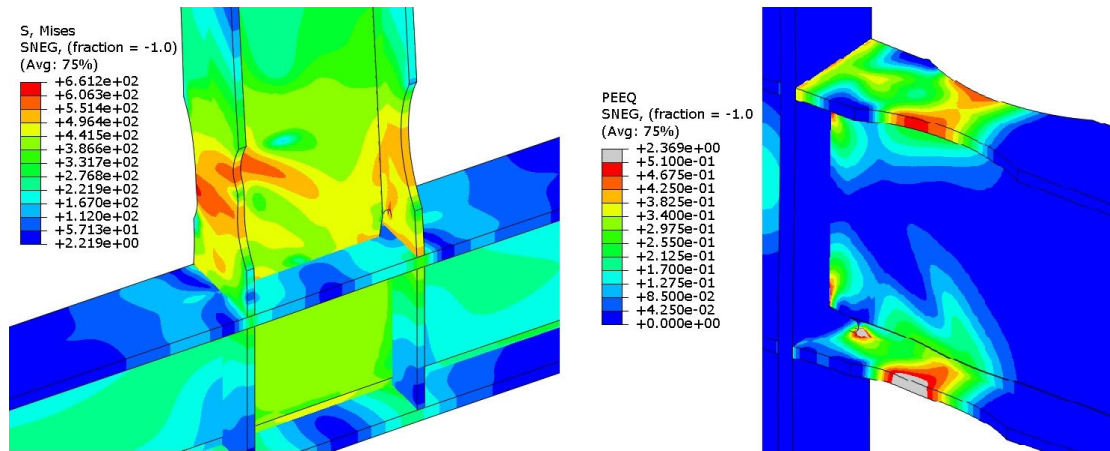


Figure 3.17: Von Mises contours (in N/mm^2 , left) and PEEQ contours (right) for HEA600 - HEM550 beam-to-column assembly. $r = 0.833$, $g = 0.2b_f$, S355 steel grade

As it can be observed, substantial overstrength has been achieved due to the cyclic hardening of the material. The stresses are highest in the beam flange which is in compression at the end of the simulation, where some flange local buckling starts

to develop. Also, high stresses are present on the web, where local buckling can also be detected. Figure 3.18 (right) shows the lateral displacements of the web. Also, the local buckling of the beam flange can be clearly appreciated. On the left, figure 3.18 shows transverse displacements for the whole beam.

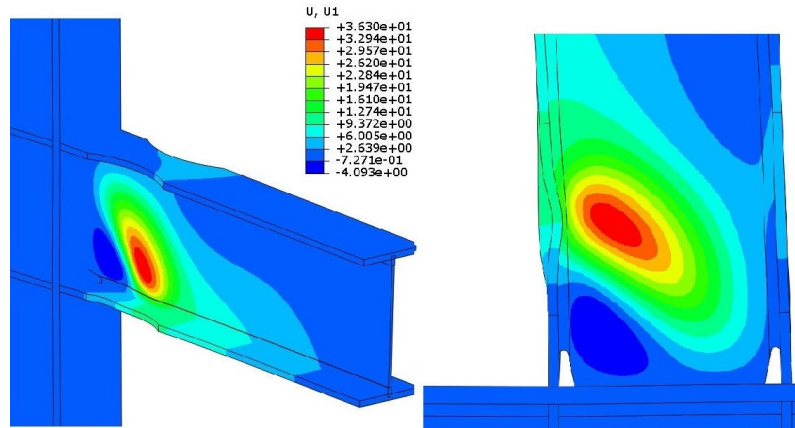


Figure 3.18: Lateral displacement contours (in mm) for HEA600 - HEM550 beam-to-column assembly (left). Close-up view of the RBS (right). $r = 0.833$, $g = 0.2b_f$, S355 steel grade

And it can be appreciated in figure 3.18 that although some substantial local buckling has occurred in the compressed flange and nearby area of the web (with an out-of-plane maximum displacement of about 36.3mm) the beam is not undergoing lateral-torsional buckling in its whole span because of the weakened section.

As it should be expected, the longitudinal stresses are the greatest in the RBS area and at the beam-to-column connection, where the welded area is. The longitudinal stresses σ_x are plotted in figure 3.19.

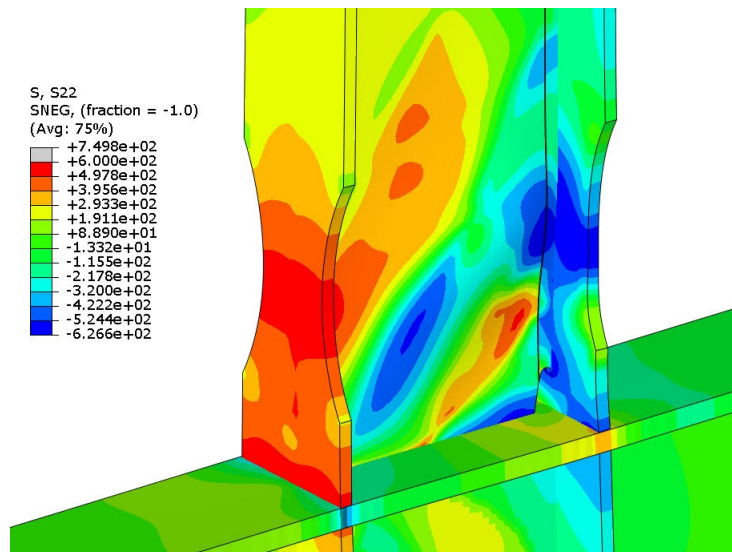


Figure 3.19: Longitudinal stress contours (in N/mm^2) for HEA600 - HEM550 beam-to-column assembly. $r = 0.833$, $g = 0.2b_f$, S355 steel grade

And in figure 3.20 a close-up view on the weld stresses can be observed. The beam flange shown is the flange in tension at the end of the simulation.

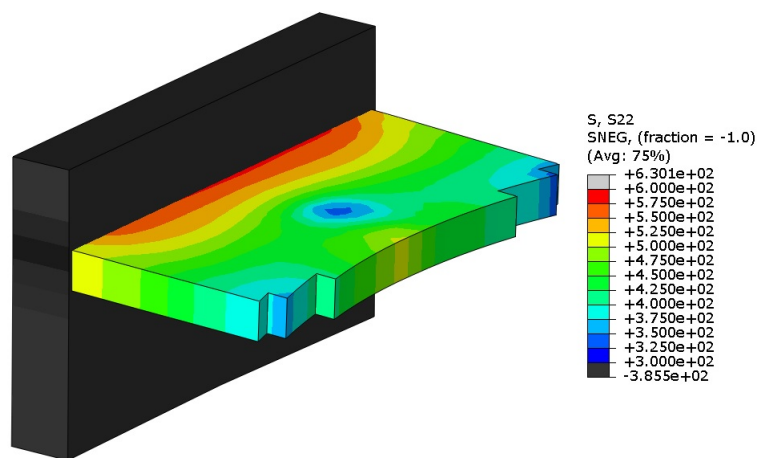


Figure 3.20: Longitudinal stress contours in the weld (in N/mm^2) for HEA600 - HEM550 beam-to-column assembly. $r = 0.833$, $g = 0.2b_f$, S355 steel grade

It can be observed that the stresses are the largest near the column flange, which is to be expected, with an almost uniform distribution.

3.4.2 Detailed results for IPE750 beam, $r = 1.6$, $g = 0.3b_f$, S235

This case exposed here corresponds to an IPE750 - HEM700 assembly. The column web panel is reinforced with an r ratio of 1.6. The cutout at each side is $g = 0.3b_f$ and the steel grade is S235. In this case, the moment-rotation diagram looks quite different from the previous case, as it can be observed in figure 3.21:

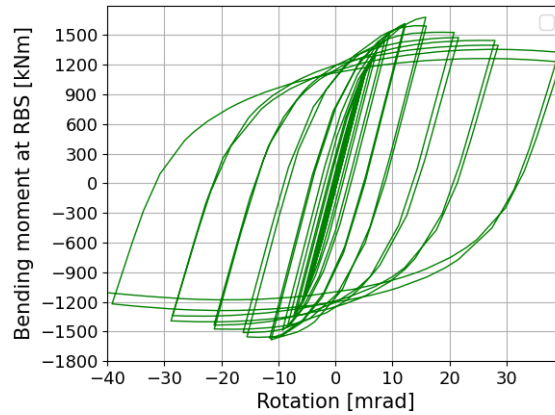


Figure 3.21: Moment-rotation diagram for IPE750 - HEM700 beam-to-column assembly. $r = 1.6$, $g = 0.3b_f$, S235 steel grade

There appears to be a substantial loss of strength due to the imposed cycles on the beam. Indeed, the maximum bending moment in this simulation is $M_{max} = 1680.64kNm$ at a rotation of about 16mrad. The degraded bending moment at the imposed rotation of 40mrad is $M_{40} = 1327.28kNm$, so there has been a substantial amount of strength loss between the maximum and the degraded strength at 40mrad, of about 21%. However, the nominal plastic moment of this specimen is $M_{pl,Rd} = 971.21kNm$, so the bending resistance after the imposed 40mrad cycle is well above the design strength and according to these data, the behaviour is nevertheless acceptable.

It can be observed in figure 3.22 that the stresses are highest in the beam flanges, especially in the flange in compression. Again, high stresses are also present on the web. There is a very substantial local buckling of the beam flanges, which have undergone some local bending and kinking. The scale has been modified in order to promote more distinguishable contours for a clearer interpretation.

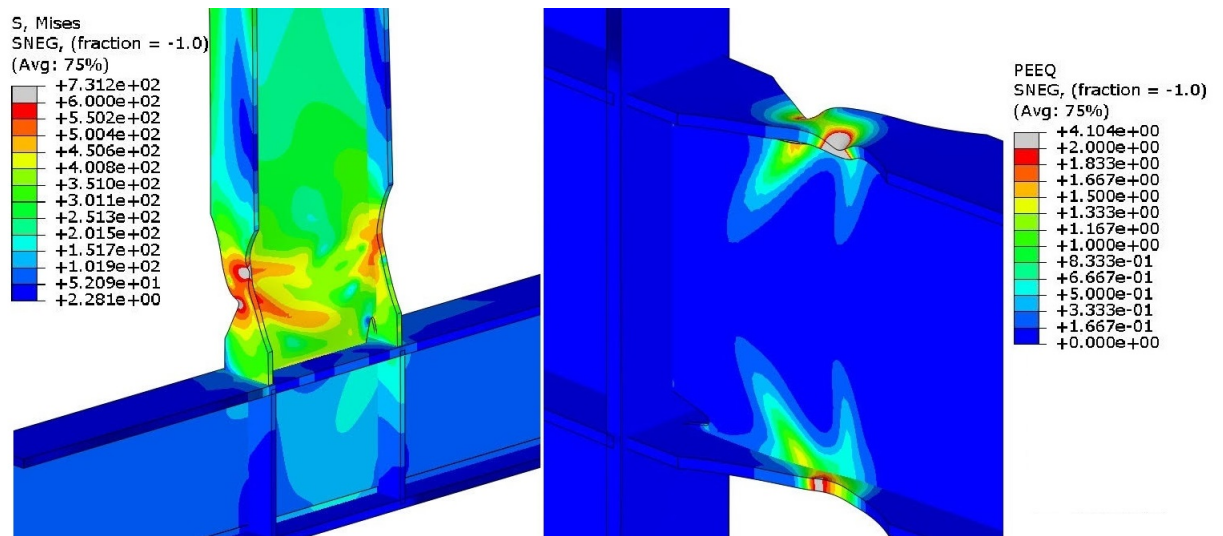


Figure 3.22: Von Mises contours (in N/mm^2 , left) and PEEQ contours (right) for IPE750 - HEM700 beam-to-column assembly. $r = 1.6$, $g = 0.3b_f$, S235 steel grade

The web also experiences some local buckling with a maximum out-of-plane displacement of 90mm (see figure 3.23). Figure 3.23 gives an overview of the lateral displacements of the whole beam and a detailed look on the RBS for the web out-of-plane displacements.

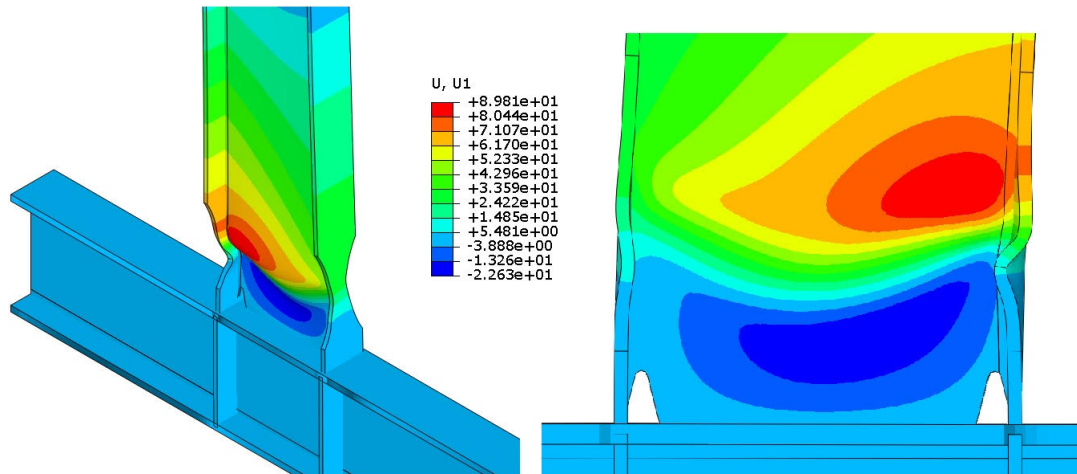


Figure 3.23: Lateral displacement contours (in mm) for IPE750 - HEM700 beam-to-column assembly (left). Close-up view of the RBS (right). $r = 1.6$, $g = 0.3b_f$, S235 steel grade

And in this case, the greater reduction in flange area compared to the previous case(only 40% of the flange area is remaining) causes the stresses in the welded

flange-to-flange connection to be reduced, and the maximum longitudinal stresses can be found in the beam flange at the RBS as shown in figure 3.24.

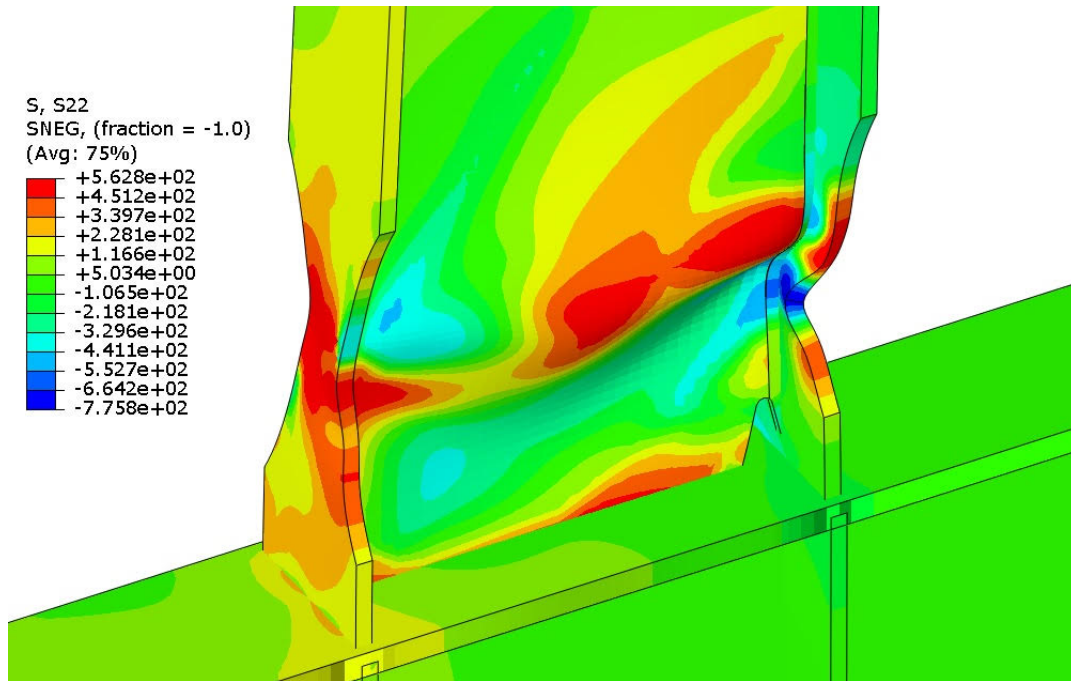


Figure 3.24: Longitudinal stress contours (in N/mm^2) for IPE750 - HEM700 beam-to-column assembly. $r = 1.6$, $g = 0.3b_f$, S235 steel grade

And in figure 3.25 a close-up view on the weld stresses can be observed. The beam flange shown is the flange in tension at the end of the simulation.

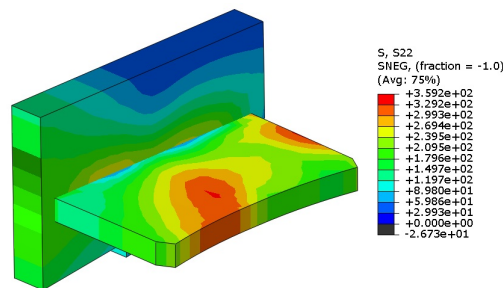


Figure 3.25: Longitudinal stress contours in the weld (in N/mm^2) for IPE750 - HEM700 beam-to-column assembly. $r = 1.6$, $g = 0.3b_f$, S235 steel grade

In this case, the stresses found near the weld do not follow a uniform distribution, and the contours appear to be distorted due to the local buckling in the RBS. Still, substantial tensile stresses are found in this area.

3.4.3 Detailed results for built-up girder, $r = 1.312$, $g = 0.25b_f$, S355

This case exposed in this subsection corresponds to the built-up girder. It is by far the most slender member in this study, with class 3 flanges and class 4 web for S355 steel grade (for the case of S235 steel grade the beam has class 2 flanges and class 3 web). It was paired with an HE100x393 column cross-section. In this particular case the column web panel is unreinforced, but the r ratio is 1.312, with substantial overstrength over the beam. The trimmed flange width in this case is $g = 0.25b_f$, with an effective flange width at the RBS exactly half of the width of the intact section. The steel grade is S355.

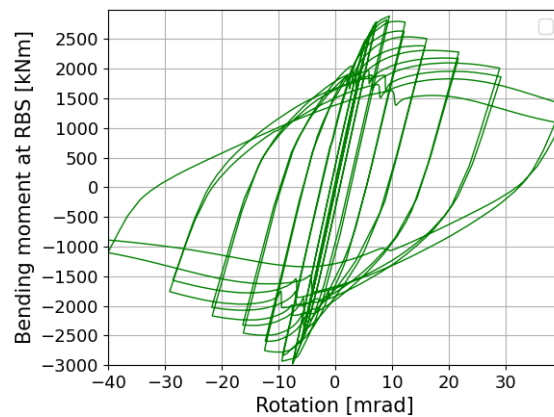


Figure 3.26: Moment-rotation diagram for built-up girder beam-to-column assembly. $r = 1.312$, $g = 0.25b_f$, S355 steel grade

It is very clear that in this case, strength degradation is very large. The hysteresis cycles developed are not stable and wide as the case of the HEA600 beam. It is very clear that all the peaks at every load step achieve lower bending strength as the amplitude is increased in subsequent steps. Indeed, the maximum bending moment developed in this simulation is $M_{max} = 2941.51kNm$ and the bending moment at 40mrad is $M_{40} = 1103.96kNm$. In this case, the nominal strength is $M_{eff,Rd} = 2295.62kNm$, so the degradation in this case has essentially halved its resistance at 40mrad. It is even possible to see some pinching in some of the cycles. Figure 3.27 highlights in red the cycles with pinching. Some initial cycles have been removed for a better interpretation of the chart.

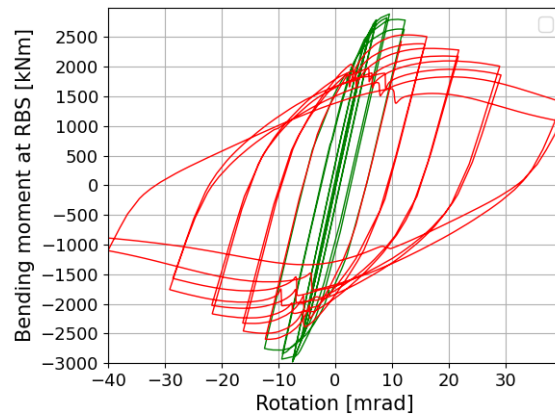


Figure 3.27: Moment-rotation diagram for built-up girder beam-to-column assembly. In red, cycles with pinching. $r = 1.312$, $g = 0.25b_f$, S355 steel grade

Figure 3.28 shows the Von Mises stresses and the equivalent plastic strains at the end of the simulation for this specimen:

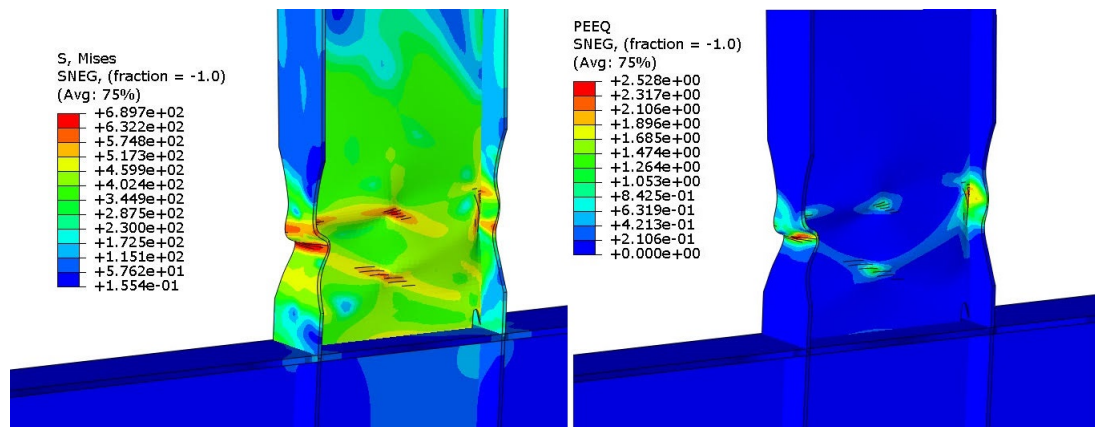


Figure 3.28: Von Mises contours (in N/mm^2 , left) and PEEQ contours (right) for built-up girder beam-to-column assembly. $r = 1.312$, $g = 0.25b_f$, S355 steel grade

It is very obvious that the flanges and web are experiencing a lot of kinking and local buckling rather than forming a plastic hinge mechanism, which is to be expected since this specimen has class 3 flanges and class 4 web. Lateral displacements can be observed in figure 3.29.

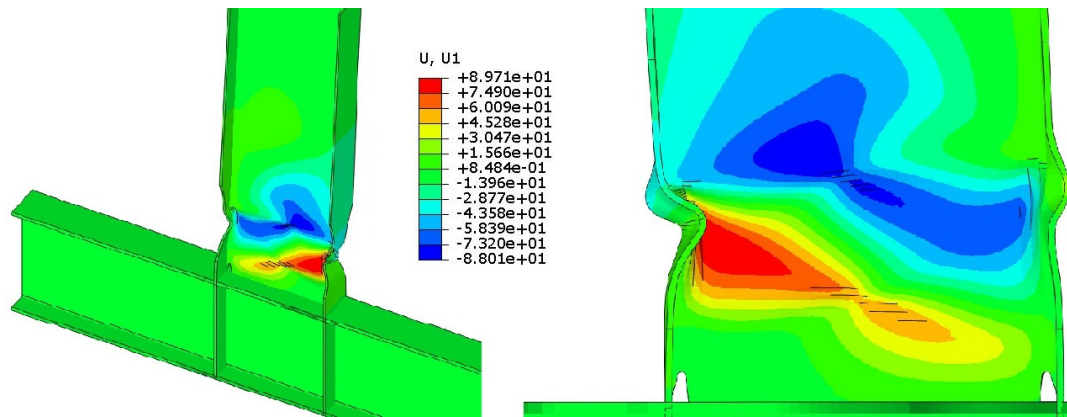


Figure 3.29: Lateral displacement contours (in mm) for built-up girder beam-to-column assembly (left). Close-up view of the RBS (right). $r = 1.312$, $g = 0.25b_f$, S355 steel grade

The out-of-plane displacement of the web is very obvious, and the compressed flange also moves laterally a substantial amount.

As for longitudinal stresses developed, since the beam is very slender and clearly the weak part of the assembly, the connection is undergoing moderate stresses, far from being the maximum stresses in the model.

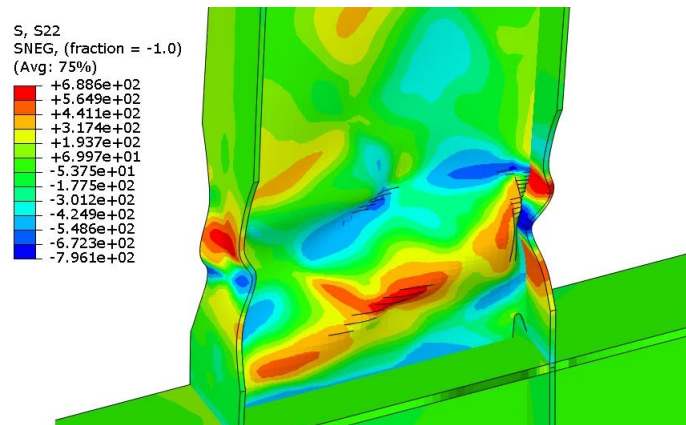


Figure 3.30: Longitudinal stress contours (in N/mm^2) for built-up girder beam-to-column assembly. $r = 1.312$, $g = 0.25b_f$, S355 steel grade

Figure 3.31 shows a close-up view on the weld stresses. The beam flange shown is the flange expected to be in tension at the end of the simulation.

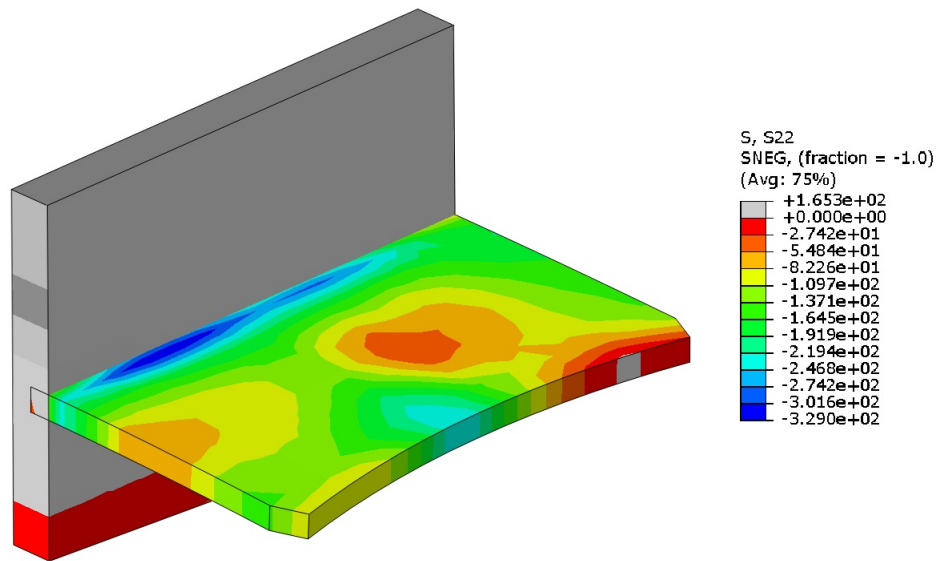


Figure 3.31: Longitudinal stress contours in the weld (in N/mm^2) for the built-up girder beam-to-column assembly. $r = 1.312$, $g = 0.25b_f$, S355 steel grade

Due to the severe damage in the RBS, the flange portion between the RBS and the column flange does not behave as expected and the stresses present are all compressive.

It is clear that this type of section is not the best suited in order to resist seismic demands in a structure and clearly does not qualify to belong in the Ductility Class High (DCH) category in EN1998-1 [18]. However, there might still be some value to sections like this for their application in a Ductility Class Medium (DCM) design or for the upgrade of existing buildings. More elaboration on this topic can be found in the next subsection 3.4.5.

3.4.4 Detailed results for Jumbo section, $r = 1.6$, $g = 0.25b_f$, S355

This case exposed in this subsection corresponds to an assembly with a Jumbo beam. It is a very robust specimen with very compact flanges and web. It was paired with a W44x593 column cross-section ($d_b=1092\text{mm}$, $b_f=424\text{mm}$, $t_f=82\text{mm}$). In this particular case the column web panel is reinforced, with an r ratio of 1.6, with large overstrength over the beam. The trimmed flange width in this case is $g = 0.25b_f$, with an effective flange width at the RBS exactly half of the width of the intact section. The steel grade is S355.

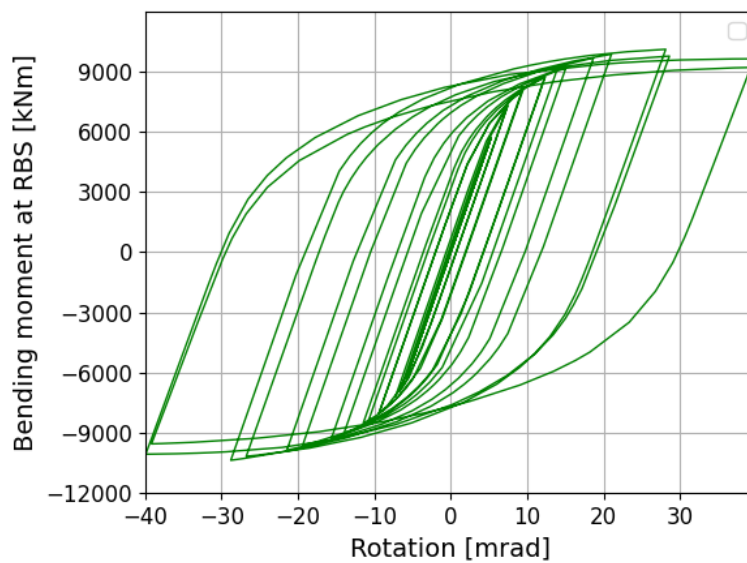


Figure 3.32: Moment-rotation diagram for Jumbo section beam-to-column assembly. $r = 1.6$, $g = 0.25b_f$, S355 steel grade

It can be observed that the specimen exhibited small strength degradation and the hysteresis loops were stable. It is clear that all the peaks at every load step achieve higher strength as the amplitude is increased in subsequent steps up to a rotation of 30mrad, where the maximum bending moment developed in this simulation is found with a value $M_{max} = 10364.45kNm$. In the following steps at 40mrad rotation, a small loss of strength is found. Nevertheless, the strength of the specimen is substantially above the design value $M_{pl,Rd} = 7380.16kNm$, so the maximum strength achieved by this assembly is $M_{max} = 1.404M_{pl,Rd}$.

Figure 3.33 shows the Von Mises stresses and the equivalent plastic strains at the end of the simulation for this specimen:

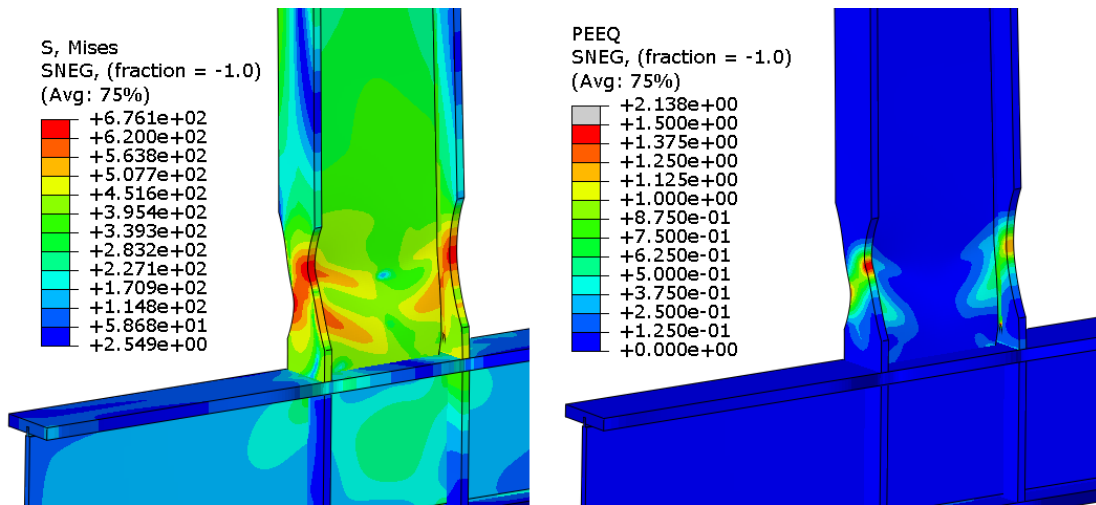


Figure 3.33: Von Mises contours (in N/mm^2 , left) and PEEQ contours (right) for Jumbo section beam-to-column assembly. $r = 1.6$, $g = 0.25b_f$, S355 steel grade

After the loading it can be seen that the flanges and web are experiencing a certain degree of local buckling. Substantial plastic damage can be observed in the flanges as well as part of the web, reflecting the formation of a plastic hinge. However, the damage is not extreme as in the case of the plated girder discussed previously. Lateral displacements can be observed in figure 3.34.

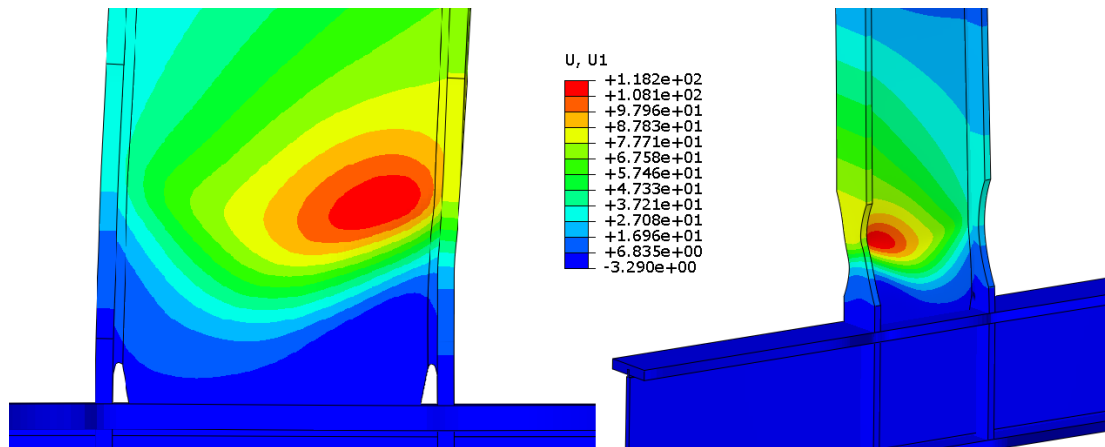


Figure 3.34: Lateral displacement contours (in mm) for Jumbo section beam-to-column assembly. Close-up view of the RBS (right). $r = 1.6$, $g = 0.25b_f$, S355 steel grade.

As for longitudinal stresses developed, they can be seen in figure 3.35. The largest strains are concentrated in the RBS and the connection.

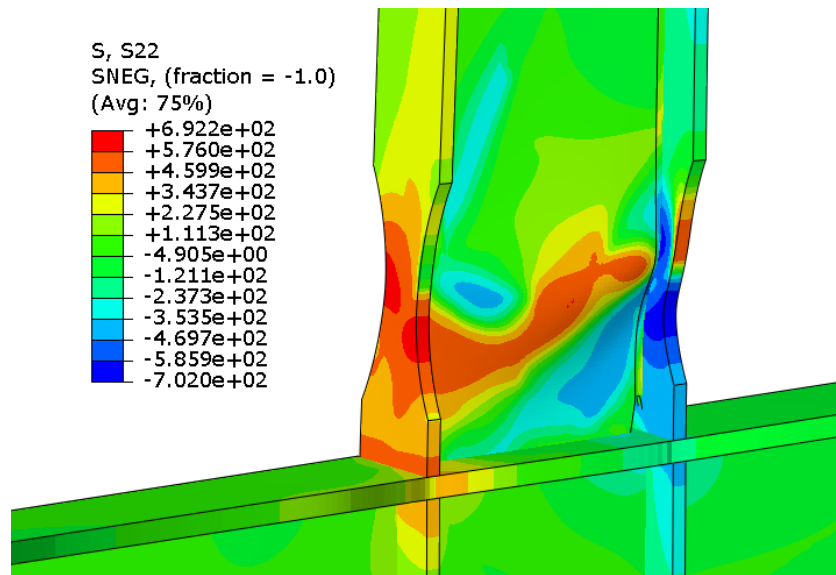


Figure 3.35: Longitudinal stress contours (in N/mm^2) for Jumbo section beam-to-column assembly. $r = 1.6$, $g = 0.25b_f$, S355 steel grade

Figure 3.31 shows a close-up view on the weld stresses. The beam flange shown is the flange in tension at the end of the simulation.

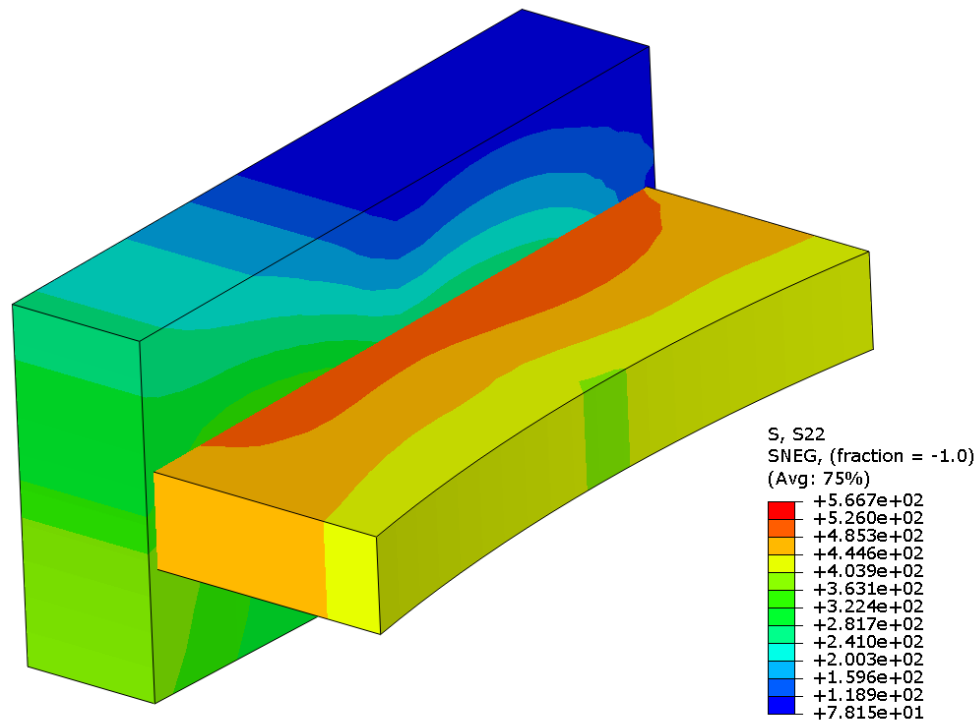


Figure 3.36: Longitudinal stress contours in the weld (in N/mm^2) for Jumbo section beam-to-column assembly. $r = 1.6$, $g = 0.25b_f$, S355 steel grade

The weld stresses results appear to be quite even across the flange width. The average longitudinal stress across the flange width is $\sigma_x=549.02\text{MPa}$.

3.4.5 Summary of the results for all the assemblies

In this subsection, an overview of the results obtained for all the simulated assemblies is presented. From all the Abaqus models, moment-rotation curves have been derived, as well as longitudinal stresses at the welded flange-to-flange connection and dissipated plastic work. In the following charts and tables the results can be found, which have been obtained by means of the analysis of each case, in an analogous way to what has been done in the detailed cases exposed in the prior subsections.

Figure 3.37 shows the loss of flexural strength between the maximum moment M_{max} and the degraded moment at 40mrad M_{40} against the web panel zone strength ratio r for the assemblies with S355 steel grade. And in figure 3.38, the

same ratios can be found for S235 steel grade assemblies. The results are sorted by the amount of trimmed flange width g in each case.

Except for a few cases, it can be observed that most specimens retain a large resistance at 40mrad with most points falling over $0.8M_{max}$, exhibiting small strength loss. Figures 3.39 and 3.40 show the ratios between the moment obtained in the simulations at 40mrad M_{40} over the design capacity $M_{pl,Rd}$ (for the case of the built-up girder $M_{el,Rd}$ for S235 steel grade and $M_{eff,Rd}$ for S355 steel grade) against the web panel zone strength ratio r .

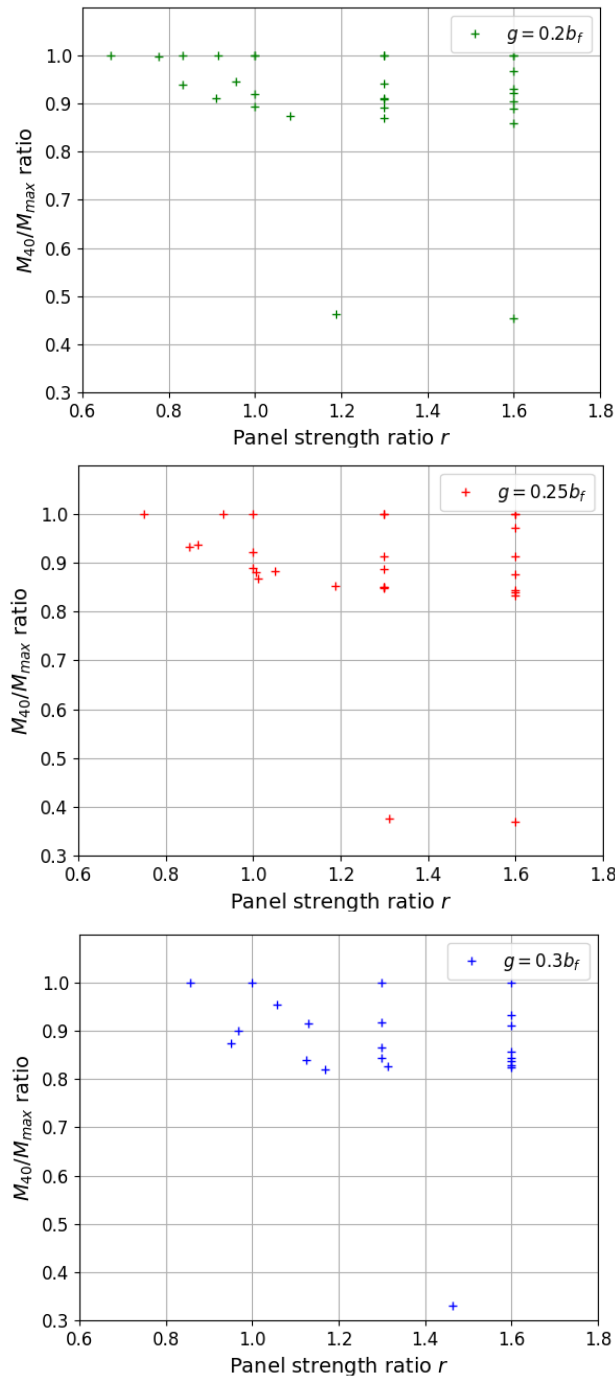


Figure 3.37: M_{40}/M_{max} ratios vs web panel strength r . $g = 0.2b_f$ in green, $g = 0.25b_f$ in red and $g = 0.3b_f$ in blue. S355 steel grade

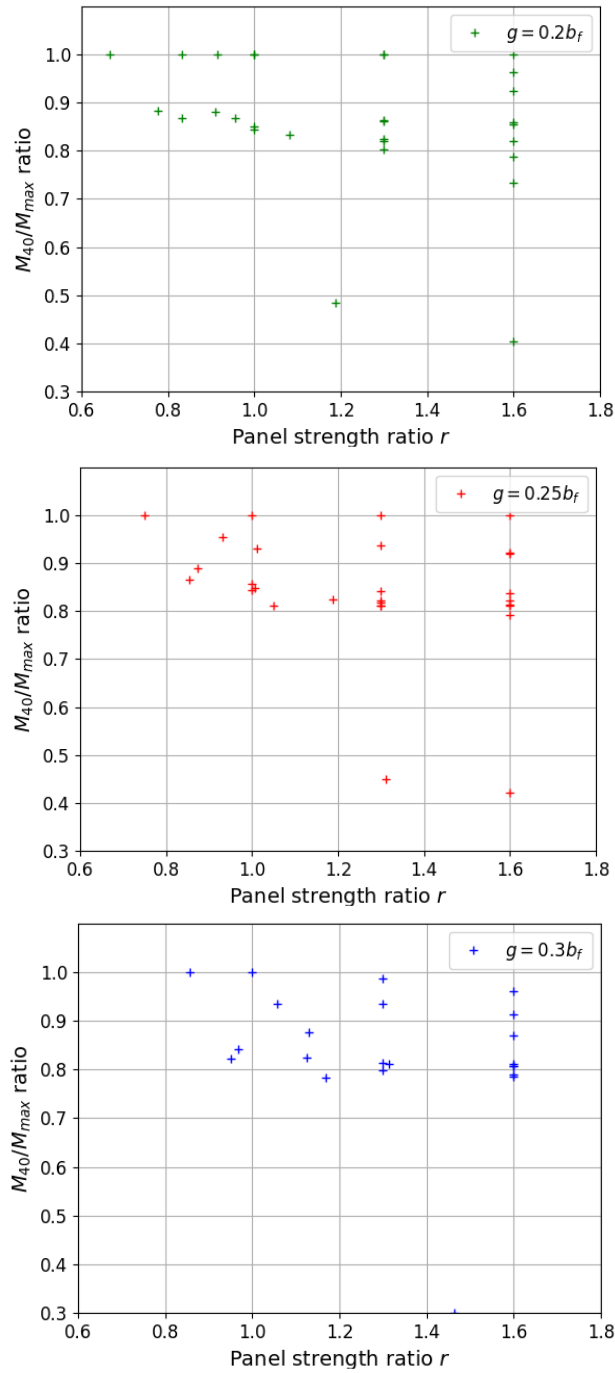


Figure 3.38: M_{40}/M_{max} ratios vs web panel strength r . $g = 0.2b_f$ in green, $g = 0.25b_f$ in red and $g = 0.3b_f$ in blue. S235 steel grade

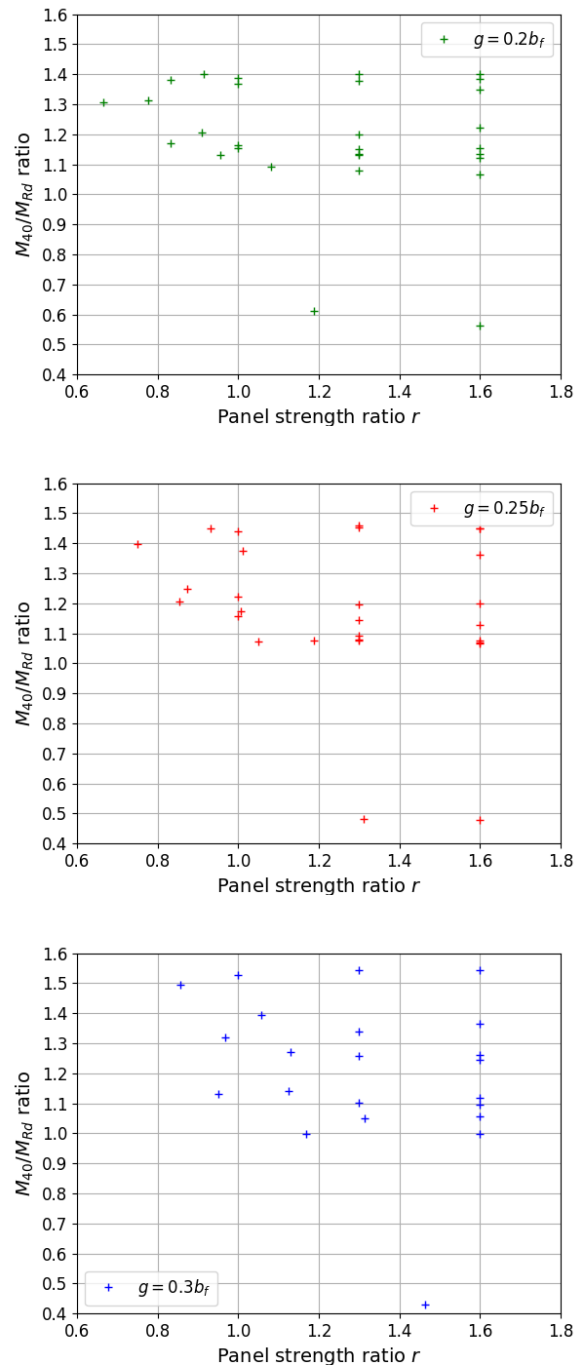


Figure 3.39: M_{40}/M_{Rd} ratios vs web panel strength r . $g = 0.2b_f$ in green, $g = 0.25b_f$ in red and $g = 0.3b_f$ in blue. S355 steel grade

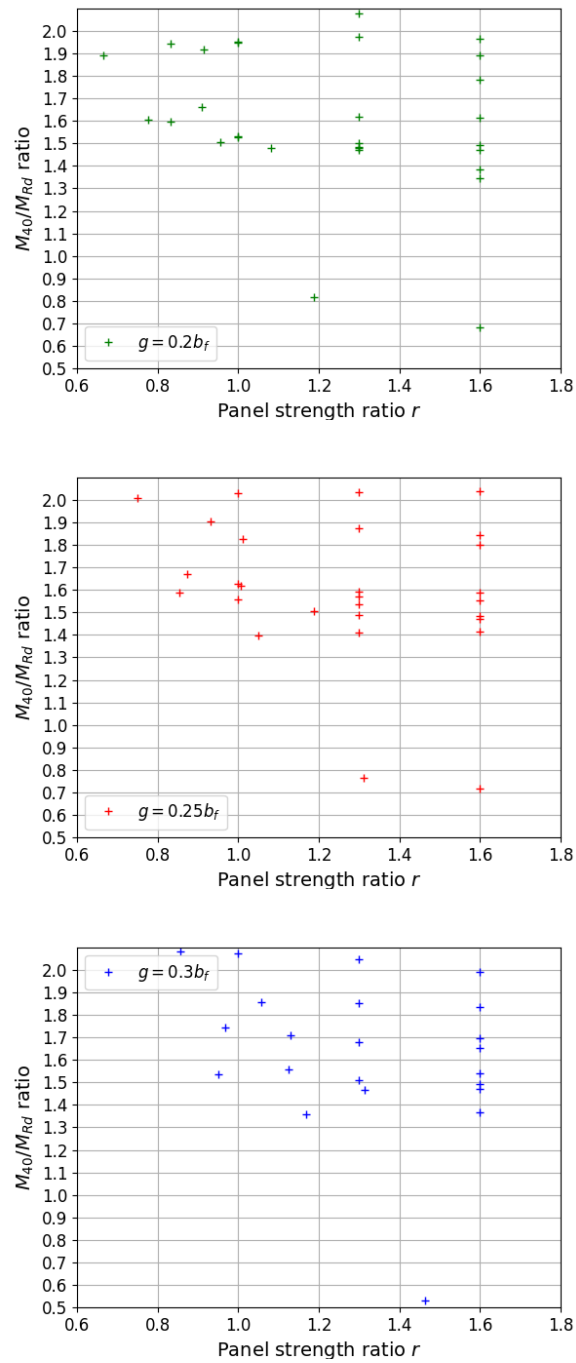


Figure 3.40: M_{40}/M_{Rd} ratios vs web panel strength r . $g = 0.2b_f$ in green, $g = 0.25b_f$ in red and $g = 0.3b_f$ in blue. S235 steel grade

As it can be observed, there are a few points falling very low in the charts in figures 3.37 through 3.40. These points at the bottom of the figures correspond to the built-up girder, which exhibited large strength degradation. The next figures 3.41 and 3.42 show the results obtained for the M_{40}/M_{Rd} ratios plotted against web slenderness λ_w . This slenderness has been computed as

$$\lambda_w = \frac{\frac{\bar{h}_w}{t_w}}{28.4\varepsilon\sqrt{k_\sigma}} \quad (3.13)$$

with $k_\sigma = 23.9$, representing equal but opposite strains at both ends ($\psi = -1$). It can be observed that the data points for M_{40}/M_{Rd} against λ_w seem to be distributed along a trend line. The web slenderness may have an influence on the response of the RBS.

Following figures 3.41 and 3.42, figures 3.43 and 3.44 show the M_{40}/M_{Rd} ratios plotted against RBS flange slenderness $\lambda_{f,RBS}$. It can be observed in figures 3.43 and 3.44 the data present more scatter and there seems to be no clear trend for the strength degradation ratio M_{40}/M_{Rd} .

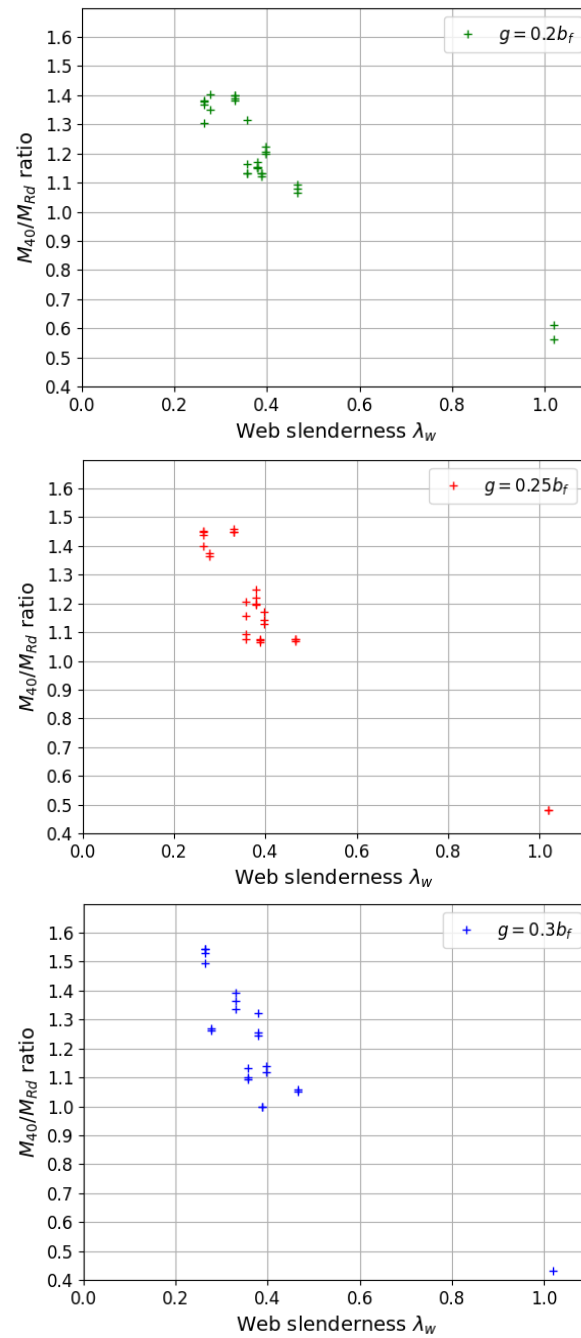


Figure 3.41: M_{40}/M_{Rd} ratios vs web slenderness λ_w . $g = 0.2b_f$ in green, $g = 0.25b_f$ in red and $g = 0.3b_f$ in blue. S355 steel grade

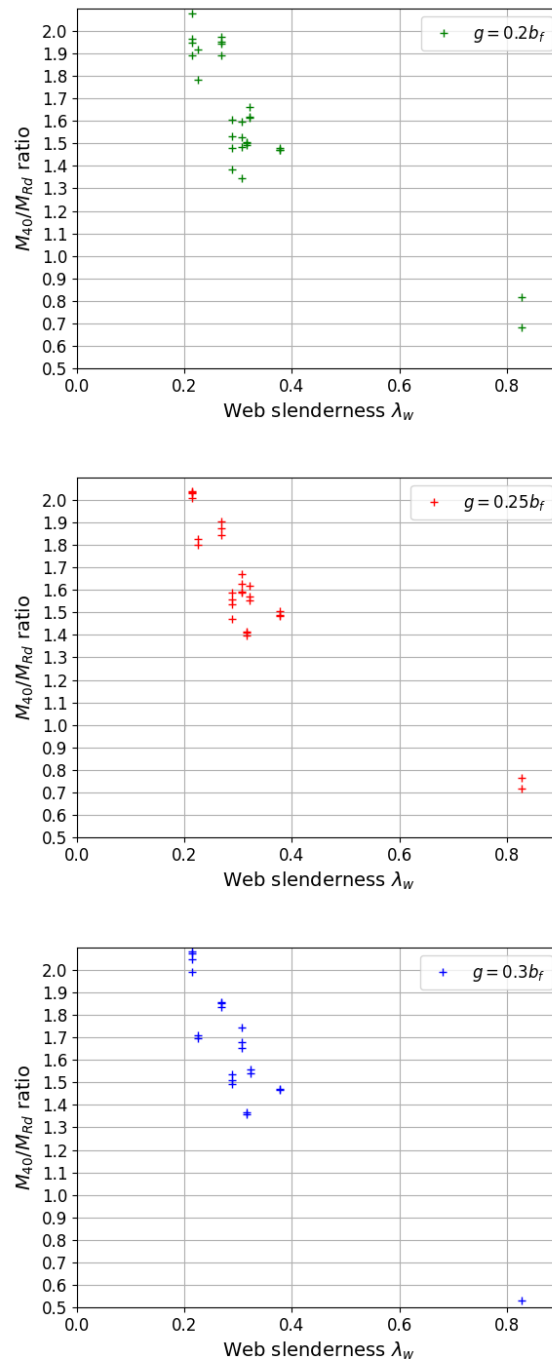


Figure 3.42: M_{40}/M_{Rd} ratios vs web slenderness λ_w . $g = 0.2b_f$ in green, $g = 0.25b_f$ in red and $g = 0.3b_f$ in blue. S235 steel grade

And analogously, figures 3.43 and 3.44 show the results obtained for the M_{40}/M_{Rd} ratios against the RBS flange slenderness $\lambda_{f,RBS}$. The slenderness has been calculated according to equation 3.13 with $k_\sigma = 0.43$ ($\psi = 1$).

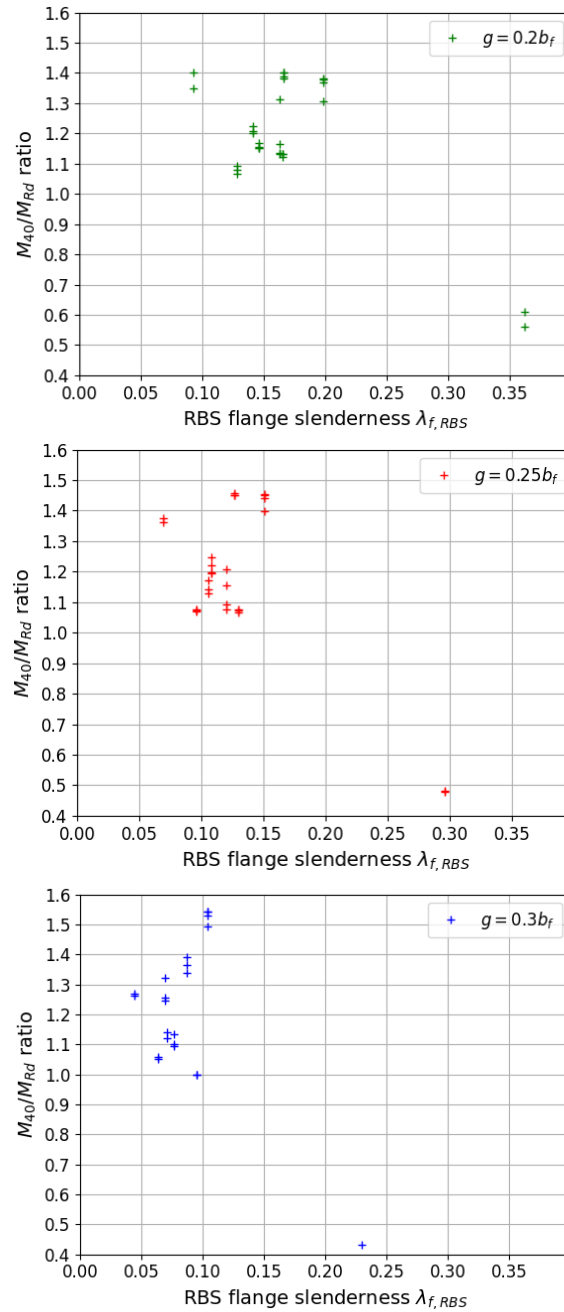


Figure 3.43: M_{40}/M_{Rd} ratios vs RBS flange slenderness $\lambda_{f,RBS}$. $g = 0.2b_f$ in green, $g = 0.25b_f$ in red and $g = 0.3b_f$ in blue. S355 steel grade

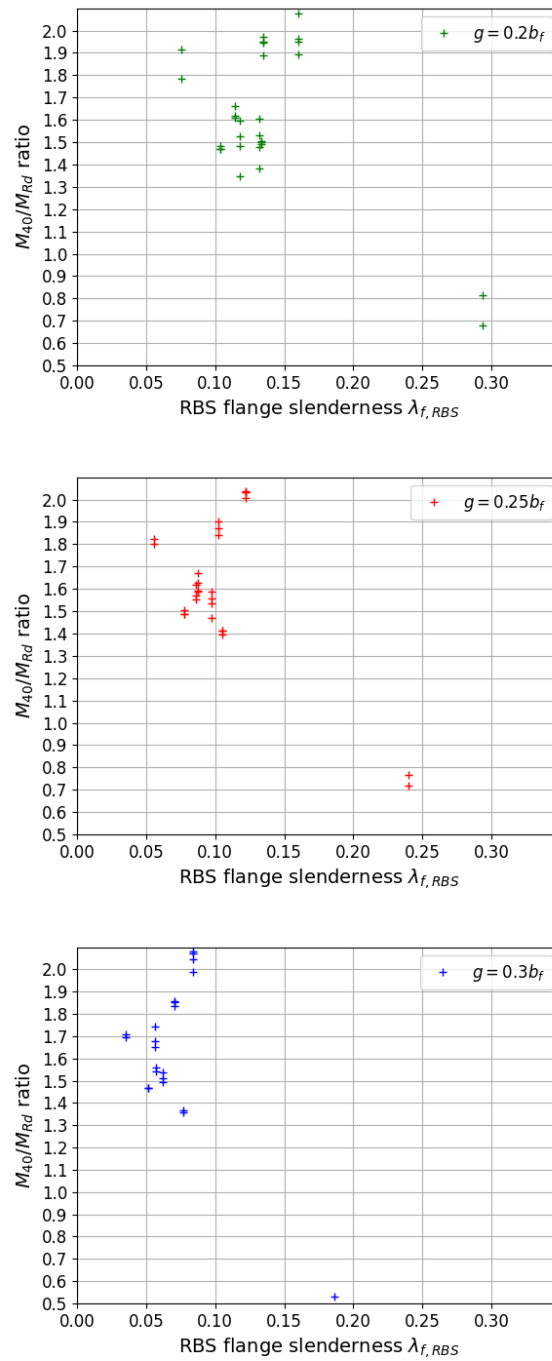


Figure 3.44: M_{40}/M_{Rd} ratios vs RBS flange slenderness $\lambda_{f,RBS}$. $g = 0.2b_f$ in green, $g = 0.25b_f$ in red and $g = 0.3b_f$ in blue. S235 steel grade

The next figures 3.45 and 3.46 show the maximum average longitudinal stress σ_x in the welds (in N/mm^2), at the connection during the simulated tests.

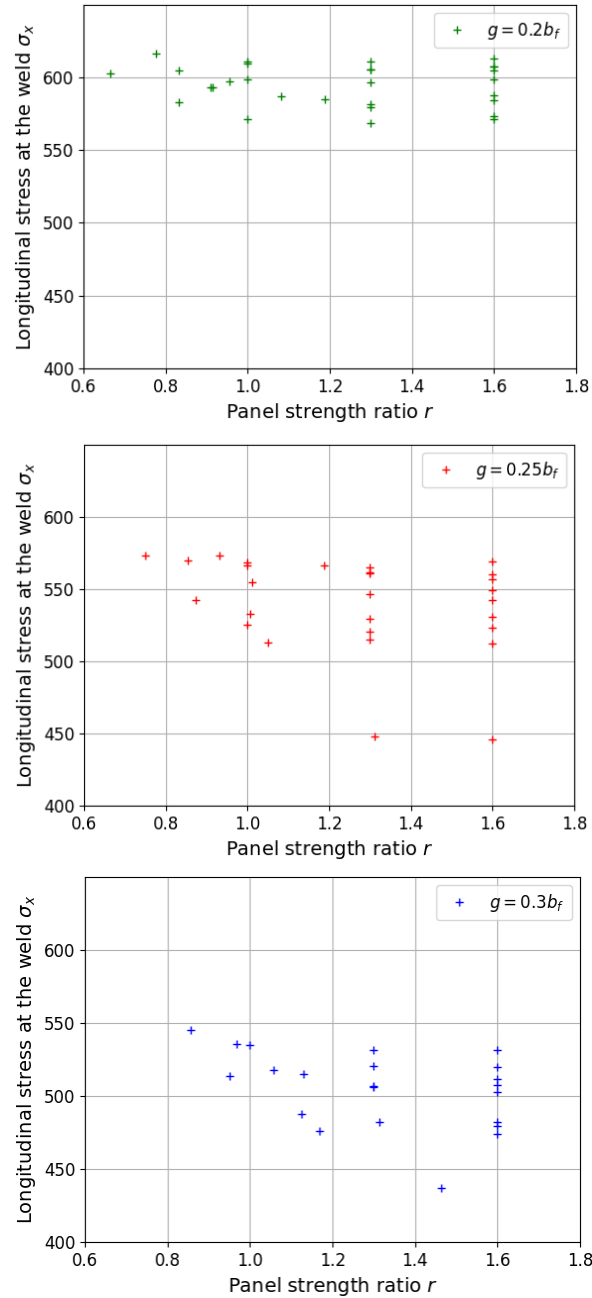


Figure 3.45: Maximum average longitudinal stress σ_x in the welds (in N/mm^2) against the panel strength ratio r . $g = 0.2b_f$ in green, $g = 0.25b_f$ in red and $g = 0.3b_f$ in blue. S355 steel grade

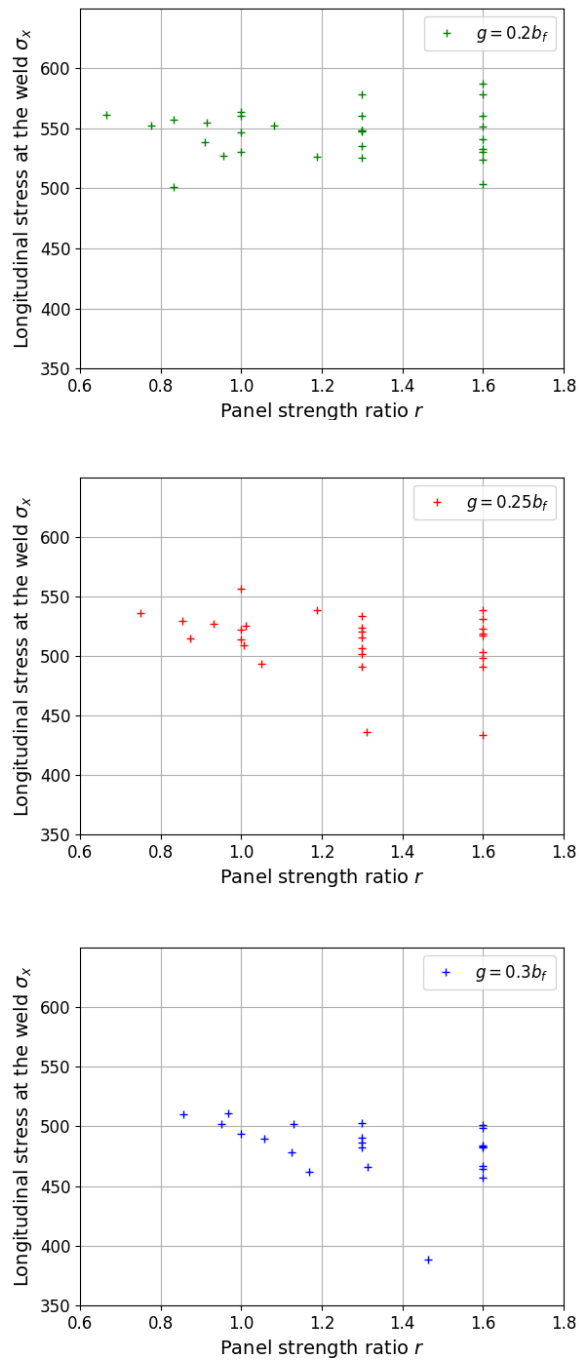


Figure 3.46: Maximum average longitudinal stress σ_x in the welds (in N/mm^2) against the panel strength ratio r . $g = 0.2b_f$ in green, $g = 0.25b_f$ in red and $g = 0.3b_f$ in blue. S235 steel grade

It is obvious that the larger the trimmed portion of the flanges, the lower the stresses in the welded area due to a reduction in maximum bearing capacity of the beam.

The most relevant results obtained in the simulations are shown in tables 3.17 through 3.20. The tables are organised in such a way so that the European hot-rolled profiles are in one table, and the built-up girder and the Jumbo section in another. One set of tables has been included for S355 steel assemblies and another one for the S235 assemblies. The main parameters included in the tables are the maximum bending moment achieved at the RBS (M_{max}), the overstrength ratio M_{max}/M_{Rd} , the 40mrad to nominal bending moment ratio (M_{40}/M_{Rd}), the maximum longitudinal stress in the weld σ_x averaged along the whole fillet and the dissipated plastic work w^{pl} . These parameters allow for an easy comparison between specimens in terms of absolute strength, relative overstrength with respect to the design strength values M_{Rd} , degradation of flexural strength at 40mrad rotation, weld stress levels and energy dissipation due to plastic strain development.

Table 3.17: Summary of the results obtained for hot-rolled European profiles assemblies in S355 steel

Profile	g	r	M_{max} (kNm)	M_{max}/M_{Rd}	M_{40}/M_{Rd}	σ_x (MPa)	w^{pl} (kJ)
HEA450	$0.2b_f$	0.666	1001.42	1.306	1.306	602.85	443.91
		1	1048.75	1.367	1.367	609.65	528.76
		1.3	1056.51	1.378	1.378	610.78	531.78
		1.6	1060.90	1.383	1.383	612.73	552.27
	$0.25b_f$	0.75	941.03	1.398	1.398	572.91	439.44
		1	968.98	1.439	1.439	568.55	481.35
		1.3	978.65	1.454	1.454	561.21	513.11
	$0.3b_f$	1.6	975.64	1.449	1.449	556.58	513.86
		0.857	865.94	1.494	1.494	545.17	422.73
		1	885.72	1.529	1.529	534.93	482.15
		1.3	894.22	1.543	1.543	531.39	506.78
	IPE450	$0.2b_f$	1.6	894.73	1.544	1.544	531.52
0.776			569.52	1.316	1.314	616.54	300.87
1			547.60	1.266	1.164	610.79	317.79
1.3			538.11	1.244	1.133	596.48	324.52
$0.25b_f$		1.6	542.56	1.254	1.134	607.32	318.94
		0.854	504.54	1.294	1.207	569.57	291.56
		1	506.91	1.300	1.156	566.41	292.63
		1.3	500.72	1.285	1.092	546.44	298.18
$0.3b_f$		1.6	503.37	1.291	1.077	542.00	299.02
		0.95	449.09	1.295	1.132	513.83	262.02
		1.3	452.83	1.305	1.102	505.87	263.34
HEA600		$0.2b_f$	1.6	453.77	1.308	1.095	502.44
	0.833		1792.88	1.382	1.382	604.89	967.93
	1		1800.87	1.388	1.388	598.27	1004.93
	1.3		1816.99	1.400	1.400	605.27	1031.73
	$0.25b_f$	1.6	1818.26	1.401	1.401	604.46	1026.86
		0.932	1663.23	1.450	1.450	573.01	928.64
		1.3	1673.78	1.459	1.459	561.03	969.18
		1.6	1663.94	1.450	1.450	560.29	955.38
	$0.3b_f$	1.058	1455.14	1.460	1.393	517.72	866.06
		1.3	1453.18	1.458	1.338	506.67	897.09
		1.6	1457.65	1.462	1.364	507.09	897.83

Table 3.17: Summary of the results obtained for hot-rolled European profiles assemblies in S355 steel. Continued from previous page

Profile	g	r	M_{max} (kNm)	M_{max}/M_{Rd}	M_{40}/M_{Rd}	σ_x (MPa)	w^{pl} (kJ)	
IPE600	0.2 b_f	0.797	1123.64	1.246	1.170	583.15	623.87	
		1	1164.55	1.291	1.155	571.39	638.42	
		1.3	1164.69	1.291	1.152	568.64	664.81	
		1.6	1170.16	1.297	1.153	571.18	668.90	
	0.25 b_f	0.874	1086.79	1.332	1.248	542.18	606.04	
		1	1080.80	1.325	1.221	525.01	616.52	
		1.3	1069.62	1.311	1.196	520.29	618.85	
	0.3 b_f	1.6	1070.02	1.311	1.198	522.77	617.59	
		0.968	1072.18	1.469	1.321	535.17	583.50	
		1.3	1058.44	1.450	1.256	520.16	597.83	
	HEA800	0.2 b_f	1.6	1060.73	1.454	1.245	519.82	616.35
			0.909	2883.77	1.323	1.207	593.40	1676.27
1.3			2880.72	1.322	1.200	579.26	1740.88	
0.25 b_f		1.6	2891.75	1.327	1.223	587.94	1781.69	
		1.006	2597.12	1.330	1.172	532.57	1583.15	
		1.3	2621.55	1.343	1.143	529.23	1625.20	
0.3 b_f		1.6	2627.71	1.346	1.129	530.86	1644.72	
		1.126	2344.99	1.360	1.141	487.38	1405.15	
IPE750		0.2 b_f	1.6	2288.56	1.327	1.120	481.96	1475.45
			0.955	2185.81	1.196	1.131	597.37	1267.66
			1.3	2198.27	1.203	1.133	605.41	1289.37
		0.25 b_f	1.6	2201.45	1.205	1.121	607.29	1326.67
	1.051		2001.04	1.215	1.072	512.72	1181.44	
	1.3		1998.70	1.213	1.078	514.69	1204.40	
	0.3 b_f	1.6	2005.05	1.217	1.066	512.35	1218.27	
		1.168	1786.51	1.218	1.000	476.11	1084.33	
	HEA1000	0.2 b_f	1.6	1774.55	1.210	0.998	473.80	1083.03
			1.082	4104.84	1.250	1.092	587.04	2457.31
			1.3	4081.41	1.243	1.080	581.63	2483.39
		0.25 b_f	1.6	4074.03	1.240	1.066	584.47	2506.61
1.187			3740.25	1.260	1.075	566.20	2307.13	
1.3			3759.67	1.267	1.075	564.61	2483.39	
0.3 b_f		1.6	3758.00	1.266	1.068	569.06	2345.82	
		1.314	3373.62	1.272	1.051	481.81	2076.96	
		1.6	3385.71	1.277	1.057	479.57	2116.94	

Table 3.18: Summary of the results obtained for the built-up girder and Jumbo profile assemblies in S355 steel

Profile	g	r	M_{max} (kNm)	M_{max}/M_{Rd}	M_{40}/M_{Rd}	σ_x (MPa)	w^{pl} (kJ)
Built-up girder	0.2 b_f	1.189	3463.35	1.323	0.611	585.22	1457.18
		1.6	3236.83	1.236	0.562	572.99	1528.05
	0.25 b_f	1.312	2941.51	1.281	0.481	447.76	1552.68
		1.6	2979.33	1.298	0.480	445.77	1565.28
	0.3 b_f	1.463	2576.65	1.306	0.431	436.75	1290.97
	W44x408	0.2 b_f	0.915	11558.26	1.401	1.401	593.40
1.6			11513.42	1.396	1.350	598.36	6833.81
0.25 b_f		1.011	11697.12	1.585	1.375	554.74	6169.10
		1.6	10364.45	1.404	1.363	549.02	6287.32
0.3 b_f		1.13	9046.94	1.389	1.270	514.99	5565.53
		1.6	9016.89	1.384	1.262	511.65	5740.24

Table 3.19: Summary of the results obtained for hot-rolled European profiles assemblies in S235 steel

Profile	g	r	M_{max} (kNm)	M_{max}/M_{Rd}	M_{40}/M_{Rd}	σ_x (MPa)	w^{pl} (kJ)
HEA450	0.2 <i>b_f</i>	0.666	960.66	1.892	1.892	561.40	403.47
		1	989.31	1.949	1.949	560.68	483.25
		1.3	1054.20	2.077	2.077	560.28	483.60
		1.6	997.10	1.964	1.964	560.76	519.77
	0.25 <i>b_f</i>	0.75	893.76	2.006	2.006	535.99	414.34
		1	904.93	2.031	2.031	556.50	453.51
		1.3	906.51	2.034	2.034	523.67	486.04
	0.3 <i>b_f</i>	1.6	908.43	2.039	2.039	523.17	457.91
		0.857	798.04	2.080	2.080	509.90	396.45
		1	795.16	2.073	2.073	493.87	462.54
		1.3	795.79	2.075	2.045	486.61	500.93
	IPE450	0.2 <i>b_f</i>	1.6	794.63	2.072	1.990	483.84
0.776			520.39	1.817	1.603	552.05	276.26
1			515.07	1.798	1.530	546.32	297.38
1.3			517.37	1.806	1.480	548.36	299.81
0.25 <i>b_f</i>		1.6	502.34	1.754	1.382	533.18	296.48
		0.854	474.31	1.838	1.589	529.05	267.55
		1	475.86	1.844	1.556	521.60	269.24
0.3 <i>b_f</i>		1.3	488.67	1.894	1.536	515.42	272.58
		1.6	479.57	1.859	1.470	517.29	281.85
		0.95	428.61	1.866	1.536	502.12	258.86
		1.3	426.98	1.859	1.511	490.38	259.17
HEA600		0.2 <i>b_f</i>	1.6	424.54	1.849	1.493	482.17
	0.833		1669.45	1.943	1.943	557.18	930.52
	1		1675.39	1.950	1.950	563.60	934.14
	1.3		1694.83	1.973	1.973	578.16	996.53
	0.25 <i>b_f</i>	1.6	1687.62	1.964	1.890	578.54	995.33
		0.932	1516.31	1.996	1.904	527.15	909.59
		1.3	1517.06	1.997	1.873	520.12	929.82
	0.3 <i>b_f</i>	1.6	1520.87	2.002	1.841	518.47	952.47
		1.058	1308.71	1.983	1.855	489.32	854.23
		1.3	1309.27	1.984	1.852	482.53	856.48
		1.6	1326.46	2.012	1.835	483.31	885.23

Table 3.19: Summary of the results obtained for hot-rolled European profiles assemblies in S235 steel. Continued from previous page

Profile	g	r	M_{max} (kNm)	M_{max}/M_{Rd}	M_{40}/M_{Rd}	σ_x (MPa)	w^{pl} (kJ)	
IPE600	0.2 b_f	0.797	1100.26	1.842	1.598	501.37	606.61	
		1	1081.28	1.811	1.526	530.73	599.73	
		1.3	1102.07	1.845	1.482	525.39	611.23	
		1.6	1096.60	1.836	1.345	524.03	615.57	
	0.25 b_f	0.874	1013.12	1.876	1.670	514.84	595.56	
		1	1024.54	1.897	1.627	513.95	602.74	
		1.3	1022.71	1.893	1.593	506.36	608.38	
	0.3 b_f	1.6	1024.08	1.896	1.588	502.94	606.88	
		0.968	1000.75	2.072	1.742	510.96	593.83	
		1.3	1015.55	2.102	1.678	502.59	593.83	
	HEA800	0.2 b_f	1.6	1016.05	2.103	1.653	499.052	601.02
			0.909	2721.99	1.887	1.661	538.11	1644.44
1.3			2701.14	1.872	1.617	535.26	1693.27	
0.25 b_f		1.6	2704.56	1.875	1.611	530.00	1699.18	
		1.006	2460.80	1.904	1.617	508.87	1554.88	
		1.3	2481.85	1.921	1.571	501.56	1599.12	
0.3 b_f		1.6	2464.59	1.907	1.552	498.16	1614.67	
		1.126	2157.46	1.890	1.558	478.27	1426.69	
IPE750		0.2 b_f	1.6	2165.49	1.897	1.540	467.10	1471.69
			0.955	2100.76	1.737	1.506	526.80	1270.39
			1.3	2107.07	1.742	1.501	547.67	1267.47
		0.25 b_f	1.6	2111.84	1.746	1.491	541.10	1293.08
	1.051		1875.73	1.720	1.397	493.05	1185.89	
	1.3		1873.02	1.718	1.411	491.05	1192.56	
	0.3 b_f	1.6	1876.59	1.721	1.414	491.05	1199.86	
		1.168	1683.24	1.733	1.358	461.87	1075.99	
	HEA1000	0.2 b_f	1.6	1680.64	1.730	1.367	457.25	1096.69
			1.082	3863.34	1.777	1.481	552.57	3863.34
			1.3	3881.42	1.785	1.470	547.93	2439.73
		0.25 b_f	1.6	3893.27	1.791	1.469	551.26	2472.38
1.187			3582.95	1.824	1.504	537.91	2283.55	
1.3			3598.40	1.831	1.486	533.18	2311.33	
0.3 b_f		1.6	3598.31	1.831	1.485	538.14	2336.09	
		1.314	3174.96	1.809	1.467	465.73	2103.60	
		1.6	3194.29	1.820	1.470	464.74	2134.54	

Table 3.20: Summary of the results obtained for the built-up girder and Jumbo profile assemblies in S235 steel

Profile	g	r	M_{max} (kNm)	M_{max}/M_{Rd}	M_{40}/M_{Rd}	σ_x (MPa)	w^{pl} (kJ)
Built-up girder	$0.2b_f$	1.189	3058.99	1.683	0.815	526.31	1381.89
		1.6	3056.54	1.681	0.681	503.86	1321.29
	$0.25b_f$	1.312	2727.11	1.705	0.765	435.61	1545.89
		1.6	2725.08	1.704	0.718	433.35	1550.01
	$0.3b_f$	1.463	2436.55	1.764	0.530	388.69	1287.98
	W44x408	$0.2b_f$	0.915	10463.69	1.917	1.917	555.10
1.6			10529.78	1.929	1.782	587.39	6835.36
$0.25b_f$		1.011	9577.95	1.961	1.824	524.91	6083.57
		1.6	9555.09	1.956	1.801	530.67	6256.49
$0.3b_f$		1.13	8416.15	1.952	1.710	502.03	5434.26
		1.6	8415.77	1.948	1.696	501.23	5623.83

3.5 Analysis of the results

In this section, a detailed analysis of the results obtained in the 158 simulated tests is presented. The discussion is organised in subsections, each of those focusing on the role of each investigated parameter in the response of the RBS in the assemblies of study.

3.5.1 Influence of the yield stress f_y

The role of the yield stress is very obvious when observing figures 3.39 and 3.40. It is very clear that almost all specimens achieved a very substantial amount of overstrength with respect to their nominal strength M_{Rd} , and especially so did the S235 specimens. Most specimens with S355 steel achieved a M_{40}/M_{Rd} ratio of 1.0-1.6, while S235 specimens reached values of about 1.3-2.2, exhibiting larger overstrength in a consistent manner.

This is clearly shown in figure 3.47, where the M_{40}/M_{Rd} ratios are shown for all the specimens. The charts are organised by flange cutouts with the points superposed for S355 steel (points indicated in cyan) and for S235 steel (points in magenta).

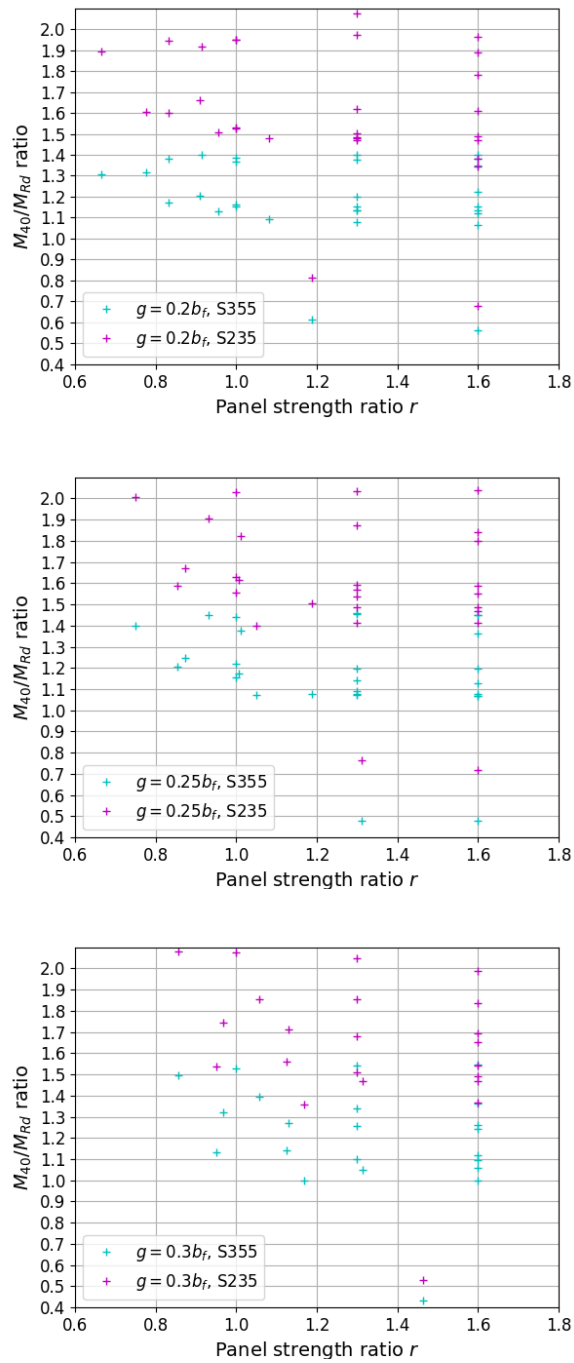


Figure 3.47: M_{40}/M_{Rd} ratios vs web panel strength r . S355 in cyan and S235 in magenta

This larger overstrength in lower grade steels is widely known and it is found in the literature such as in this work by Yun and Gardner [58]. This overstrength is reflected in the material model parameters introduced in the software. For the S355 steel, the measured yield stress is $f_{y,355,real} = 386N/mm^2$ and for the S235 steel the true yield stress is $f_{y,235,real} = 310N/mm^2$. Moreover, apart from this overstrength associated to the actual yield stress of the material, the cyclic hardening of the steel also plays a very relevant part. The cyclic hardening of the steel has elevated the strength numbers even higher to what can be observed in the charts. The material parameters introduced in the model correspond to laboratory test data obtained from the literature on S355 and S235 steels, and similar results should be expected with other S355 and S235 steel specimens.

These high strength values obtained may seem like an advantage, but these results seem to indicate that the material randomness and strain-hardening coefficients recommended in EN1998-1 [18] may be too low for their application to RBS designs. In EN1998-1 the strain-hardening factor is taken as 1.1, while the overstrength factor recommended is 1.25. With these results obtained in this PhD thesis in mind, it makes sense to establish these values according to the cross-section type and specific steel grade, as it is being done for the new revision of Eurocode 8. That being said, the factor that may need to be changed by the largest amount is the strain-hardening coefficient, since a small 10% extra strength does not make up for the cyclic hardening of the material by any means at all. Many specimens in S235 steel grade have literally doubled their design strength, and the current rules of EN1998-1 do not account for such a large effect.

It should also be noted that the design of the column and the column web panel zone strength are done according to the beam flexural strength. The facts exposed earlier may be a problem when assessing the column flexural overstrength and the web panel strength: a panel zone designed as with a strength balanced with that of the beam may be in fact a weak panel. This issue can be even worse in the case of a design of a beam-to-column assembly with a beam in S235 steel and S355 column to promote the plastic hinge forming in the beam. In that case, using the values recommended in EN1998-1 may lead to a very underestimated beam strength and a column web panel strength much lower than expected in the design, since S355 steel exhibits smaller overstrength and strain-hardening than that of S235.

And analogously to the previous point regarding the column and panel zone design, the beam-to-column connection can also incur in the same overstrength problem. This specific connection problem may be resolved if the connection is done with full penetration butt welds, as indicated in EN1998-1 [18], clause 6.5.5 - (2). In

that case, the non-dissipative connections of dissipative members can be deemed to satisfy the overstrength criterion. However, the specimens with S235 steel presented lower stress levels at the welds due to the smaller flexural resistance of the RBS. This effect can be observed in figure 3.48.

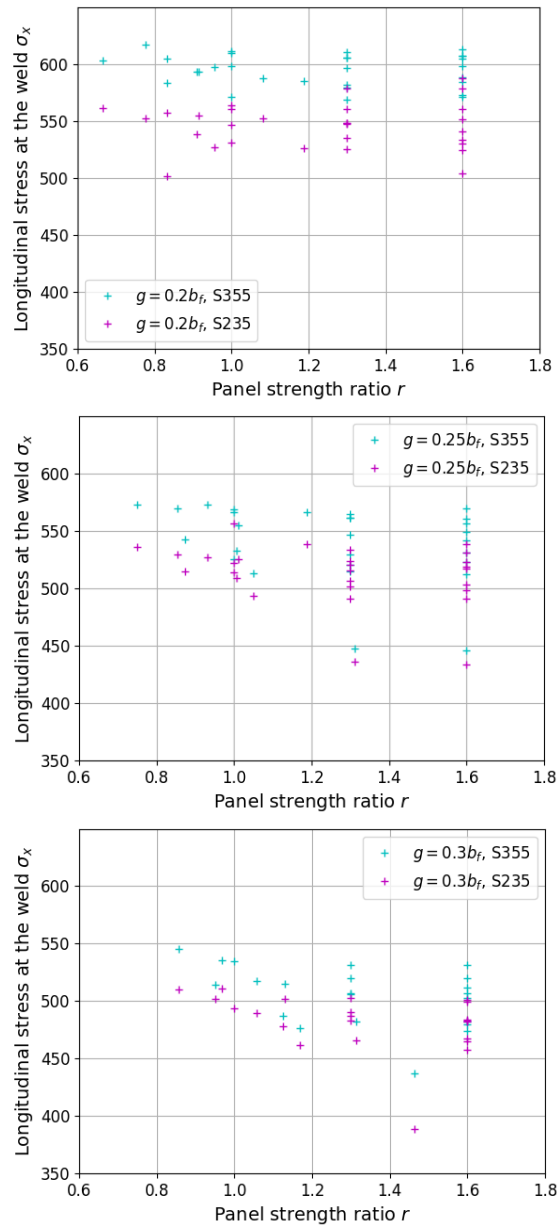


Figure 3.48: Maximum average longitudinal stress σ_x in the welds (in N/mm^2) against the panel strength ratio r . S355 in cyan and S235 in magenta

It is clearly visible that the values for specimens in S355 steel are consistently higher. This is to be expected, since the strength of the RBS is higher due to the higher strength of the steel alloy.

3.5.2 Influence of the trimmed flange width g

The influence of the parameter g has been studied giving this parameter three possible values in this thesis, namely $0.2b_f$, $0.25b_f$ and $0.3b_f$. From the results obtained, detailed in tables 3.17 through 3.20 and figures 3.37 through 3.46 several facts can be pointed out.

A reduction of flange width directly implies a reduction in flexural strength. Similar assemblies with identical beam and column cross-sections, the same panel zone strength ratio r and the same steel grade can be compared to find any differences, and indeed it has been found that reducing more and more flange width causes a decrease in maximum flexural strength M_{max} and also a decrease in degraded bending moment at 40mrad M_{40} . However, this loss in bearing capacity does not significantly affect the M_{40}/M_{Rd} ratio, which tends to be around the same value for all the cases for a given beam-column assembly made with the same steel. There just appears to be a small tendency in the smaller, more compact profiles that exhibited more stable hysteresis loops and very little local buckling, where it can be observed that a larger trimmed width can result in a slightly larger M_{40}/M_{Rd} in many cases, albeit with small differences, as it can be seen in table 3.21.

Table 3.21: Effect of g on the M_{40}/M_{Rd} ratio for some specimens

Profile - Steel grade	r	g	M_{40}/M_{Rd}
HEA450 - S355	$r = 1.0$	$0.2b_f$	1.367
		$0.25b_f$	1.439
		$0.3b_f$	1.529
	$r = 1.3$	$0.2b_f$	1.378
		$0.25b_f$	1.454
		$0.3b_f$	1.543
	$r = 1.6$	$0.2b_f$	1.383
		$0.25b_f$	1.449
		$0.3b_f$	1.544
HEA450 - S235	$r = 1.0$	$0.2b_f$	1.949
		$0.25b_f$	2.031
		$0.3b_f$	2.073
	$r = 1.3$	$0.2b_f$	2.077
		$0.25b_f$	2.034
		$0.3b_f$	2.045
	$r = 1.6$	$0.2b_f$	1.964
		$0.25b_f$	2.039
		$0.3b_f$	1.990
IPE450 - S355	$r = 1.0$	$0.2b_f$	1.164
		$0.25b_f$	1.156
		$0.3b_f$	1.132
	$r = 1.3$	$0.2b_f$	1.133
		$0.25b_f$	1.092
		$0.3b_f$	1.102
	$r = 1.6$	$0.2b_f$	1.134
		$0.25b_f$	1.077
		$0.3b_f$	1.095
IPE450 - S235	$r = 1.0$	$0.2b_f$	1.530
		$0.25b_f$	1.556
		$0.3b_f$	1.536
	$r = 1.3$	$0.2b_f$	1.480
		$0.25b_f$	1.536
		$0.3b_f$	1.511
	$r = 1.6$	$0.2b_f$	1.382
		$0.25b_f$	1.470
		$0.3b_f$	1.493

Figures 3.49 and 3.50 show a comparison between two similar specimens from the same beam-to-column assembly. Two IPE450 beams are compared side by side in S355 steel, with a strong panel zone $r = 1.6$. On the left, $g = 0.2b_f$ and on the right $g = 0.3b_f$. Lateral displacements and equivalent plastic strains (PEEQ) are compared, respectively. The kinking of the beam flanges is very clear in the $g = 0.3b_f$ case and the flanges concentrate much more plastic damage with higher PEEQ levels.

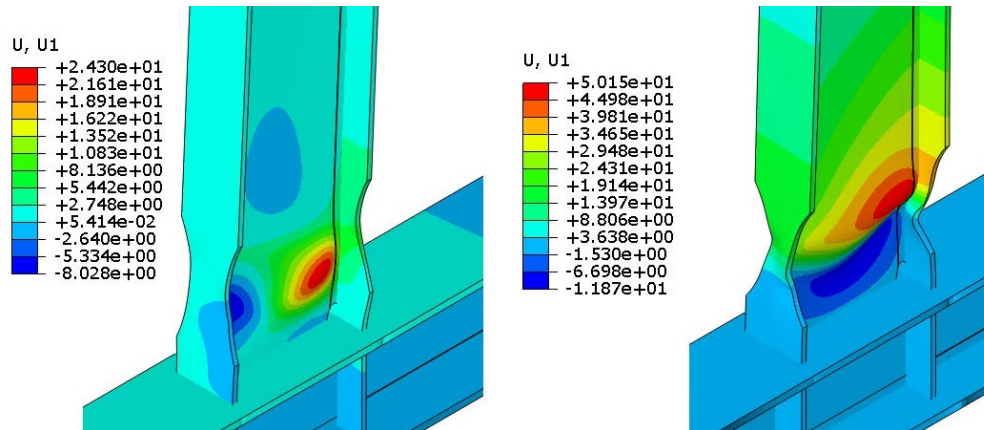


Figure 3.49: Comparison of lateral displacements in two similar specimens. $g = 0.2b_f$ (left) and $g = 0.3b_f$ (right). IPE450 - HEB340 assembly, $r = 1.6$, S355 steel grade

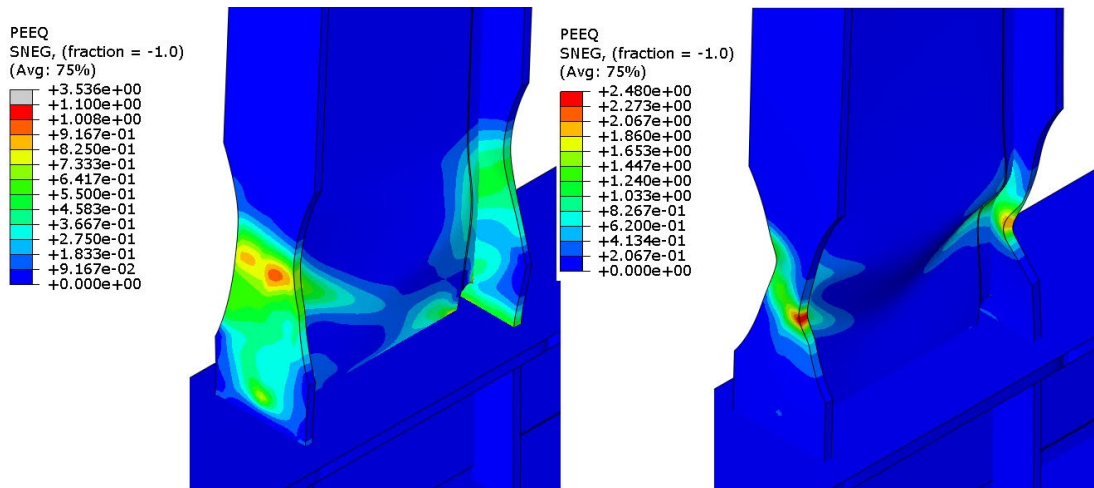


Figure 3.50: Comparison of equivalent plastic strains in two similar specimens. $g = 0.2b_f$ (left) and $g = 0.3b_f$ (right). IPE450 - HEB340 assembly, $r = 1.6$, S355 steel grade

It is clear that the beam with smaller flanges experiences lateral-torsional buckling as well as local buckling of the flanges and web, while the case with more flange width only has local buckling in the flanges and web. Moreover, the $g = 0.2b_f$ has smaller out-of-plane displacements in the web and no severe kinking of the flanges can be observed. Excessive kinking of the beam flanges needs to be avoided, since these areas in the kinks are prone to developing fracture in the flanges, losing structural integrity and dissipative capacity. The beam in figure 3.49 on the left does not experience lateral-torsional buckling and exhibits stable behaviour with no fracture risk as long as the weld is properly designed and executed. Figure 3.51 shows the two moment-rotation diagrams for both specimens.

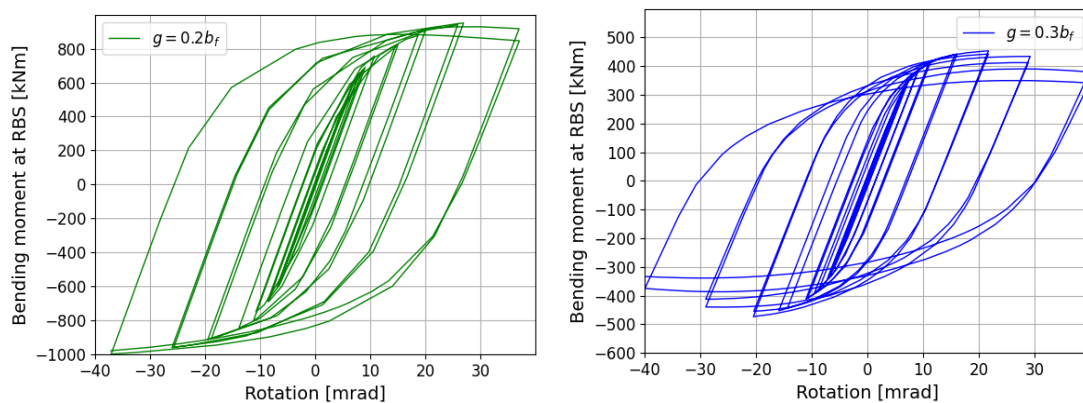


Figure 3.51: Comparison of moment-rotation diagrams in two similar specimens. $g = 0.2b_f$ (left) and $g = 0.3b_f$ (right). IPE450 - HEB340 assembly, $r = 1.6$, S355 steel grade

As it can clearly be observed, the specimen with the smaller reduction of the flanges achieved higher bending strength and retained higher strength at 40mrad. On the other hand, the specimen with $g = 0.3b_f$ (in blue) experienced higher strength loss, probably due to lateral-torsional buckling. The M_{max}/M_{40} ratios are 0.857 and 0.803, respectively, although M_{40}/M_{Rd} values are quite similar being 1.134 and 1.095.

Also, it must be noted that the flange kinking poses a great risk of fracture, which the model developed is not able to reflect. The possibility of fracture due to kinking may be reduced by providing the beam with lateral bracing to avoid lateral-torsional buckling and prevent or reduce flange kinking. EN1998-1 in clause 6.6.2 - Beams states that "beams should be verified as having sufficient resistance against lateral and lateral-torsional buckling in accordance with EN1993, assuming the formation of a plastic hinge at one end of the beam [...]". Although this clause makes a lot of sense on paper and is written with the best of intentions,

it may not always be trivial to estimate the strength required due to the formation of a plastic hinge, as shown in the simulations performed in this study. The use of lateral bracing systems is not obligatory according to EN1998, but in order to protect the flanges from kinking excessively a lateral brace can be a good solution. As a matter of fact, lateral bracing systems are obligatory according to AISC Seismic Provisions [1] in section D1 - General Member and Connection Design Requirements, clause 2c. - Special Bracing at Plastic Hinge Locations, and these braces should be located at the end of the RBS the furthest away from the column or a short distance away from that end of the RBS. However, the FEMA recommendations do not require the placement of supplemental lateral bracing at plastic hinge locations for beams with composite floor construction (AISC 341 Commentary, Section D1-2c. [1]).

In figures 3.52 and 3.53 another similar comparison is presented. This is the case of an HEA450 beam in S235 steel, with a strong panel zone $r = 1.6$. On the left, $g = 0.2b_f$ and on the right $g = 0.3b_f$.

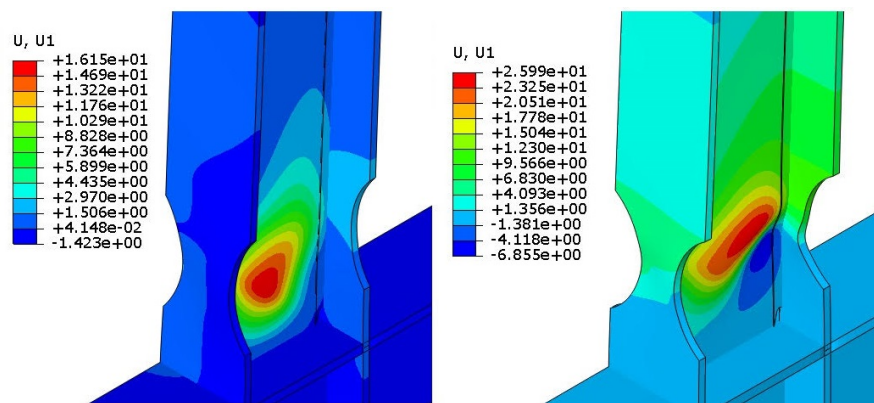


Figure 3.52: Comparison of lateral displacements in two similar specimens. $g = 0.2b_f$ (left) and $g = 0.3b_f$ (right). HEA450 - HEB500 assembly, $r = 1.6$, S235 steel grade

As it can be observed in this case as well, the weaker beam experiences lateral-torsional buckling as well as local buckling, while the $g = 0.2b_f$ case only has some small local buckling in the web and flanges. And despite one of the specimens experiencing lateral-torsional buckling and visibly more local buckling, the strength degradation in both cases is very similar (see figure 3.54).

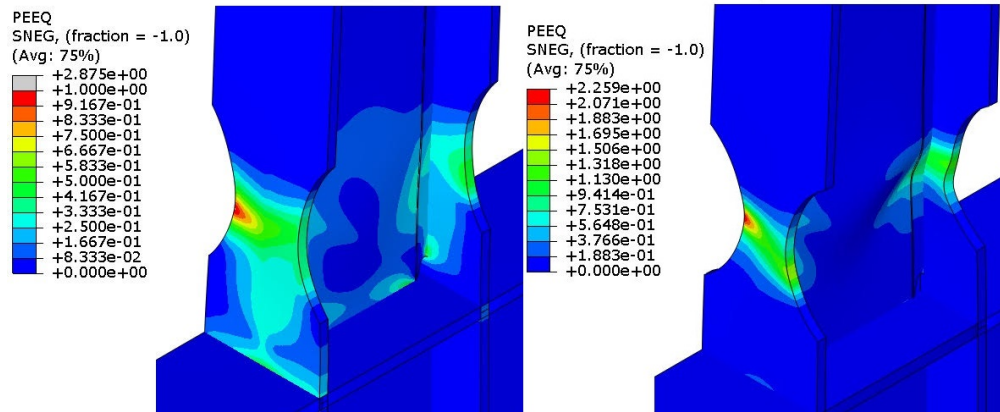


Figure 3.53: Comparison of equivalent plastic strains in two similar specimens. $g = 0.2b_f$ (left) and $g = 0.3b_f$ (right). HEA450 - HEB500 assembly, $r = 1.6$, S235 steel grade

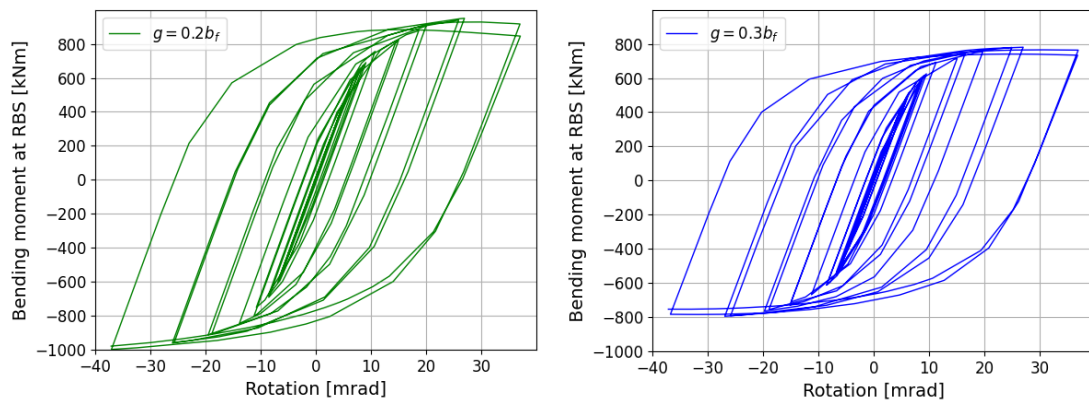


Figure 3.54: Comparison of moment-rotation diagrams in two similar specimens. $g = 0.2b_f$ (left) and $g = 0.3b_f$ (right). HEA450 - HEB500 assembly, $r = 1.6$, S235 steel grade

However, despite the two cases disclosed above where the case with more flange width does not experience lateral-torsional buckling and the case with less flange width does, it is common to see both extremes to incur in lateral-torsional buckling, as shown in figures 3.55 and 3.56. This is the case of an HEA1000 beam in S235 steel, with an unreinforced panel zone. On the left, $g = 0.2b_f$, $r = 1.082$ and on the right $g = 0.3b_f$, $r = 1.314$.

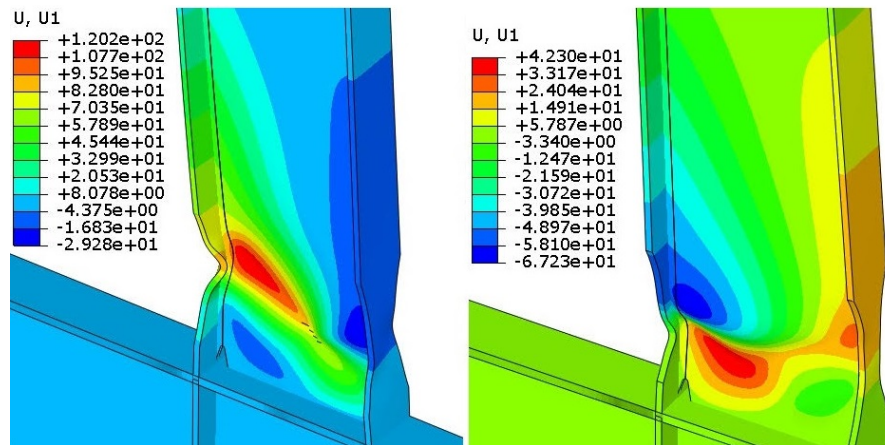


Figure 3.55: Comparison of lateral displacements in two similar specimens. $g = 0.2b_f$, $r = 1.082$ (left) and $g = 0.3b_f$, $r = 1.314$ (right). HEA1000 - HE1000x393 assembly, S235 steel grade

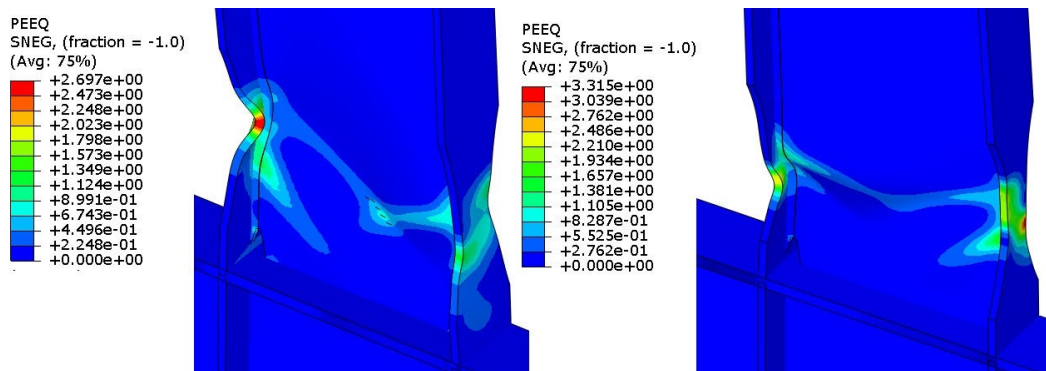


Figure 3.56: Comparison of equivalent plastic strains in two similar specimens. $g = 0.2b_f$, $r = 1.082$ (left) and $g = 0.3b_f$, $r = 1.314$ (right). HEA1000 - HE1000x393 assembly, S235 steel grade

In this case, both specimens experience lateral-torsional buckling, and it is even possible to see how one flange moves laterally in one direction, while the other heads the other way. The flange kinking is similar in both cases, and PEEQ values are also similar. And figure 3.57 shows the moment-rotation diagrams for both specimens.

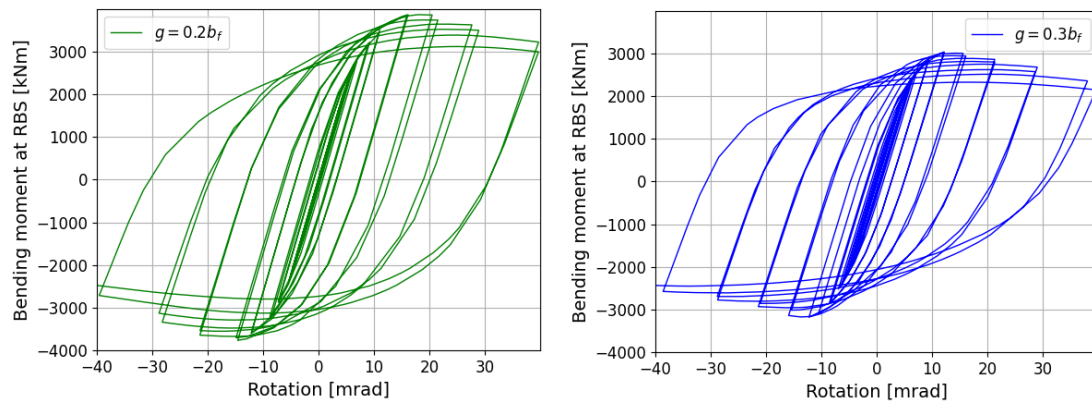


Figure 3.57: Comparison of moment-rotation diagrams in two similar specimens. $g = 0.2b_f$, $r = 1.082$ (left) and $g = 0.3b_f$, $r = 1.314$ (right). HEA1000 - HE1000x393 assembly, S235 steel grade

As it can be seen, similar strength degradation is exhibited by both specimens. So in this case both specimens exhibit lateral-torsional buckling, which causes the behaviour of both to be quite similar in terms of strength degradation, local buckling and flange kinking, and even PEEQ concentration patterns in the RBS flanges. Again, the presence of a lateral brace could improve the behaviour in these cases, since lateral-torsional buckling would be avoided and flange kinking would be either avoided or reduced, diminishing the risk of fracture initiation in the flanges.

In order to avoid this drawback from weakening the beam flanges, another strategy has recently arisen. The Reduced Web Section (RWS) is an alternative to RBS which tries to adopt a similar approach to the formation of a plastic hinge by weakening the web by cutting a hole in it [13]. The early results are quite promising, but further research is still needed. Another relatively new solution to this problem is the Drilled Flange Connection (DFC) which also seems to be a viable alternative [5], [57]. The available results on DFCs are still limited, so further studies are necessary.

Also, from the reduction in flexural strength derived from the flange cutout, a reduction in weld stresses can be observed when the flange trimmed width is increased. Figure 3.58 shows the results obtained sorted by steel grades.

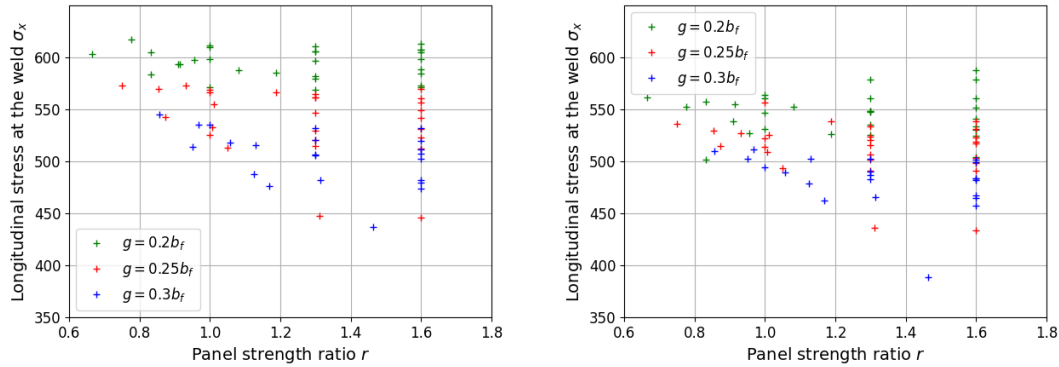


Figure 3.58: Maximum average longitudinal stress σ_x in the welds (in N/mm^2) against the panel strength ratio r . S355 (left) and S235 (right)

It is clear that the loss in plastic modulus $W_{pl,RBS}$ entails a reduction in weld stresses. This fact is not only due to the loss of plastic bending capacity, but also to the development of lateral-torsional buckling, which prevents in some cases the assemblies from achieving higher levels of flexural strength.

3.5.3 Influence of the web panel strength ratio r

The web panel strength ratio r appears to affect very minimally the global response of the RBS. The specimens exhibited some small differences when changing only r , but the variations found are very small in all cases, and show no clear trend. M_{max} , M_{40} and M_{40}/M_{max} ratios remain almost the same with minor variations across all the specimens (see tables 3.17 through 3.20).

However, the change in r did alter the degree of plastic engagement of the column greatly. In figure 3.59, a comparison of the plastic engagement of the elements of the model when varying r is presented. This case corresponds to the case of an HEA450 - HEB340 assembly, with a trimmed flange width of $0.2b_f$ in S235 steel. The areas in red are actively yielding, while the blue areas are in a stress state inside the yield surface in elastic range.

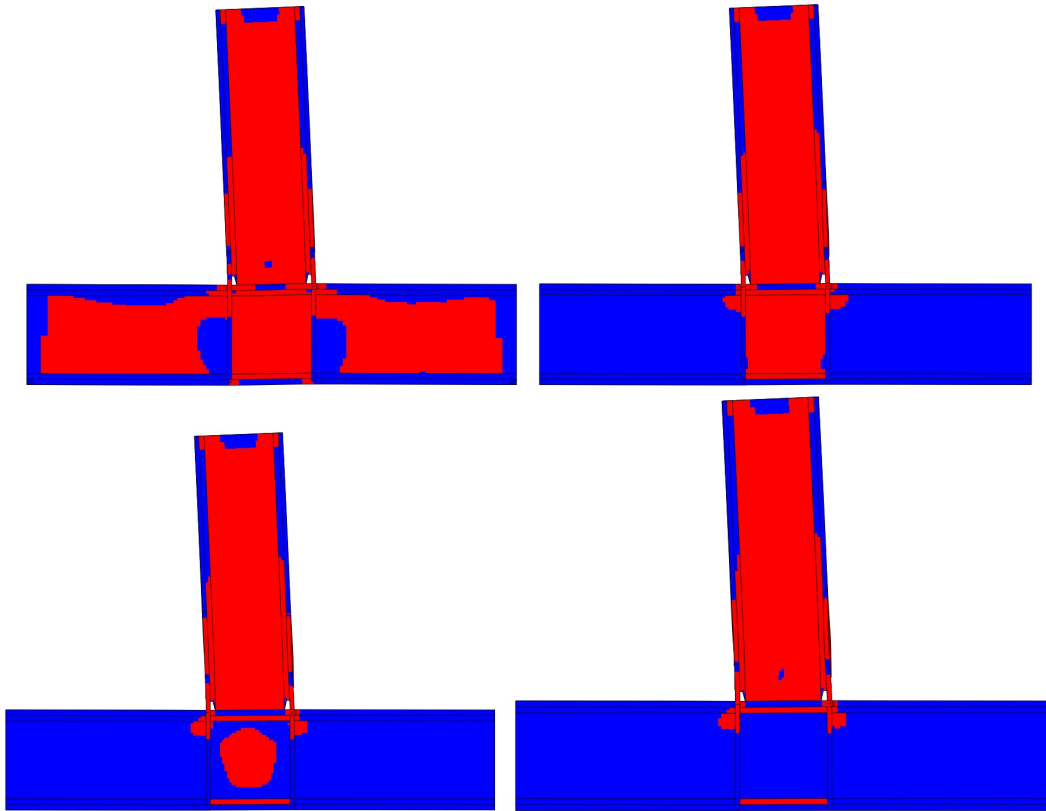


Figure 3.59: Comparison of plastic engagement in four similar specimens. HEA450 - HEB340 assembly, $g = 0.2b_f$, S235 steel grade. $r = 0.666$ (top left), $r = 1$ (top right), $r = 1.3$ (bottom left) and $r = 1.6$ (bottom right)

It is clearly visible from the figure that up to a ratio of $r = 1.6$ some damage occurs in the panel zone. Even with an overstrength of $r = 1.3$ the panel zone is yielded, which causes permanent damage to the column despite the strong panel design. Also, it can be observed that the beam web is fully plastic. In the cases where the flange reduction is relatively small like $g = 0.2b_f$ (the same as the case in figure 3.59) the shear force introduced in the beam at the end of the test (when a plastic hinge has already clearly formed) can be of relevance, and in some cases even be higher than 50% of the plastic shear resistance of the beam, which according to EN1993-1-1, clause 6.2.8 [16] would require an interaction rule to take this effect into account. However, in figure 3.59 the case on the top left corner reached a shear force value of $1.03V_{pl}$ and exhibited very good behaviour, with no apparent loss of flexural strength due to high shear. This is probably due to the great strain-hardening capabilities of S235 steel. M-V interaction in RBS has been studied previously by Crisan and Dubina in [11], but research on this area is still very limited. Figure 3.60 shows the main results obtained at the end of the

simulation for the top left case in terms of lateral displacements, Von Mises stresses and equivalent plastic strains. Also, the moment-rotation diagram is shown.

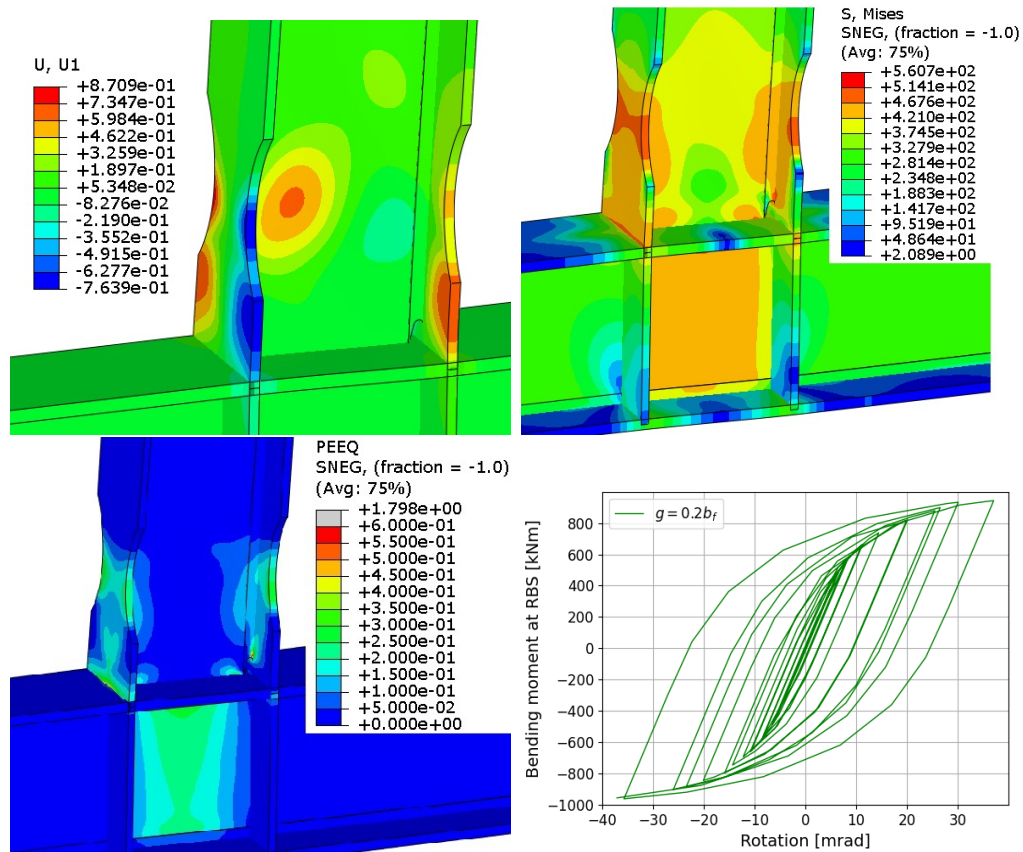


Figure 3.60: Main results obtained for the HEA450 - HEB340 assembly, $g = 0.2b_f$, $r = 0.666$, S235 steel grade. Lateral displacements (in mm, top left), Von Mises stresses (in N/mm^2 top right), equivalent plastic strains (bottom left) and moment-rotation diagram (bottom right)

The great strain-hardening of S235 steel like in the previously exposed case allows for the beam to develop high shear in the web along the whole span as well as a plastic hinge due to bending in the RBS. However, with S355 steel specimens, the levels of shear stress are lower, where strain-hardening achieves lower (although still substantial) levels. Figure 3.61 shows the same HEA450 - HEB340 assembly in S355 steel. The flange trimmed width is the same $g = 0.2b_f$, as well as the panel strength ratios r .

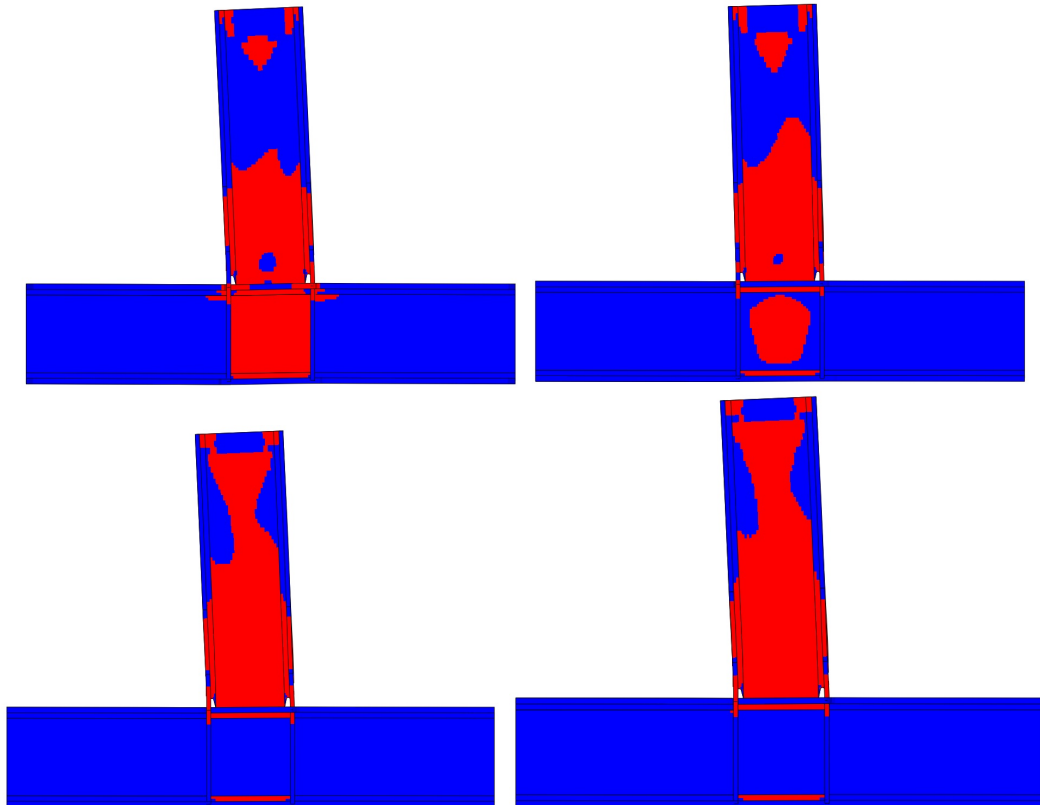


Figure 3.61: Comparison of plastic engagement in four similar specimens. HEA450 - HEB340 assembly, $g = 0.2b_f$, S355 steel grade. $r = 0.666$ (top left), $r = 1$ (in N/mm^2 top right), $r = 1.3$ (bottom left) and $r = 1.6$ (bottom right)

In this case with S355 steel, it is clear that the column web panel is experiencing less of a plastic engagement for a given ratio r . Also, as the column web panel strength increases, it shifts more of the plastic engagement onto the beam web. Despite substantial yielding of the beam web, the specimen on the top left achieved a level of shear of $0.71V_{pl}$. Still substantial, but much lower than the previous case with $1.03V_{pl}$.

Again, detailed results are presented for the top left case ($r = 0.666$) in figure 3.62.

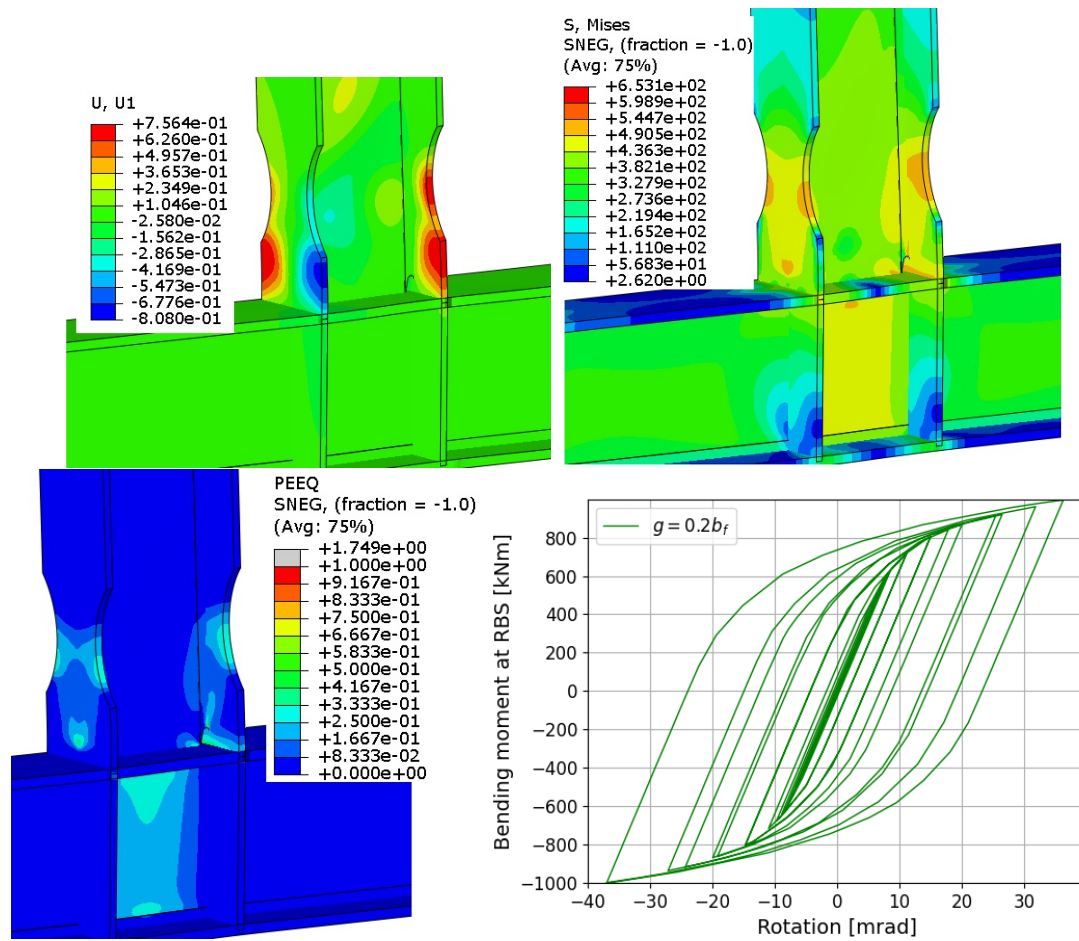


Figure 3.62: Main results obtained for the HEA450 - HEB340 assembly, $g = 0.2b_f$, $r = 0.666$, S355 steel grade. Lateral displacements (in mm, top left), Von Mises stresses (top right), equivalent plastic strains (bottom left) and moment-rotation diagram (bottom right)

No relevant influence of the column web panel zone strength ratio r has been found on the weld stresses, which remain around the same values when only r is varied.

3.5.4 Influence of the slenderness of the member plates

It is clear from figures 3.63 and 3.64 that there appears to be a relationship between the slenderness of the members plates and the strength achieved. Especially the web slenderness figures seem to indicate that a curve exists, where the points tend to fall quite close.

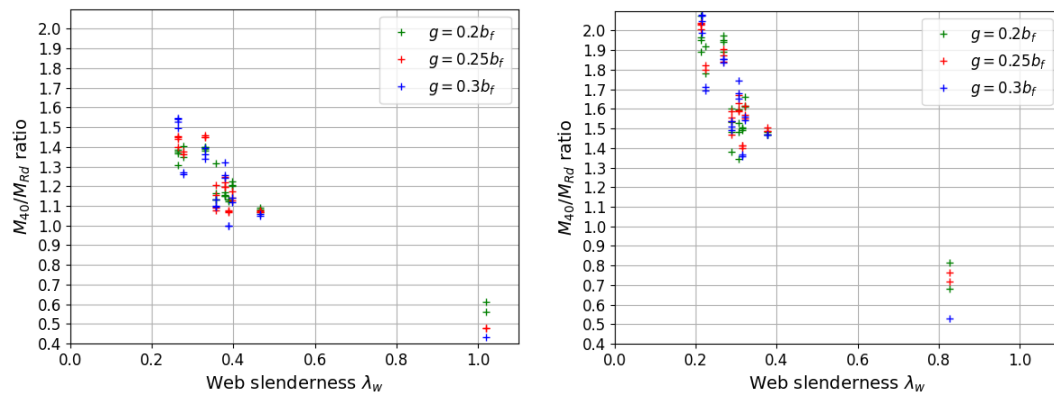


Figure 3.63: M_{40}/M_{Rd} ratios vs RBS web slenderness λ_w . $g = 0.2b_f$ in green, $g = 0.25b_f$ in red and $g = 0.3b_f$ in blue. S355 steel (left) and S235 steel (right)

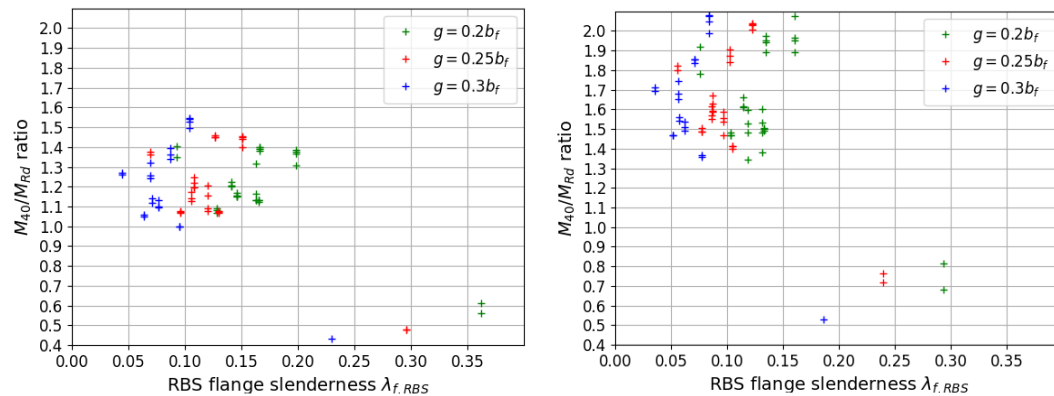


Figure 3.64: M_{40}/M_{Rd} ratios vs RBS flange slenderness $\lambda_{f,RBS}$. $g = 0.2b_f$ in green, $g = 0.25b_f$ in red and $g = 0.3b_f$ in blue. S355 steel (left) and S235 steel (right)

Unfortunately, there is a large gap between the points corresponding to the hot-rolled beam profiles and the built-up girder, which is a lot more slender than the rest and exhibits poor behaviour. More specific research is needed in a wider variety of slendernesses for the web and flanges in order to draw solid conclusions, but these results may indicate that web and/or flange slenderness might be a parameter to influence the design of a RBS. As for the Jumbo American section, it showed M_{40}/M_{Rd} ratios of around 1.3 in S355 steel and around 1.8 in S235 steel, so it is one of the sections that appears towards the top of the charts with substantial overstrength.

The built-up girder is the beam that performed the worst out of all the profiles studied, consistently exhibiting large degradation of flexural strength. Even

in S235 steel, with class 2 flanges and class 3 web the behaviour was still far from ideal. Therefore, it is not advised to use such kind of section for a dissipative seismic design, not even in a DCM design even if EN1998-1 allows the use of class 3 cross-sections. However, the absence of a lateral brace is very noticeable in the results of the analysis where large lateral displacements can be observed. This kind of more slender sections might have some value for seismic applications in DCM structures if provided with lateral braces. Further research on this area is needed to deny or confirm this possibility.

The influence of the web slenderness on the response of the RBS is shown in figures 3.65 and 3.66. These images show the PEEQ contours and the lateral displacement contours of an HEA450 specimen with $g = 0.3b_f$, $r = 1$ in S355 steel (figure 3.65), and an IPE750 specimen with $g = 0.3b_f$, $r = 1.168$ in S355 steel (figure 3.66).

The comparison between these two specimens is motivated by the following: the HEA450 specimen has a web slenderness of $\lambda_w = 0.265$ and flange RBS slenderness of $\lambda_{f,RBS} = 0.104$. On the other hand, the IPE750 specimen has $\lambda_w = 0.389$ and $\lambda_{f,RBS} = 0.095$. As a result, figures 3.65 and 3.66 compare the results obtained for two specimens, when varying λ_w but with both having similar flange slendernesses, panel strength ratios and steel grades.

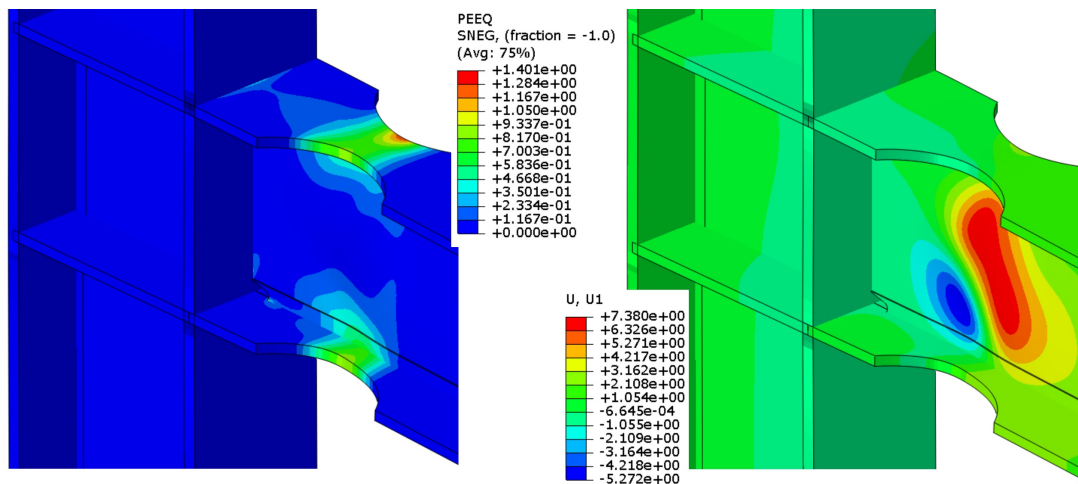


Figure 3.65: PEEQ contours for HEA450 (left) and lateral displacement contours (in mm, right). $g = 0.3b_f$, $r = 1$, S355 steel

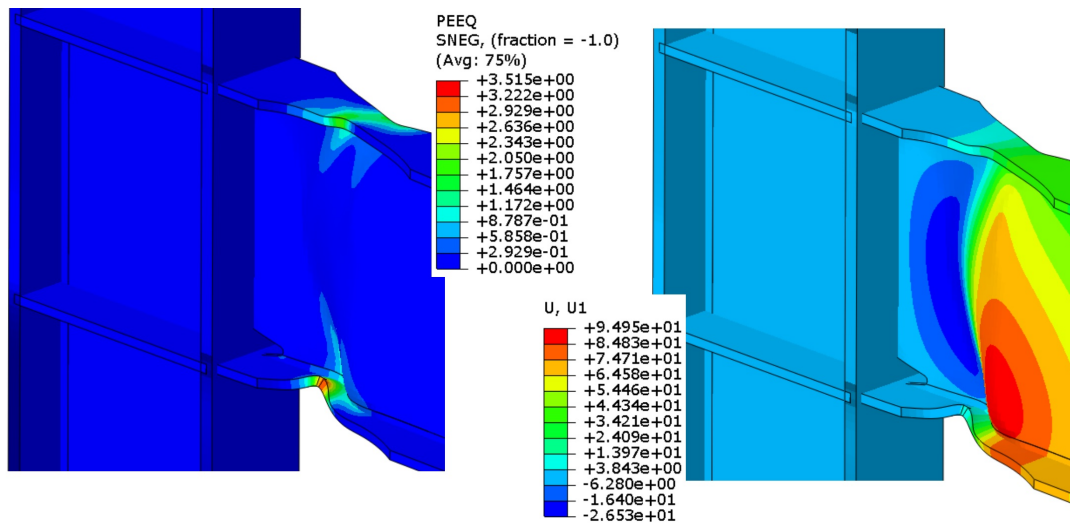


Figure 3.66: PEEQ contours for IPE750 (left) and lateral displacement contours (in mm, right). $g = 0.3b_f$, $r = 1.168$, S355 steel

It is clear that the IPE750 specimen developed very obvious lateral-torsional buckling with lateral displacements of almost 10cm and kinking in the flanges. On the contrary, the HEA450 specimen only presented 7mm displacement in the web, and the flanges do not experience any kinking at all with lower PEEQ levels. Due to all this, the M_{40}/M_{Rd} ratios are very different in both cases. The IPE750 specimen presents a M_{40}/M_{Rd} ratio of exactly 1.000, while the HEA450 exhibited a ratio of 1.529. It is then clear that lateral-torsional buckling development greatly reduces the residual strength of the RBS at 40mrad rotation.

Aside from the slender plated girder, all the specimens exhibited good behaviour and managed to retain good strength at 40mrad rotation, above the $0.80M_{pl}$ target. If lateral-torsional buckling and subsequent flange kinking is avoided, all hot-rolled sections could improve their behaviour and exhibit possibly very stable hysteresis loops. More research is needed on RBS with lateral bracing in order to quantify such benefit.

3.6 Statistical analysis of the results obtained for γ_{sh}

As it has been observed in the previous section, the response of the RBS depends on a variety of factors and different levels of overstrength (M_{max}/M_{Rd}) are reached for each beam-to-column assembly with a given dog-bone geometry. This magnitude M_{max}/M_{Rd} is very relevant for the use of RBS in a seismically-resistant structure, since this overstrength makes it necessary to design non-dissipative members of the structure to withstand that overstrength, ensuring appropriate global structural behaviour.

From all the data obtained in the simulations, it is possible to perform a statistical analysis to derive a characteristic value for the strain-hardening coefficient γ_{sh} . As for the material randomness coefficient γ_{ov} a statistical analysis cannot be performed due to the fact that only one S235 and one S355 steel have been used in the simulations.

The statistical analysis performed herein intends to obtain a characteristic value of γ_{sh} to be used as a design value. Due to the variety of behaviours exhibited by all the assemblies in the simulations, the following statistical analysis is only performed for the European hot-rolled cross-sections (discarding the results for the Jumbo and built-up girder sections).

Firstly, the strain-hardening coefficient value is obtained for every case considered in this statistical analysis. The ratios M_{max}/M_{Rd} have been divided by the material randomness parameter γ_{ov} to obtain each of the γ_{sh} values. The values for the material randomness coefficient in the steels used in this study are those proposed in the forthcoming prEN1998-1-2:2020 in clause 11.2.2 [50], where distinct values are adopted for different steel grades (unlike the current version of EN1998-1 [18]). It should be noted that those values are different from the γ_{ov} values obtained from the laboratory test data of the steels used in the present thesis. All the values are indicated in table 3.22:

Table 3.22: Values of the material randomness coefficient γ_{ov} for the steels used in this study

Steel grade	prEN1998-1-2:2020	Laboratory tests
S355	1.25	1.087
S235	1.45	1.319

The data for the European hot-rolled profiles obtained from the simulations have

been plotted and good fits have been achieved with normal distributions for all the considered cases by means of the maximum likelihood method. The normal distribution cumulative probabilities are plotted, and means, standard deviations and 95th percentiles have been obtained. The statistical processing of the data has been performed with the statistical and machine learning toolbox in MATLAB [29] in a similar fashion to this study [3].

3.6.1 γ_{sh} values using prEN1998-1-2:2020 values for γ_{ov}

After dividing all M_{max}/M_{Rd} ratios by the corresponding γ_{ov} values in prEN1998-1-2:2020 [50] ($\gamma_{ov,355,EN1998-1-2} = 1.25$ and $\gamma_{ov,235,EC8} = 1.45$) a fitting normal distribution is obtained. The fit for S355 steel grade can be seen in figure 3.67 and for S235 steel grade in figure 3.68.

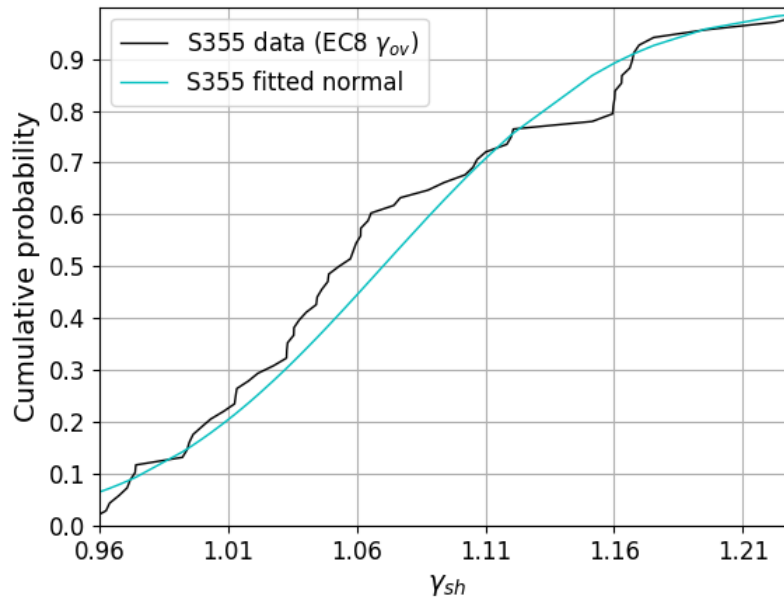


Figure 3.67: Statistical fit of γ_{sh} values for S355 steel grade with fitted normal distribution. $\gamma_{ov,355,EC8} = 1.25$. Mean: 1.070, standard deviation: 0.0729, 95th percentile: 1.190

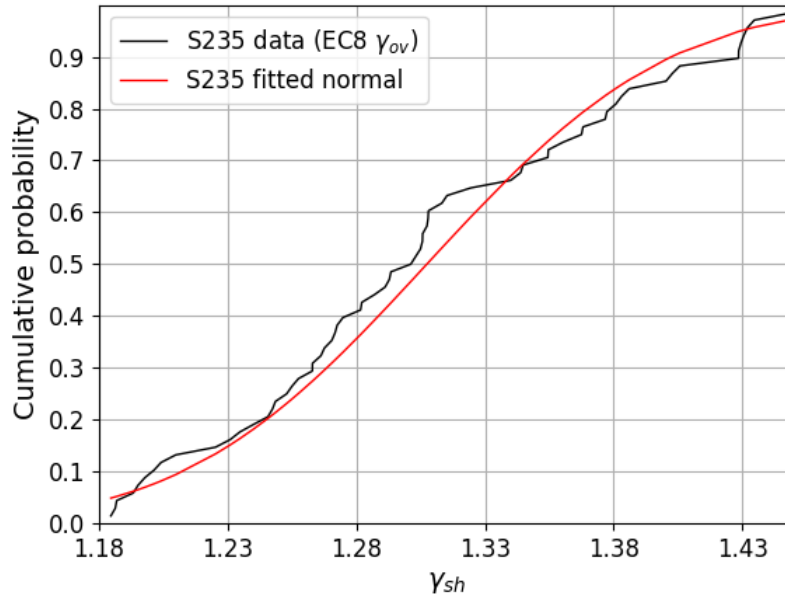


Figure 3.68: Statistical fit of γ_{sh} values for S235 steel grade with fitted normal distribution. $\gamma_{ov,235,EC8} = 1.45$. Mean: 1.307, standard deviation: 0.0742, 95th percentile: 1.429

3.6.2 Summary of the values obtained for the γ_{sh} distributions

After the statistical analyses have been performed the fitting normal distributions have been obtained. The values are reported in table 3.23.

Table 3.23: Relevant values obtained for the normal distributions for the fit of γ_{sh} values

Steel grade	prEN1998-1-2:2020		
	μ	σ	$P_{95\%}$
S355	1.070	0.0729	1.190
S235	1.307	0.0742	1.429

According to the results obtained shown in table 3.23, when the design of a RBS is done with the values of γ_{ov} recommended in prEN1998-1-2:2020 [50] the characteristic values for γ_{sh} for steel grades S355 and S235 are 1.190 and 1.429, respectively.

However, the prescribed value for γ_{sh} , according to prEN1998-1-2:2020 [50] to be applied in the non-dissipative zones of moment resisting frames working in bending is given by the following expression:

$$\gamma_{sh} = \frac{f_y + f_u}{2f_y} \leq 1.20 \quad (3.14)$$

and has an upper bound value of 1.20. As it has been found in the present study, a $\gamma_{sh} = 1.20$ value is reasonable for a S355 steel grade, but not for S235. The value of 1.20 is substantially below the 95th percentile value obtained from the previous statistical analysis (1.429) and may potentially lead to unconservative designs.

4 Structural behaviour under seismic actions. Benefits of the dog-bone

4.1 General

After the seismic events of Kobe and Northridge, much research was undertaken to develop new solutions for connections in seismic areas in order to avoid brittle failures in steel structures, especially in the connections. A huge prequalification task was completed in the SAC project funded by FEMA from which the RBS arose as a new solution for buildings in seismic areas. Much has been already said about the RBS in the previous sections about its local as well as its global benefits. So, as a summary, the most relevant advantages of the Reduced Beam Section are listed below.

Local benefits:

- The RBS provides more uniform yielding within the reduced flange portion of the beam, creating a reliable, stable and uniform plastic hinging location.
- It offers the possibility to avoid brittle failure in the connection by protecting the welds and keeping them in their elastic range.
- Improves rotation capacity of the plastic hinges: by trimming the flange width the flanges are more compact and more stable under severe cyclic actions, delaying buckling phenomena and exhibiting better hysteretical behaviour.
- Allows for greater plastic dissipation: more hysteretical stable behaviour allows for greater plastic strains in the RBS flanges, which helps dissipate more energy by plastic strains.

Global benefits:

- The plastic engagement of the beam ends induces more lateral flexibility, which has an lowering effect on base shear when subjected to extreme lateral pushing actions. However, it also reduces the lateral stiffness of the structure: although elastic stiffness remains almost identical in the structure, smaller horizontal forces are needed to cause yielding in the RBS.
- Allows for greater imposed displacements: better rotation capacity at the beam ends makes it easier to achieve large imposed displacements during a seismic event.

In order to better appreciate and quantify the effects of the RBS on global structural behaviour, two studies have been conducted. One of them using pushover analysis (Jiménez et al. [31]), the other one using nonlinear time-history analysis (Jiménez et al. [32]).

4.2 First study, pushover analysis

The aim of this study is to evaluate the behaviour of a MRF and a D-EBF when subjected to a lateral set of pushing forces and to investigate on the effects of the RBS in such structural typologies. The behaviours of conventional MRF and D-EBF are compared to those of a similar structure when provided with RBS at the beam ends in all spans and storeys.

In order to achieve such objective, a numerical model is developed using the software Abaqus [56] to reproduce the cyclic behavior of RBS in HEA240 sections and to obtain moment-rotation curves. These moment-rotation diagrams are then introduced in a FEM using beam elements in SAP2000 [10] to assess the behaviour of the structures when subjected to seismic load with dog-bone joints and to compare their responses with those of two control structures with identical configurations but without RBS.

The studied structure is a six-storey four-span planar frame belonging to a regular symmetric 3D structure. The interstorey height is 3.5m for all levels and the span between adjacent columns is 6m. All columns are modelled perfectly fixed to the foundation. All the beams are predesigned under gravity loads for ULS and SLS, and the cross-section adopted for the beams is HEA240.

4.2.1 Moment-rotation curves and numerical modelling

4.2.1.1 Obtainment of the moment-rotation curves

After the validation of the numerical model reproducing the experimental test conducted in [15] a numerical model using Abaqus was developed. The model consisted of a very similar beam-to-column assembly with the same column section HEB300 and a HEA240 beam, subjected to identical loading. The details of the geometry of the RBS can be seen in table 4.1:

The parameters b_f and d_b stand for the beam flange width and beam depth, respectively. After the simulation, moment-rotation curves were obtained for the HE240A beam, both with and without RBS, in order to compare the behaviour of MRF and DEBF with both joint typologies. In the next figure, the moment-rotation diagrams for the RBS and the intact beam section are compared and the

Table 4.1: Parameters of the dog-bone joint for the present study (see figure 3.11). Dimensions in mm

b_f	d_b	a	b	g	s	r
240	230	144	172.5	48	230.3	101.5

vertical axis is the bending moment resisted at the RBS by the specimens.

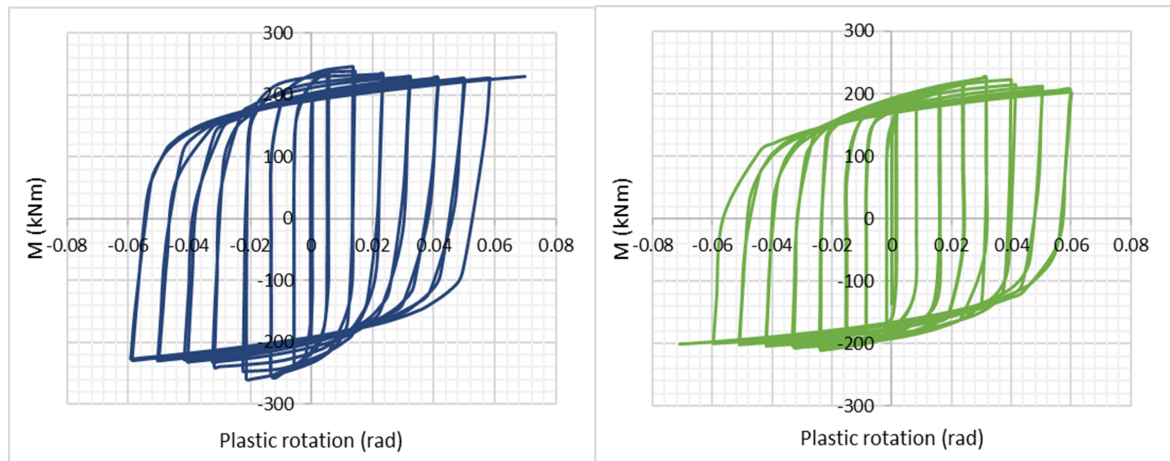


Figure 4.1: Moment-rotation diagrams for the intact section (left) and RBS (right)

The plastic moment of the RBS is 66% of that of the intact HE240A section. In spite of that, the moment-rotation diagrams appear to be quite similar. It has been observed in the Abaqus models that the intact section develops local buckling of the flanges and web for lower levels of rotation than the Reduced Beam Section. This fact shows that the RBS is less sensitive to local buckling having more robust flanges. Therefore, the RBS has greater rotation capacity which allows it to achieve greater levels of strain-hardening making the difference of the graphs smaller than their difference in plastic modulus $W_{pl,RBS}$. These moment-rotation diagrams are incorporated in a SAP2000 model to reproduce the cyclic behaviour of the joints when subjected to lateral loads.

4.2.1.2 Introduction of the moment-rotation curves for the study of the frames

SAP2000 allows for the modification of predefined moment-rotation diagrams available in the standards or in FEMA273 [21], which can be very useful to reproduce

the cyclic behaviour of the joints of the structure by means of a nonlinear static analysis. At every joint where a plastic hinge can potentially develop a moment-rotation diagram is set. In beam-to-column joints the moment-rotation diagrams obtained in Abaqus were introduced. The moment-rotation diagram introduced in SAP2000 corresponds to the backbone curve of the cyclic diagram obtained with Abaqus. It can be observed that the plastic hinge can withstand a bending moment larger than $M_{pl,RBS}$ due to the strain-hardening of the material introduced in the numerical model.

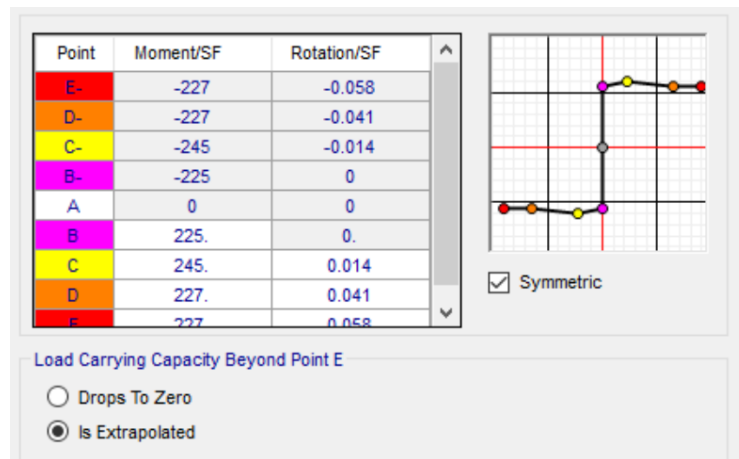


Figure 4.2: Moment-rotation diagram introduced in SAP2000 for the intact beam section

This diagram was introduced in all beam-to-column joints so that in case of that section losing linearity the section behaviour will be taken over by the moment-rotation diagram. This diagram was introduced in the hinges at exactly 115 mm from the face of the column, corresponding to half the beam depth d_b . For the RBS, a similar diagram was introduced. The moment values are in kNm, and the rotation values in rad.

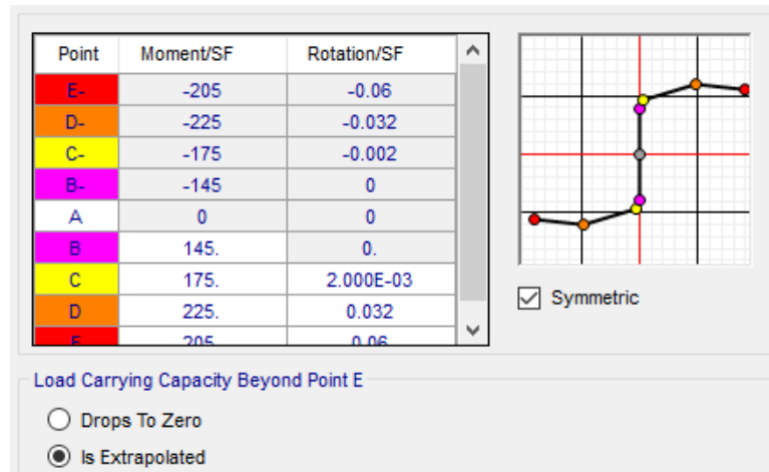


Figure 4.3: Moment-rotation diagram introduced in SAP2000 for the reduced beam section

As it can be observed, in the case of the RBS the ultimate strength is smaller but still reaches $M_{pl,RBS}$ thanks to the strain-hardening of the material. This moment-rotation diagram was introduced at exactly 230 mm from the face of the column corresponding to the midsection of the dog-bone.

In the columns, a N-M type hinge was introduced with its moment-rotation curve determined according to ASCE 41-13 [4] and with the N-M interaction rule in EN1993-1-1, clause 6.2.9.1. Figures 4.4 and 4.5 show the moment-rotation diagram and the interaction curve for the HEB300 columns. The other column profiles (HEB280 and HEB260) had similar values scaled down according to their flexural and axial strength. For the columns, the moment values reported in figure 4.4 are multiples of the plastic moment M_{pl} and the rotation values are multiples of the yield rotation, obtained according to ASCE41-13, eq. 9-2 [4] and is equal to 0.0081mrad.

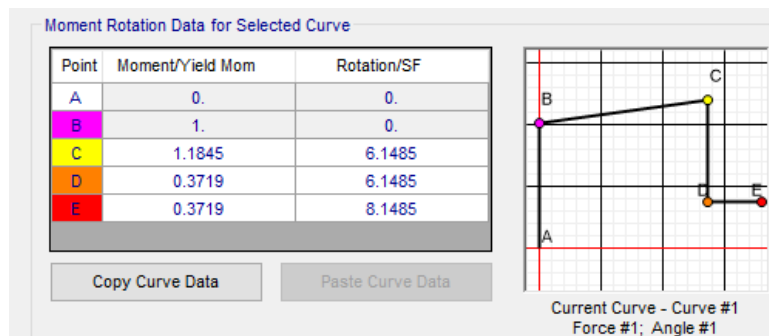


Figure 4.4: Moment-rotation diagram introduced in SAP2000 for the HEB300 columns

And the interaction diagram introduced in the HEB300 columns is shown in figure 4.5, where the values in the tables are multiples of the cross-sectional flexural resistance and axial resistance. The interaction curve shown presents the shape of a trapezium.

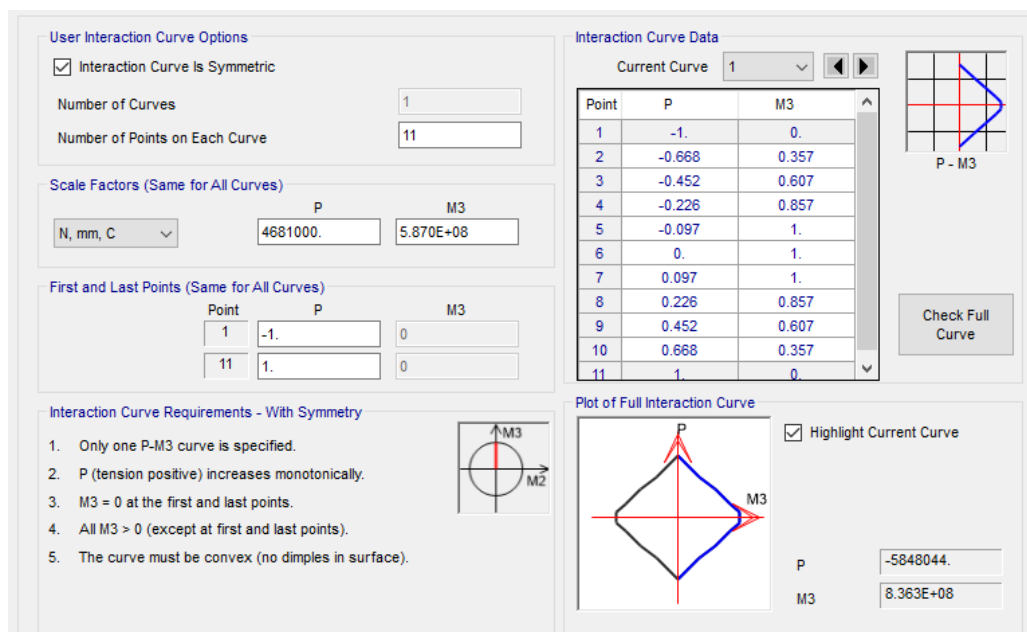


Figure 4.5: N-M interaction introduced in SAP2000 for the HEB300 columns

After the predesign of the structure and the definition of the rotational properties of the plastic hinges, the numerical analysis can be performed.

4.2.1.3 Numerical analysis

The analysis consists of a static nonlinear pushover analysis with displacement control at one node at the roof level. The structure was provided with a “leaning column” to consider second order effects, carrying all the mass of the gravity-resisting half of the building (the building only has two seismically resistant frames in each direction). After applying the vertical loads (self-weight, dead loads and live load) the lateral displacement increases and the formation of plastic hinges can be observed. For both structural typologies (MRF or D-EBF) the pushover is performed first on the structure without RBS and the maximum roof displacement d_n is obtained, when structural failure is achieved. Then, the same displacement d_n is imposed in the structure with RBS, and the plastic hinge pattern can be observed for the same imposed displacement in the two cases.

4.2.2 Moment Resisting Frames

The profile sections of the beams used in the frame are based on a gravity design. The columns are ranging between HEB300 and HEB260 after an equivalent lateral load predesign. Beam-to-column joints are modelled as capable of transmitting bending, shear and normal forces in all cases, full strength and fully rigid.

The design of the building has been undertaken assuming that all the members of the building carry gravitational loads, and all beam sections are HEA240. However, only the two façades parallel to the seismic action are actively resisting the earthquake induced forces. The frames of study correspond to those seismic resisting system façades.

For this case of study, a set of common values for the earthquake and soil have been chosen: the seismic action is characterised by a peak ground acceleration of 0.35g, a seismic response factor equal to 2.5, a behaviour factor q equal to 6 for MRF (with and without RBS), soil type B, 5% damping and spectrum type 1. The dynamic behaviour of the structure is assumed to be predominantly governed by the first mode of vibration. Under this assumption, the earthquake horizontal forces are introduced while monitoring of an imposed displacement at the roof level, according to EN1998-1, annex B.

The fundamental period of the structure has been approximated by $T_1 = C_t H^{3/4}$ according to [18] and [35] to reproduce the behaviour of the structures when designed with the simple and conservative approach in EN1998-1 without estimating the fundamental period by means of finite element analyses. For the case of the frame of study as a MRF the fundamental period is $T_1=0.83s$. This fundamental period has been used to obtain the equivalent lateral loads acting on the frame for the predesign of the columns to seism.

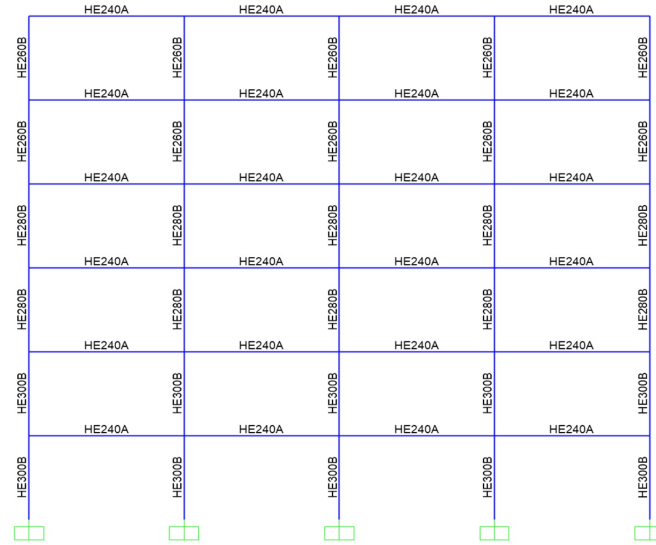


Figure 4.6: Six-storey four-span planar steel Moment Resisting Frame studied. Sections used for beams and columns

The columns have been provided with substantial overstrength with respect to the connected beams, in accordance with the strong column-weak beam principle, following the equation:

$$M_{pl,Rd}(N_{Ed}, V_{Ed}) > M_{Ed} = M_{Ed,G} + 1.1 \cdot \gamma_{ov} \cdot \Omega \cdot M_{Ed,E} \quad (4.1)$$

where $M_{pl,Rd}$ is the design bending resistance of the column taking into account the possible interaction with shear and axial forces, $M_{Ed,G}$ is the bending moment in the column due to non-seismic actions included in the seismic combination, $M_{Ed,E}$ is the bending moment in the column due to the design seismic action, γ_{ov} is the overstrength factor, 1.1 stands for the strain-hardening factor, and Ω is the "magnification coefficient", which ensures the strong column-weak beam behaviour, and is calculated as:

$$\Omega = \min \left(\frac{M_{pl,Rd,i}}{M_{Ed,i}} \right) \quad (4.2)$$

where $M_{pl,Rd,i}$ is the design plastic resistance of beam i and $M_{Ed,i}$ its design bending moment. The magnification coefficient Ω must be calculated for all the beams containing dissipative zones, and the minimum among all the values obtained should be used. The dissipative members should be designed in such a way so that the largest value of Ω obtained in the structure is no larger than 1.25 times the smallest obtained value ($\Omega_{max} \leq \Omega_{min}$).

4.2.2.1 Results for MRF with intact section

After imposing a lateral displacement at the roof level, the structure was considered to have failed at a total displacement $d_n=952$ mm, and the following scheme of plastic hinges is developed:

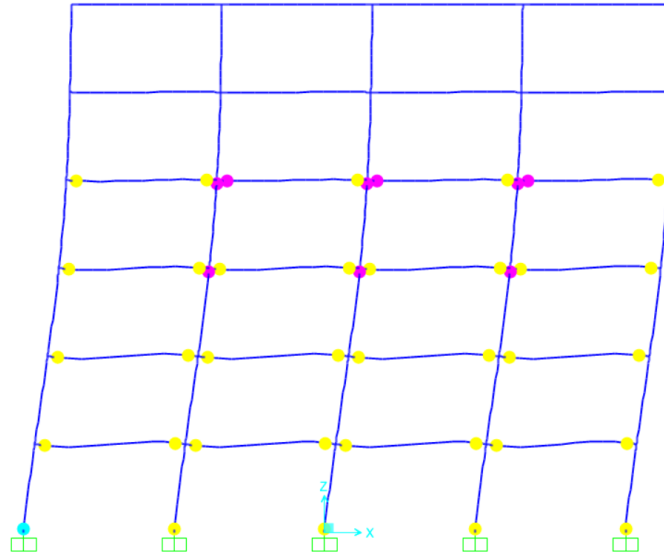


Figure 4.7: Results for the pushover analysis with MRF

As it can be observed, the structure develops plastic hinges in the beams and the column bases as well as a few columns at the third and fourth levels. A total of 43 plastic hinges are formed. The plastic hinges start forming at the second floor level, and extend progressively to the first, third and fourth level. The maximum plastic rotation achieved in the beams is 66.4 mrad, smaller than the limit $8\theta_y=115$ mrad for the studied beam cross-sections in compliance with EN1998-3. θ is calculated as:

$$\theta = \frac{M_{pl,b}L_b}{6EI_b} \quad (4.3)$$

where $M_{pl,b}$ is the plastic bending resistance of the beam, L_b is the beam span, and I_b is the inertia of the beam section.

4.2.2.2 Results for MRF with RBS

For the sake of comparison, the same total displacement $d_n=952$ mm was imposed at the roof level which caused structural failure for the MRF without RBS. After

the analysis the following scheme of plastic hinges was developed:

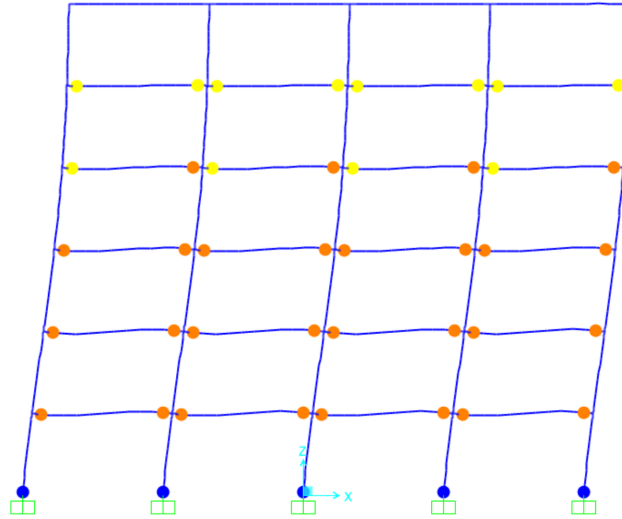


Figure 4.8: Results for the pushover analysis with MRF and RBS

The structure develops plastic hinges in the beams and the column bases only. The formation of plastic hinges in the beams extends over a higher amount of members with higher levels of rotation demand. The formation of the plastic hinges in the columns at the fourth level in this case is avoided, contrary to the case of the MRF without RBS, where a failure mechanism develops in the fourth level. The maximum rotation achieved is 63.4mrad, also smaller than the limit $8\theta_y$. A total of 45 plastic hinges are formed in this case.

4.2.3 Dual Eccentrically-braced Frames

For the case of the D-EBF the same procedure was followed in order to design the structure. The fundamental period of the structure in this case was estimated as $T_1=0.74s$. The links were HEA240 profiles (as well as the beams) and were designed with a length e of exactly 1m, thus behaving as short links and working mainly in shear. The length limit for a link being classified as "short" e_s is given in equation 4.4:

$$e \leq e_s = 1.6 \frac{M_{pl,link}}{V_{pl,link}} \quad (4.4)$$

And the eccentric braces have been designed with sufficient overstrength over the seismic links, according to the following expression:

$$N_{b,Rd}(M_{Ed}, V_{Ed}) > N_{Ed} = N_{Ed,G} + 1.1 \cdot \gamma_{ov} \cdot \Omega \cdot N_{Ed,E} \quad (4.5)$$

where $N_{b,Rd}(M_{Ed}, V_{Ed})$ is the design flexural buckling resistance of the diagonal brace taking into account any possible interaction with the design bending moment M_{Ed} or shear force V_{Ed} . Equation 4.5 is very similar to equation 4.1 since the philosophy of the design is the same in both cases. However, in this case, using equation 4.5 for the design of eccentric braces Ω needs to be calculated as:

$$\Omega = \min \left(\frac{V_{pl,link,i}}{V_{Ed,i}} \right) \quad (4.6)$$

since the failure mechanism in this case is dictated by the short links yielding in shear, not the development of plastic hinges in the beam ends.

After all this design process for the Dual Eccentrically-braced Frame, the sections for the braces will all be rectangular hollow sections 150x125x8. And figure 4.9 shows all the sections in the structure:

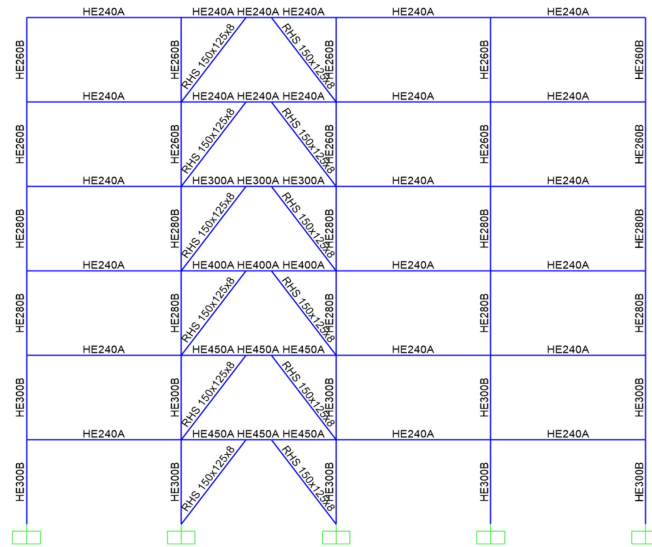


Figure 4.9: Six-storey four-span planar steel Dual Eccentrically-braced Frame studied. Sections used for beams, links, braces and columns

4.2.3.1 Results for D-EBF with intact section

The software in this case stopped the analysis at $d_n=304$ mm due to one of the links achieving the maximum rotation 0.08 rad (maximum allowable rotation for

short links as indicated in EN1998-1 - clause 6.8.2 (10) [18]). After this roof displacement is achieved, the following scheme of plastic hinges is developed:

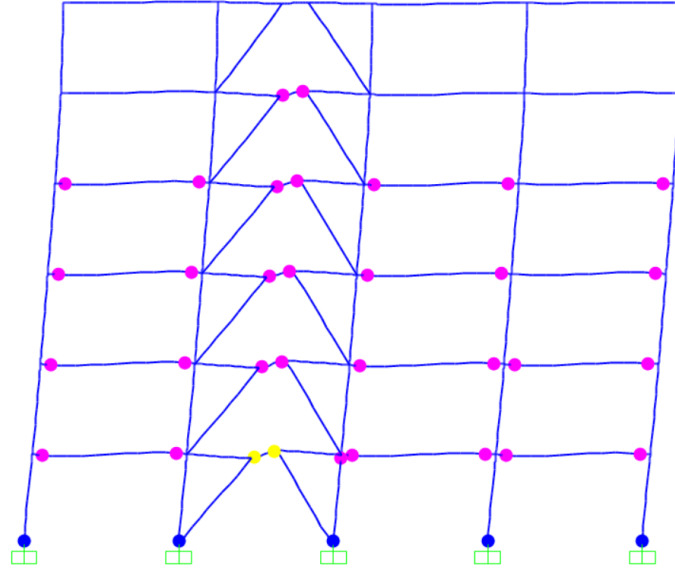


Figure 4.10: Results for the pushover analysis with DEBF. Source: A. Jiménez et al. [31]

The structure develops plastic hinges in the lower two links in the first place. As the structure is progressively loaded the progressive yielding of the seismic links occurs up to the fifth level. After the links have yielded and are in their plastic range a limited yielding of beams can be observed (exhibiting a similar behaviour to the MRF). The simultaneous yielding of 5 seismic links and all the beams in four different levels allows the structure to withstand the lateral displacement. A total of 38 plastic hinges are formed. The maximum rotation in the beams is 8.7 mrad, while the seismic link in the first floor achieves the maximum rotation allowed for short links 80 mrad.

4.2.3.2 Results for D-EBF with RBS

And in this case, the displacement causing structural failure in the structure with intact section is imposed ($d_n=304\text{mm}$, and the following plastic hinges formed:

As it can be observed, the structure develops a similar mechanism as the DEBF with no RBS, but the beams yielding is more generalised. Also, the maximum plastic rotation achieved is 12.1mrad, larger than in the previous case illustrated in Figure 11. A total of 45 plastic hinges are formed.

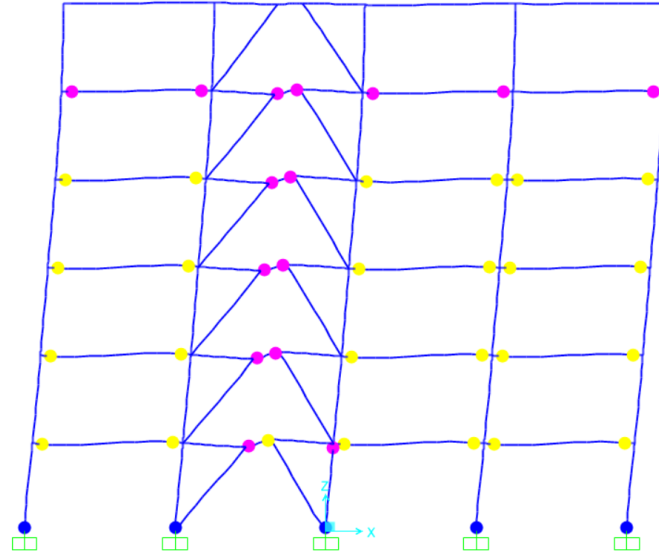


Figure 4.11: Results for the pushover analysis with DEBF and RBS. Source: A. Jiménez et al. [31]

4.2.4 Analysis of the results

From all the data gathered from the various analyses it is possible to compare the pushover curves for the MRF (Figure 4.12) and the DEBF (Figure 4.13) with and without RBS.

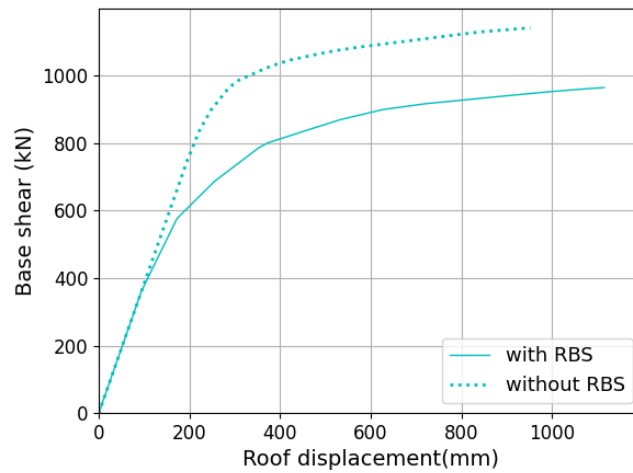


Figure 4.12: Base shear during the pushover analysis for the MRF. Source: A. Jiménez et al. [31]

It is clear that the curves for the MRF and MRF + RBS are identical up to about a displacement of 120 mm. From that point on the curves split into two. The difference in base shear for the displacement of 950 mm is about 19%.

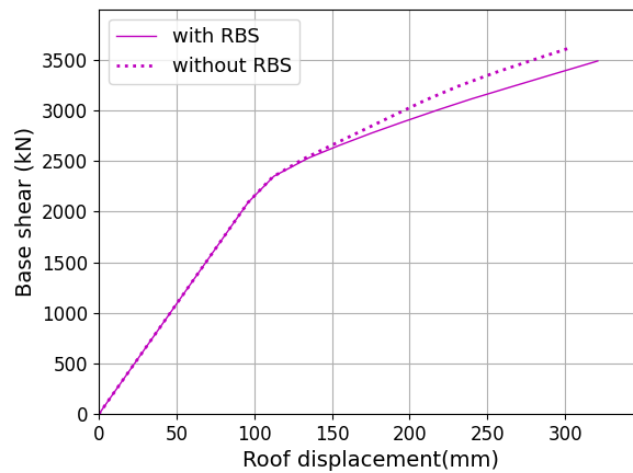


Figure 4.13: Base shear during the pushover analysis for the DEBF. Source: A. Jiménez et al. [31]

In the case of the DEBF, up to a displacement of 150mm both curves are very similar, when most of the dissipation occurs in the seismic links (where the first

plastic hinges form in all cases). However, for higher magnitudes of roof displacement the RBS does improve a bit the dissipative behaviour of the structure and more generalized beam plastic hinges develop. The difference in base shear for the displacement $d_n = 304\text{mm}$ is about 2%.

Although the studied structures are two and have concrete geometries and cross-sections, the benefits of the dog-bone are applicable to other structures of the same frame typologies, especially to MRF, which benefit the most from the reduced section. The results found herein can be reproduced for larger frames with different cross-sections, steel grades and beam spans and interstorey heights.

4.3 Second study, nonlinear time-history analysis

In this study, a numerical model is developed using the software Abaqus to reproduce the behaviour of a two-storey single-span moment resisting frame (MRF) when subjected to a ground acceleration by means of a nonlinear time-history analysis. A series of seismic records have been scaled up by means of the software SeismoMatch [38] in order to match a specific level of seismic demand. The structure of study is analysed with and without dog-bones in order to identify the differences in the behaviour of the structures when subjected to a seismic action. Base shear, interstorey drifts and dissipated plastic work are evaluated.

4.3.1 Definition of the seismic action

In order to impose the scaled seismic records to the structure matching the same level of seismic severity an elastic response spectrum needs to be defined to scale all the natural records to. The software SeismoMatch is used to that effect. A total of three recorded accelerograms provided by the software were used. These accelerograms correspond with the earthquakes of Kobe (Japan, 1994), Imperial Valley (United States and Mexico, 1940) and Friuli (Italy, 1976). This choice of accelerograms aims to consider earthquakes with different characteristics in order to have a greater generality of seismic inputs.

4.3.1.1 Elastic response spectrum and matching of the records

In order to consider a fairly severe spectrum, the seismic action considered in this study is represented by a peak ground acceleration $\text{PGA}=0.55g$, 5% damping, spectrum type 1, soil type C and importance class II. The corresponding elastic spectrum is shown in figure 4.14 according to EN1998-1, clause 3.2.2.

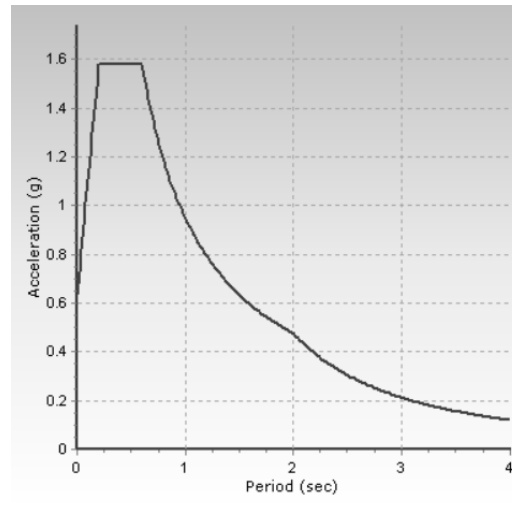


Figure 4.14: Elastic response spectrum used for the scaling of the seismic records

The recordings provided in SeismoMatch did not match the desired seismic severity (see figure 4.15a). After the proper scaling of the records, very good agreement has been achieved between the target spectrum in EN1998-1 and the spectrum of each of the earthquakes considered in this study (figure 4.15b). The matched recordings accurately represent the seismic demand of study and have been used in the analyses performed herein.

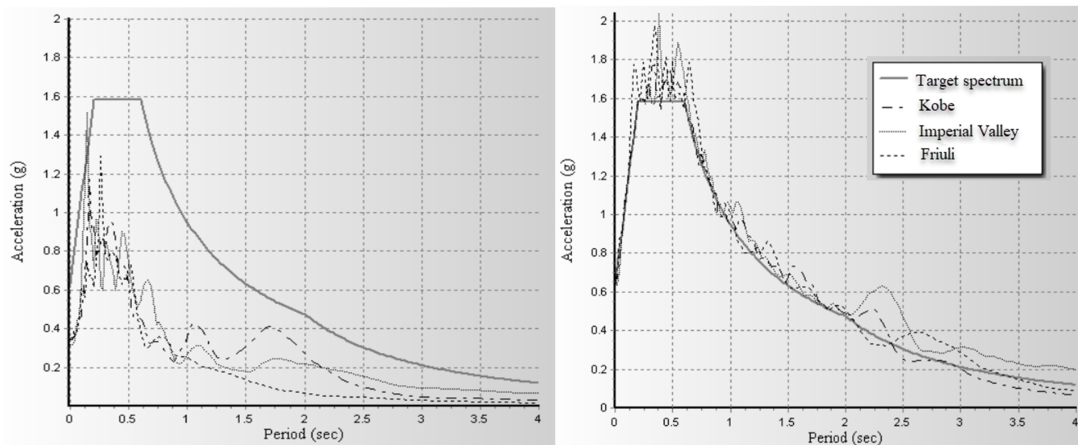


Figure 4.15: Target response spectrum and spectra derived from the seismic recordings (left) and derived from the matched recordings (right)

Figure 4.16 shows the original accelerograms for each seismic record (left, dotted lines) as well as the matched accelerograms introduced in the numerical model (right, continuous lines).

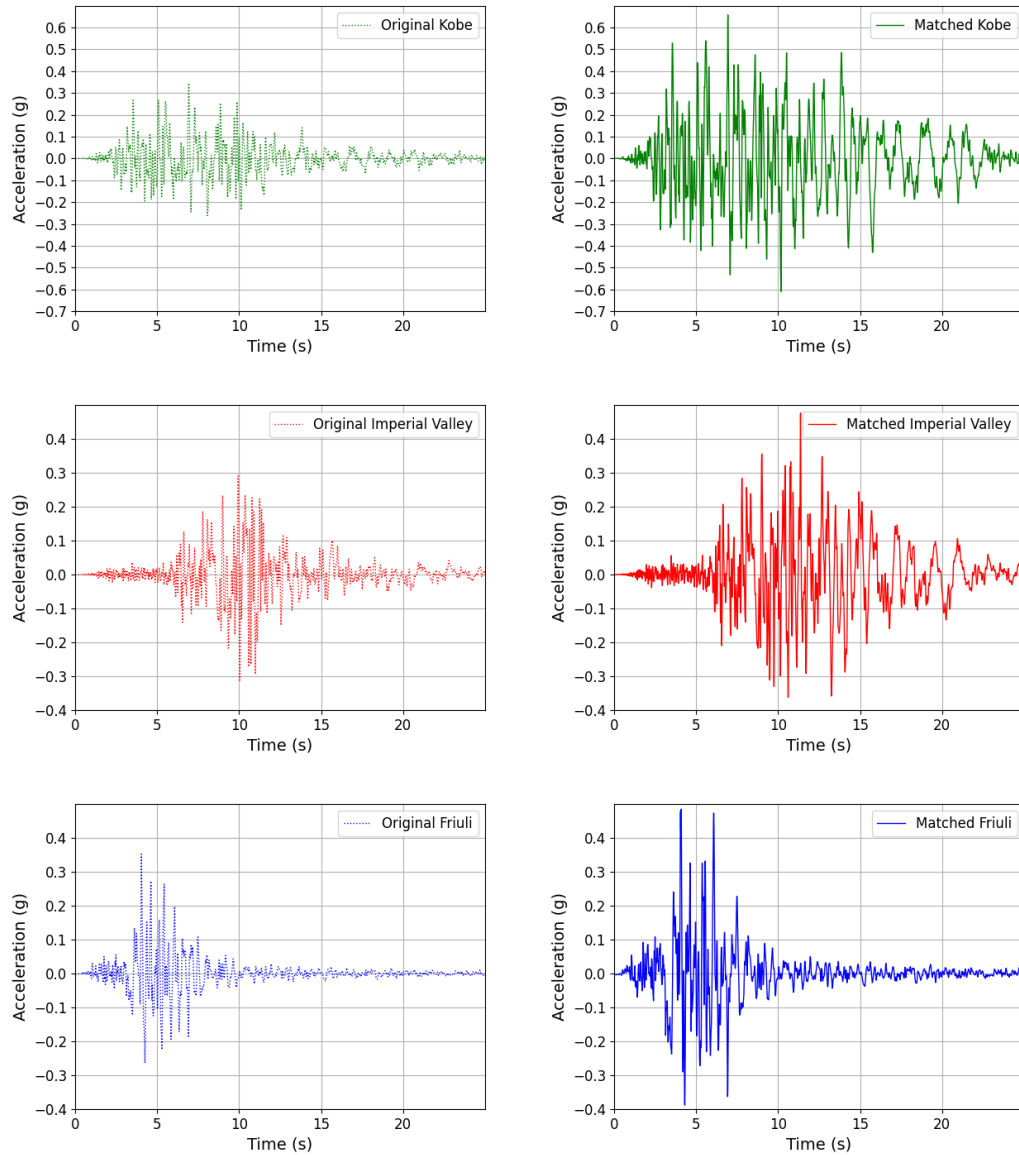


Figure 4.16: Original seismic records (dotted lines, left) and matched seismic records (continuous lines, right). Kobe (green), Imperial Valley (red) and Friuli (blue)

4.3.2 Numerical model

4.3.2.1 Description of the frame

The structure of study is a moment resisting frame with a single span and two

storeys. It is fixed at the column bases and is working only in-plane. The storey height is 5m and the beam span is 11m (measured between the centrelines of the columns). It has been designed under dead and live loads and checked against ultimate limit state as well as serviceability requirements according to EN1993-1-1 [16]. The sections used are IPE450 for the beams and HEB340 for the columns. All members are made of steel with S275 steel grade. Figure 4.17 shows the geometry of the structure considered in this study.

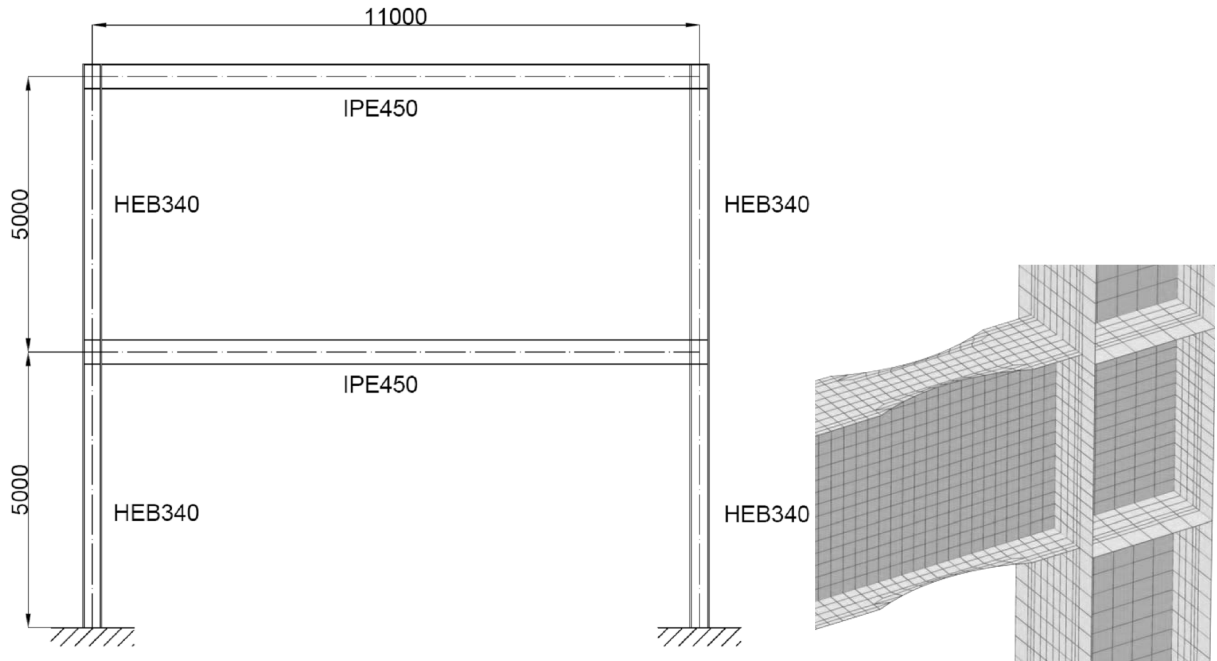


Figure 4.17: Structure of study with dimensions in mm (left) and view of the beam-to-column connection (right)

4.3.2.2 Geometry of the reduced beam section

The radius cut to be performed on the beams has been designed according to the prescriptions given in EN1998-3, annex B clause B.5.3.4 (3) [19] (see figure 4.18).

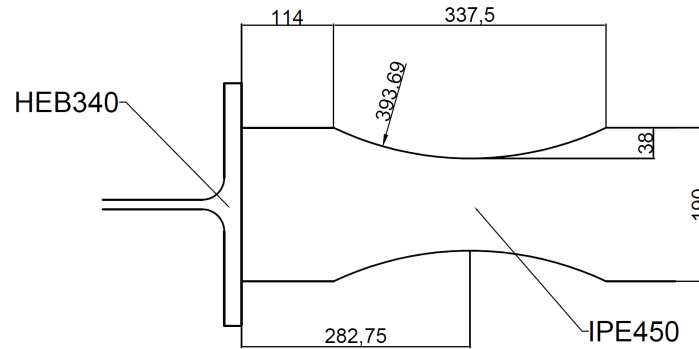


Figure 4.18: Scheme of the geometry of the Reduced Beam Section of study. Dimensions in mm

4.3.2.3 Characterisation of the material

The material used in the numerical model is a Chaboche nonlinear isotropic-kinematic hardening model with three backstresses [8] for carbon steel grade S275. The parameters introduced in Abaqus have been obtained from cyclic test data in the literature [33]. The values used are reported in table 4.2.

Table 4.2: Parameters for the definition of the properties of the material. Source: Krolo et al. [33]

Material	E (MPa)	ν	$\sigma _0$ (MPa)	C_1 (MPa)	γ_1	C_2 (MPa)	γ_2	C_3 (MPa)	γ_3	Q_∞ (MPa)	b
S275	207000	0.3	285	13921	765	4240	52	1573	14	25.6	4.4

4.3.2.4 Numerical model and analysis

The numerical model has been developed using only S4R shell elements for the whole structure. All shells were located at the middle plane of the plates. The top flanges of the beams have their movement restrained in the out-of-plane direction and cannot rotate due to torsion effects, simulating fixity due to the presence of a floor slab. Adequate stiffening of the panel zone and continuity plates were modelled. The welds were not taken into account in the model but the beams and columns were connected by sharing mesh nodes. More details on the numerical model can be found in [32].

The analysis conducted in Abaqus is a dynamic analysis with implicit integration. Masses due to self-weight and the loads acting in seismic combination have been introduced in the model. Vertical loads in seismic combination and an acceleration boundary condition was applied to reproduce the ground movement caused by the matched seismic records.

4.3.3 Results

After performing the six nonlinear time-history analyses the base shear, the interstorey drifts and the dissipated plastic work have been evaluated for each of the three matched seismic records. In the subsequent sections the obtained results are compared.

4.3.3.1 Base shear

The following graphs have been obtained after the analyses evaluating the base shear of the structure at every instant during the simulated seismic event. As it can be observed in figure 4.19, the differences in base shear are not very apparent between the cases with and without RBS. Indeed, it has been checked that the fundamental period of the structure does not change in a noteworthy manner due to the weakening of the beams and therefore, the forces acting on the structure remain the same. Both graphs tend to follow a very similar pattern, indicating similar responses from both structures (with and without RBS). This is especially so during the first seconds of the simulation, when little damage has occurred and there is very small influence on the stiffness by the RBS. After some damage is developed, differences start to be more evident.

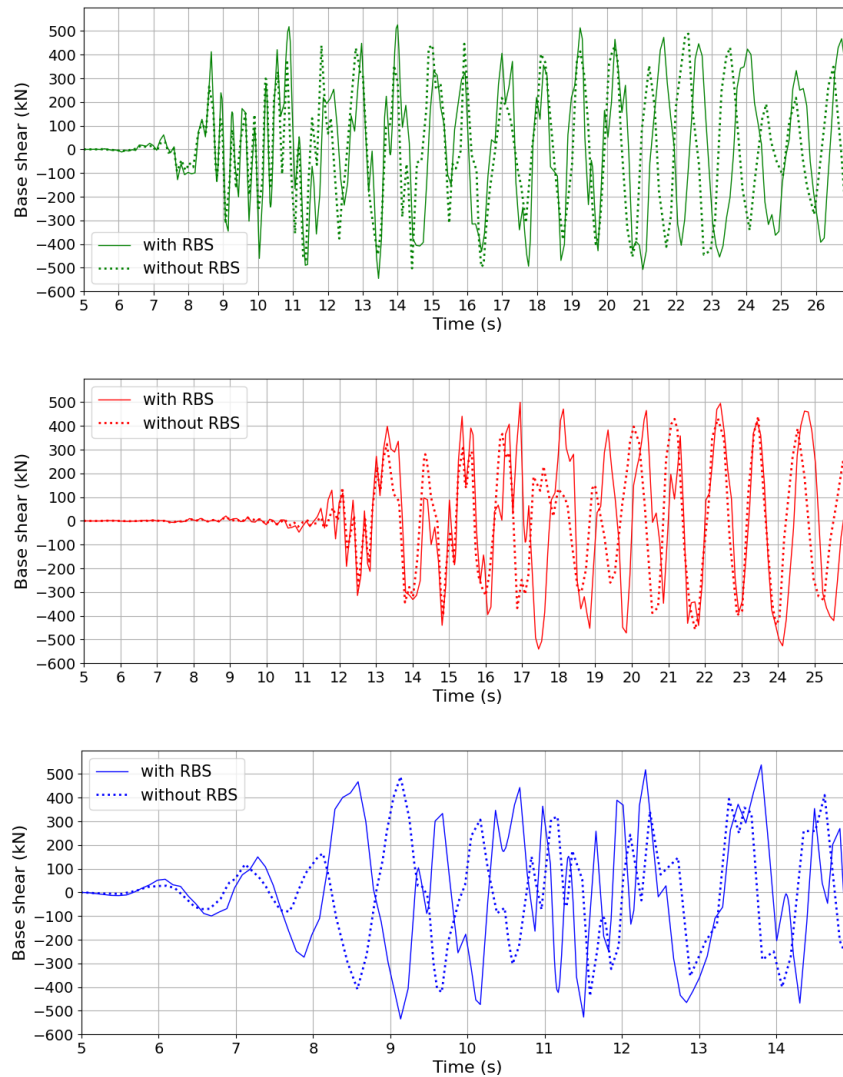


Figure 4.19: Evolution of the base shear of the structure during the analysis. Kobe matched earthquake (green), Imperial Valley matched earthquake (red), Friuli matched earthquake (blue)

4.3.3.2 Interstorey drift

The interstorey drift was measured for both storeys throughout the whole duration of the seismic event simulation. The following figures illustrate the results obtained for the first storey.

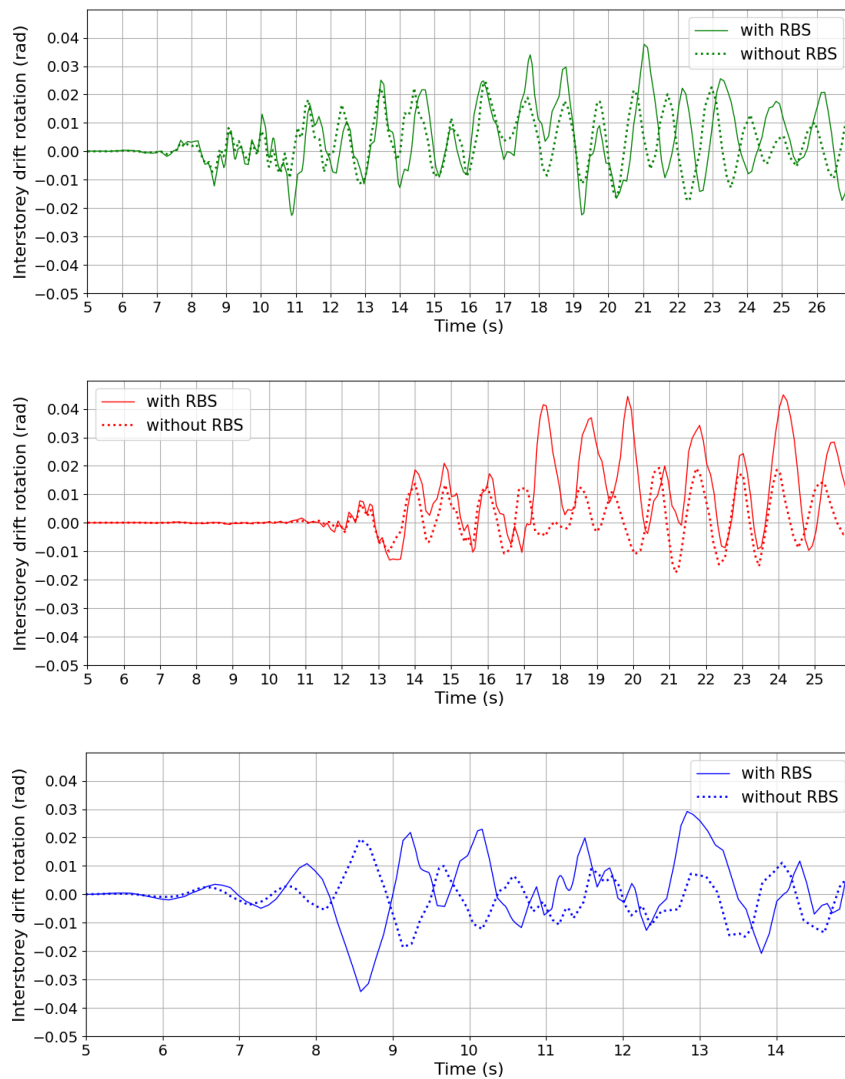


Figure 4.20: Evolution of the interstorey drift for the first storey. Kobe matched earthquake (green), Imperial Valley matched earthquake (red), Friuli matched earthquake (blue)

And figure 4.21 shows the interstorey drifts obtained for the second storey.

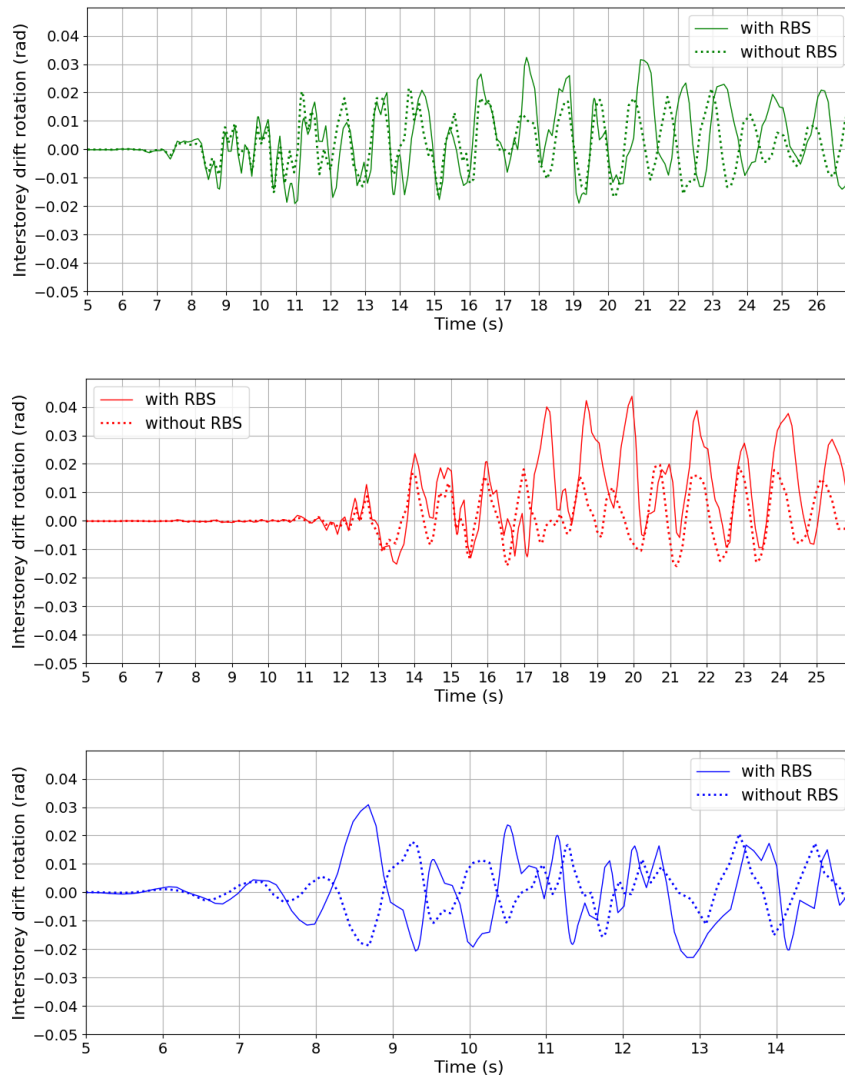


Figure 4.21: Evolution of the interstorey drift for the second storey. Kobe matched earthquake (green), Imperial Valley matched earthquake (red), Friuli matched earthquake (blue)

As it can be observed in figure 4.20 and figure 4.21, the maximum displacements achieved by the structure are always larger in the case of the frame that is provided with RBS. This seems to indicate that, although base shear seems to be the same (see figure 4.19), the structure is more flexible and can reach larger target displacements when plastic fuses are adopted.

This increase in lateral flexibility needs to be checked for damage limitation re-

quirements with a lower intensity seismic action (EN1998-1, clause 4.4.3.2 [18]), which causes lower plastic strains in the frame members. As a result, differences in interstorey drifts in damage limitation combinations between frames with and without RBS will be smaller than those in ultimate limit state combinations.

4.3.3.3 Dissipated plastic work

The total dissipated plastic work in the structure was also evaluated during the time-history analyses. For a single Gauss point, the dissipated plastic work w_{pl} is defined as shown in equation 2.10 (Lemaitre and Chaboche, 2009 [37]).

$$w^{pl} = \int_0^t \sigma_{ij}(\tau) \dot{\varepsilon}_{ij}^{pl}(\tau) d\tau \quad (4.7)$$

The total dissipated plastic work for each matched accelerogram is displayed in figure 4.22.

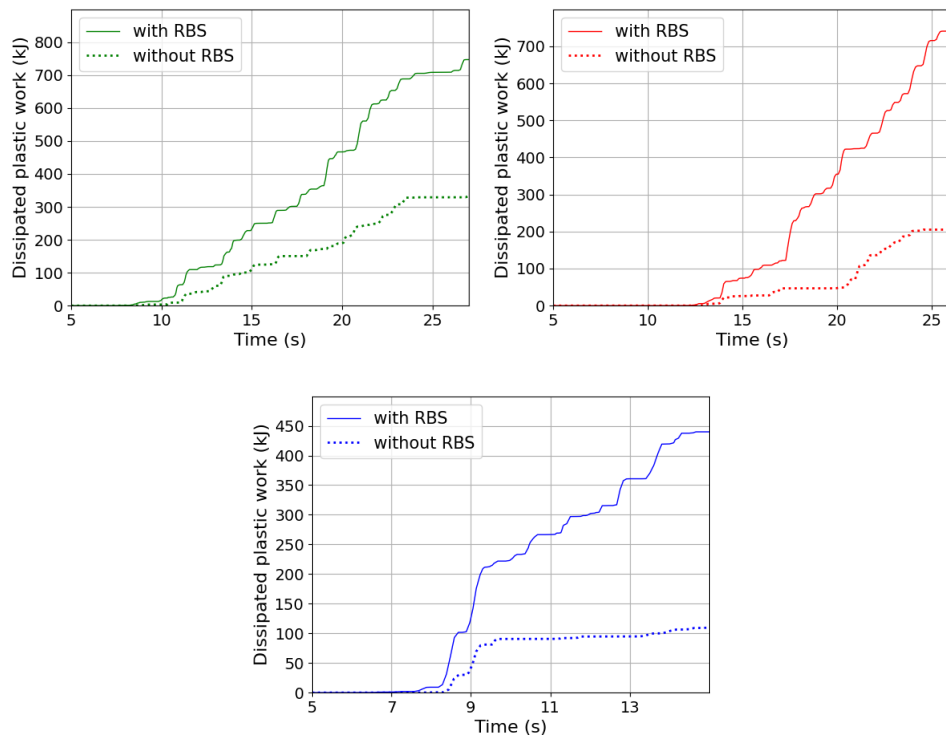


Figure 4.22: Evolution of the total dissipated plastic work for the whole structure. Kobe matched earthquake (green), Imperial Valley matched earthquake (red), Friuli matched earthquake (blue)

In the three cases analysed, the total dissipated plastic work w^{pl} is at least twice as much when the structure is provided with dog-bones. Since the structure is exactly the same in both cases with the single difference of the presence of RBS, this great difference in dissipated energy is clearly due to the higher dissipation in the dog-bones when experiencing plastic rotations.

This fact can be observed in figure 4.22, where equivalent plastic strains are compared for the Imperial Valley matched earthquake. For the structure with RBS the strains correspond with $t=21.63s$ and for the structure without RBS $t=21.73s$. The times are slightly different to ensure a similar level of base shear for the structure. The maximum equivalent plastic strains for the RBS (0.209) are almost three times those of the intact section (0.077) (see figure 4.23).

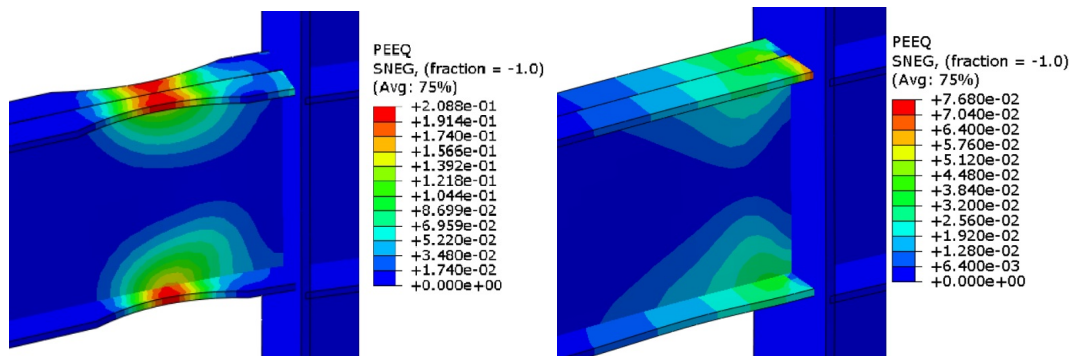


Figure 4.23: Equivalent plastic strain at the first storey right beam end. Imperial Valley Matched earthquake. Comparison between the Reduced Beam Section (left) and intact section (right)

It is clear from the results obtained in this study that the RBS provides a stable energy dissipation zone in the beam, promoting the development of plastic strains far away from the beam-to-column connection and avoiding any brittle fracture in the welds. The dissipation capacity of the structure by plastic dissipated work is greatly increased, thus requiring more energy input into the structure to cause collapse. Also, the structure is able to reach greater target displacements when provided with RBS, thus improving its ductility. Both of these characteristics are desirable when designing a highly dissipative structure in a seismic area.

5 Summary, conclusions and design recommendations

5.1 Summary

The current state of EN1998-1 [18] does not contemplate the possibility of a new seismic structural design provided with Reduced Beam Sections (RBS). Only EN1998-3 [19] contemplates the possibility to use RBS for the retrofit or seismic enhancement of existing buildings. Even in EN1998-3, the rules provided are few and entirely based on the American standard AISC 358 [2] and the FEMA 350 recommendations [22], which are not conceived with European cross-sections and steel grades in mind. This study aims to cast some more light on this topic which has been extensively studied before, but the current state of the art is lacking a systematic and exhaustive study on RBS in a European environment.

In this PhD thesis, a parametric study on the behaviour of Reduced Beam Sections is performed. The topic is addressed by means of a finite element model using the software Abaqus [56]. The numerical model developed is capable of reproducing with good accuracy the behaviour of beam-to-column assemblies provided with RBS (dog-bones). The model was validated by means of a comparison of the moment-rotation diagrams obtained in a laboratory test and the simulations performed with the model developed. It was found that the maximum strength achieved and the degradation after many cycles with load inversion showed very small differences between the models and the laboratory tests.

A total of 158 simulations have been performed. The parametric study involves three different trimmed flange widths $g = 0.2b_f$, $g = 0.25b_f$ and $g = 0.3b_f$; several column web panel strength ratios covering weak panels and very strong panels with r values up to 1.6; two different steel grades commonly used in Europe in seismic designs such as S235 and S355 grades, and a wide variety of hot-rolled European beam profiles (coupled with adequately strong columns) from the HEA and IPE families, ranging from depths of 450mm up to 1000mm. Also, a plated built-up girder and an American Jumbo section are studied with depths 1200mm and 1100mm, respectively.

Also, two smaller studies are included in the thesis to assess global structural behaviour when adopting RBS at the beam ends: in [31], the influence of the RBS is analysed by means of pushover analyses. A MRF and a D-EBF are provided with dog-bones, with moment-rotation curves previously obtained in Abaqus. The responses are compared to analogous control structures not provided with RBS.

In [32], a two-storey single-span MRF is subjected to three different accelerograms which have been modified in order to have them all match a certain seismic demand. By means of nonlinear time-history analyses the behaviour of the structure provided with dog-bones is compared to a control structure with intact beams.

5.2 Conclusions

The main conclusions to be drawn from the present study are the following:

- The results show that all the specimens achieve very substantial overstrength ratios M_{max}/M_{Rd} and most of them, with the exception of the built-up girder, retain a good amount of flexural strength at 40mrad, with good M_{40}/M_{Rd} ratios. However, excessive strain-hardening requires stronger columns to keep the resistance hierarchy, leading to more expensive solutions. The levels of strain-hardening found in the simulations is very high, especially for the S235 steel, where high overstrength due to material randomness makes this issue even worse.
- For the S355 steel grade, most of the assemblies presented M_{max}/M_{Rd} ratios of 1.0-1.5, with a few points at almost 1.6. For the S235 steel grade, most specimens exhibited overstrength ratios of about 1.4-2.0, with a few cases approaching 2.1. The current state of EN1998-1 [18] and EN1998-3 [19] do not account for such levels of overstrength, and the design of non-dissipative components (i.e. connections, columns, foundation...) with the suggested overstrength factors in Eurocode 8 could be unconservative, potentially leading to damage in such areas. Those values may need some revision according to the steel grade and cross-section, and even flange trimmed width g when applied to RBS solutions.
- The impact on the reduction in flange width comes with advantages and disadvantages: on the one hand, it provides more flange stability as the beam flanges become more compact, and by reducing the moment of inertia of the RBS, the maximum bending moment that can be achieved is also reduced, thus lowering the stresses and strains in the welded area. On the other hand, weakening the beam makes the beam more prone to lateral-torsional buckling. Assemblies experiencing lateral-torsional buckling have been observed to provide less stable hysteresis loops, with higher strength degradation. The specimens with more severe lateral-torsional buckling experienced a substantial amount of flange kinking, presenting great stress concentrations in the crooks of the beam flanges. Those areas are prone to developing fracture and need to be avoided. This has been found to be especially the case in the assemblies with a large trimmed width of the flanges $g = 0.3b_f$.

- The panel strength ratio r has proved to be an effective way to compare beam and column web panel strength. By increasing r it is possible to reduce the plastic engagement of the column, avoiding repair costs associated to the columns. By shifting the plastic engagement from the column onto the beam it also ensures that the dissipation is accomplished thanks to the RBS and the dissipative function is not shared between the two.
- It has also been observed in some cases that some specimens achieved high levels of shear force. No loss of flexural strength has been observed due to high shear, possibly thanks to the cyclic hardening of the material. This matter has not been directly addressed in the study, so further research is needed in order to draw solid conclusions in that regard.

And the main conclusions to be drawn from studies [31] and [32] on the benefits of the RBS on the structural response under seismic events are:

- The moment-rotation curves of the beam-to-column joints with and without RBS are much closer than might be expected a priori for the cases studied in [31]. The reduction in ultimate bending resistance due to the radius cut is not remotely approximate to the loss of plastic modulus in the RBS. This fact might be due to the fact that the RBS has lower slenderness in its flanges, possibly improving rotation capacity and delaying instabilities allowing for the achievement of greater strains.
- The global response of MRF is noticeably affected by the moment-rotation behaviour of the beam-to-column joints since most plastic hinges are formed in that region, governing the collapse mechanism. On the contrary, DEBF is negligibly affected by the moment-rotation behaviour of beam-to-column joints, since the seismic links play a major role in the behaviour of the structure when subjected to a lateral load.
- In all the studied cases in [31], the presence of RBS allows for a more generalised plastic engagement among the structural members. Indeed, it has been observed that the structures with RBS develop fewer plastic hinges in the columns and more plastic hinges in the beams, and more floors have their beams working in their plastic range. This is especially beneficial in order to avoid soft storey mechanisms.
- The study performed in [31] by means of a pushover analysis shows a reduction in base shear when the structure is provided with RBS compared to a case with no weakening of the beam ends. However, in [32], by using a nonlinear time-history analysis no substantial differences were found in base

shear. In spite of this fact, in [32] the nonlinear time-history analyses showed that larger displacements are achieved for a similar level of base shear.

- It is very clear from figure 4.22 that plastic dissipated work w^{pl} is much larger when the structure is provided with RBS. The RBS allowed for a dissipation between double and 3.5 times the dissipation without RBS for the frame of study with the accelerograms used.

5.3 Design recommendations

From the information gathered in this study, these are the design recommendations derived in order to obtain a good performance from a RBS design:

- As it has been observed in the study, excessive overstrength is a concern in RBS design. Since S235 steel has proved to have a great capacity to harden and to practically double its strength in some cases, leading to much more costly designs, it is recommended to use S355 steel for its use in RBS, which presents much lower overstrength ratios. prEN1998-1-2:2020 provides the values $\gamma_{ov} = 1.25$ and $\gamma_{sh} \leq 1.20$ for S355 steel grade which, as derived from the statistical analysis performed in this PhD thesis, seem to be adequate for new designs and as a result the total overstrength is $\alpha = \gamma_{sh} \cdot \gamma_{ov} = 1.50$. However, for S235 steel grade, the value $\gamma_{sh} = 1.20$ may be too small in some cases and could lead to unconservative designs. Based on the data obtained herein it is possible that S235 steels present values higher than that. More research is required to provide a design recommendation.
- As stated in EN1998-3 [19] and AISC 358 [2], flange reductions greater than $g = 0.25b_f$ are advised against. Such large reduction implies a loss of lateral stability with higher degradation of strength and possibly flange kinking, elevating the risk of crack initiation in the flanges.
- In order to further improve RBS behaviour, lateral braces should be placed at the end of the RBS the furthest away from the column flange, as indicated in AISC Seismic Provisions [1] in section D1 - clause 2c. In the case of a composite floor slab, such brace is not required. The RBS area should not be connected to the floor with shear studs, as welds and bolts in the RBS area may serve as fracture initiation sites (protected zone). Such lateral bracing system may make the larger flange cutouts $g = 0.3b_f$ viable if it can improve its performance to an acceptable level.
- The column web panel zone should be designed as a strong panel, with ratios of at least $r = 1.3$, provided the abovementioned recommended values for

γ_{sh} and γ_{ov} are used. This will diminish plastic engagement of the column to almost none, thus avoiding any permanent damage to the columns and avoiding any repair costs associated with them.

6 Future research

In this PhD thesis, a study on RBS on hot-rolled European cross-sections has been undertaken. Also, a built-up girder and an American Jumbo section have been included in the parametric study. However, there are some limitations to this study.

The conclusions derived from the study only apply to the members studied, which are mostly compact members. Only one slender member has been considered, which exhibited poor stability and therefore should not be used in a dissipative structure. Despite this, members with compact flanges and slender webs should be investigated in order to derive solid conclusions on the slenderness of the plates on the degradation of the strength of RBS. It is possible that section slenderness might need to be taken into account for the design of RBS for new designs and/or for the retrofit of existing structures. Also, not very compact members may have some value for their use in DCM designs with dog-bones.

In this study it has been found that, with the specific S235 steel used herein, very high levels of strain-hardening are achieved, significantly over the values provided in EN1998-1 and in prEN1998-1-2. Further research should be undertaken in this area with several S235 steels to derive more solid conclusions and possibly suggest a different value for γ_{sh} .

It has been observed in some of the simulations that significant shear appear in the RBS due to the significant hardening of the steel. Although shear and axial forces rarely need to be taken into consideration for the check of beam plastic bending resistance, it should be noted that some special cases may require to check these possible interactions closely.

Stainless steels provide very good ductility to structures, provided the design is good. RBS in stainless steel structures may be a viable option in highly seismic areas in situations where the added benefit of great corrosion and improved fire resistance may be useful. This matter could be addressed by another line of investigation.

Recently, more different approaches are being studied in order to weaken the beam in a certain location in order to avoid plastic engagement in the beam-to-column connection and/or the column. Aside from the RBS, the Reduced Web Section (RWS) and the drilled flange connections (DFCs) have proven to be a viable alternative to RBS. These types of solutions have not been studied deeply and more research is required.

References

- [1] AISC341-16. *Seismic Provisions for Structural Steel Buildings*, American Institute of Steel Construction. 2016.
- [2] AISC358. *Prequalified Connections for Special and Intermediate Steel Moment Frames for Seismic Applications*, American Institute of Steel Construction. 2016.
- [3] I. Arrayago, K.J.R. Rasmussen, and E. Real. Statistical analysis of the material, geometrical and imperfection characteristics of structural stainless steels and members. *Journal of Constructional Steel Research*, 175, 2020.
- [4] ASCE41-13. *Seismic Evaluation and Upgrade of Existing Buildings*, American Society of Civil Engineers, Reston, Virginia. 2013.
- [5] A. Atashzaban, I. Hajirasouliha, R. A. Jazany, and M. Izadinia. Optimum drilled flange moment resisting connections for seismic regions. *Journal of Constructional Steel Research*, 112, 2015.
- [6] AWS-D1.1. *Structural Welding Code*, American Welding Society. 2015.
- [7] AWS-D1.8. *Structural Welding Code - Seismic Supplement*, American Welding Society. 2016.
- [8] J. L. Chaboche. Time-independent constitutive theories for cyclic plasticity. *International Journal of Plasticity*, 2, 1986.
- [9] S.J. Chen and C.T. Tu. Experimental study of jumbo size reduced beam section connections using high strength steel. *Steel of Structural Engineering*, 130(4):582–587, 2004.
- [10] Computers and Structures INC. *CSI Analysis Reference Manual*, 2016.
- [11] A. Crisan and D. Dubina. Bending-shear interaction in short coupling steel beams with reduced beam section. *Journal of Constructional Steel Research*, 122, 2016.
- [12] M. D’Aniello, R. Landolfo, V. Piluso, and G. Rizzano. Ultimate behaviour of steel beams under non-uniform bending. *Journal of Constructional Steel Research*, 78, 2012.
- [13] M. Davarpanah, H. Ronagh, P. Memarzadeh, and F. Behnamfar. Cyclic behaviour of welded elliptical-shaped RWS moment frame. *Journal of Constructional Steel Research*, 175, 2020.

- [14] A.E. Deri and D.S. Sophianopoulos. Parametric analysis and optimization of reduced beam section steel frame connections. *7th European Conference on Steel and Composite Structures - Naples, Italy*, September 10-12, 2014.
- [15] A. Deylami and A. Moslehi Tabar. Promotion of cyclic behavior of reduced beam section connections restraining beam web to local buckling. *Thin-walled Structures*, 73, 2013.
- [16] EN1993-1-1. *Design of steel structures - part 1-1: General rules and rules for buildings*, European Comitee for Standardisation, 2020.
- [17] EN1993-1-8. *Design of steel structures – part 1-8: Design of joints*, European Comitee for Standardisation. 2009.
- [18] EN1998-1. *Design of structures for earthquake resistance – part 1: General rules, seismic actions and rules for buildings*, European Comitee for Standardisation. 2009.
- [19] EN1998-3. *Design of structures for earthquake resistance – part 3: Assessment and retrofitting of buildings*, European Comitee for Standardisation. 2011.
- [20] M. D. Engelhardt, T. Winneberger, A.J. Zekany, and T.J Potyraj. Experimental investigation of dogbone moment connections. *Engineering Journal*, 35(4), 1998.
- [21] FEMA273. *NEHRP guidelines for the rehabilitation of buildings*, Federal Emergency Management Agency, Washington (DC). 1997.
- [22] FEMA350. *Recommended Seismic Design Criteria for New Steel Moment-Frame Buildings*, Federal Emergency Management Agency. 2000.
- [23] E.M. Güneyisi, M. D’Aniello, R. Landolfo, and K. Mermerdaş. A novel formulation of the flexural overstrength factor for steel beams. *Journal of Constructional Steel Research*, 90, 2013.
- [24] E.M. Güneyisi, M. D’Aniello, R. Landolfo, and K. Mermerdaş. Prediction of the flexural overstrength factor for steel beams using artificial neural network. *Steel and Composite Structures, An International Journal*, 17(3), 2014.
- [25] Z. Guo and S.S. Huang. Behaviour of restrained steel beam with reduced beam section exposed to fire. *Journal of Constructional Steel Research*, 122, 2016.

- [26] S.W. Han, K.H. Moon, S.H. Hwang, and B. Stojadinovic. Rotation capacities of reduced beam section with bolted web (RBS-B) connections. *Journal of Constructional Steel Research*, 70, 2012.
- [27] S.W. Han, K.H. Moon, and B. Stojadinovic. Design equations for moment strength of RBS-B connections. *Journal of Constructional Steel Research*, 65, 2009.
- [28] Y. Hos and M. Vormwald. Measurement and simulation of strain fields around crack tips under mixed-mode fatigue loading. *Frattura ed Integrità Strutturale*, 33, 2015.
- [29] The MathWorks INC. *MATLAB Documentation*, 2021.
- [30] J.P. Jaspart. Contributions to recent advances in the field of steel joints. column bases and further configurations for beam-to-column joints and column bases. University of Liège, Belgium. 1997.
- [31] A. Jiménez, E. Mirambell, and E. Real. Structural behaviour of dual eccentrically braced frames with welded dog-bone joints subjected to cyclic loading. *9th International Conference on Steel and Aluminium Structures (ICSAS19)*, Bradford, UK, 2019.
- [32] A. Jiménez, E. Real, and E. Mirambell. Study on the influence of reduced beam sections on the seismic behaviour of a moment resisting frame. *The International Colloquium on Stability and Ductility of Steel Structures*, Prague, Czech Rep., 2019.
- [33] P. Krolo, D. Grandić, and Ž. Smolčić. Experimental and numerical study of mild steel behaviour under cyclic loading with variable strain ranges. *Advances in materials science and engineering*, page Article ID 7863010, 2016.
- [34] S.A. Kulkarni and G. Vesmawala. Study of steel moment connection with and without reduced beam section. *Case Studies in Structural Engineering*, 1:26–31, 2014.
- [35] R. Landolfo, F. Mazzolani, D. Dubina, L.S. da Silva, and M. D’Aniello. *Design of Steel Structures for Buildings in Seismic Areas*, ECCS Eurocode Design Manuals, Ed. Wiley. 2017.
- [36] C.H. Lee, K.H. Chang, and V.N. Van Do. Finite element modelling of residual stress relaxation in steel butt welds under cyclic loading. *Engineering Structures*, 103:63–71, 2015.

- [37] J. Lemaitre and J. L. Chaboche. *Mechanics of solid materials*, New York: Cambridge University Press. 2009.
- [38] SeismoSoft Ltd. *SeismoMatch: User's manual*, 2012.
- [39] F.M. Mazzolani and V. Piluso. Member behavioural classes of steel beams and beamcolumns. *Proceedings of First State of the Art Workshop*, pages 517–529, 1992.
- [40] R. Montuori. The use of the "dog-bone" for the seismic improvement of steel MRFs. *WSEAS Transactions on Applied and Theoretical Mechanics*, 2016.
- [41] R. Montuori. Less is more: the reduction of beam section for the seismic behaviour improvement of existing steel moment-resisting frames. *6th International Conference on Theoretical and Applied Mechanics*, Salerno, Italy. 2015.
- [42] M.A. Morshedi, K.M. Dolatshahi, and S. Maleki. Double reduced beam section connection. *Steel of Constructional Steel Research*, 138:283–297, 2017.
- [43] American Institute of Steel Construction. *Advisory Statement on Mechanical Properties Near the Filled of Wide Flange Shapes and Interim Recommendations*, January 10, 1997.
- [44] M. Ohsaki, H. Tagawa, and P. Pan. Shape optimization of reduced beam section under cyclic loads. *Journal of Constructional Steel Research*, 65(7), 2009.
- [45] D.T. Pachoumis, E.G. Galoussis, E.G. Kalfas, and A.D. Christitsas. Reduced beam section moment connections subjected to cyclic loading: Experimental analysis and fem simulation. *Engineering Structures*, 31, 2009.
- [46] D.T. Pachoumis, E.G. Galoussis, E.G. Kalfas, and I.Z. Efthimou. Cyclic performance of steel moment-resisting connections with reduced beam sections - experimental analysis and finite element model simulation. *Engineering Structures*, 32, 2010.
- [47] A. Plumier. New idea for safe structure in seismic zones. *Proceedings of IABSE symposium on mixed structures including new materials*, pages 431–436, 1990.
- [48] Equaljoints Plus. *Volume with pre-normative design recommendations for seismically qualified steel joints*, European Convention for Constructional Steelwork. 2018.

- [49] FreeDam Plus. *Seismic Design of Steel Structures with FREE from DAMAge Joints*, European Convention for Constructional Steelwork. 2020.
- [50] prEN1998 1-2:2020. *Design of structures for earthquake resistance – part 1-2: Rules for new buildings (Draft version)*, European Comitee for Standardisation. April, 2020.
- [51] R. Rahnavard, A. Hassanipour, and N. Siahpolo. Analytical study on new types of reduced beam section moment connections affecting cyclic behavior. *Case Studies in Structural Engineering*, 3, 2015.
- [52] M.T. Roudsari, F. Abdollahi, H. Salimi, S. Azizi, and A.R. Khosravi. The effect of stiffener on behavior of reduced beam section connections in steel moment-resisting frames. *The International Journal of Steel Structures*, 15(4), 2015.
- [53] A. Saleh, S.R. Mirghaderi, and S.M. Zahrai. Cyclic testing of tubular web rbs connections in deep beams. *Journal of Constructional Steel Research*, 117, 2016.
- [54] C.E. Sofias, C.N. Kalfas, and D.T. Pachoumis. Experimental and fem analysis of reduced beam section moment endplate connections under cyclic loading. *Engineering Structures*, 59:320–329, 2014.
- [55] D.S. Sophianopoulos and A.E. Deri. Parameters affecting response and design of steel moment frame reduced beam section connections: an overview. *The International Journal of Steel Structures*, 11(2):133–144, 2011.
- [56] Dassault Systèmes. *Abaqus 2016 Online Documentation*, 2016.
- [57] M.G. Vetr, M. Miri, and A. Haddad. Seismic behavior of a new reduced beam section connection by drilled holes arrangement (RBS_DHA) on the beam flanges through experimental studies. *Proceedings of the 15th World Conference on Earthquake Engineering - Lisbon, Portugal*, September 24-28, 2012.
- [58] X. Yun and L. Gardner. Stress-strain curves for hot-rolled steels. *Journal of Constructional Steel Research*, 133:36–46, 2017.
- [59] X. Zhang, J.M Ricles, L.W. Lu, and J.W. Fisher. Analytical and experimental studies on seismic behavior of deep column-to-beam welded reduced beam section moment connections. *13th World Conference on Earthquake Engineering - Vancouver, Canada*, Paper No. 1599, August 1-6, 2004.